Chem Soc Rev

Density Functional Theory Studies of Transition Metal Carbides and Nitrides as Electrocatalysts

Journal:	*Chemical Society Reviews*
Manuscript ID	CS-REV-06-2021-000590.R1
Article Type:	Review Article
Date Submitted by the Author:	25-Aug-2021
Complete List of Authors:	Tian, Dong; Kunming University of Science and Technology, State Key Laboratory of Complex Nonferrous Metal Resources Clean Utilization; Columbia University, Department of Chemical Engineering Denny, Steven; Columbia University, Department of Chemical Engineering Li, Kongzhai; Kunming University of Science and Technology, Metallurgy and Energy Engineering Wang, Hua ; Kunming University of Science and Technology, State Key Laboratory of Complex Nonferrous Metal Resources Clean Utilization Kattel, Shyam; Florida A&M University, Physics Chen, Jingguang; Columbia University, Chemical Engineering

Chem Soc Rev

REVIEW ARTICLE

Density Functional Theory Studies of Transition Metal Carbides and Nitrides as Electrocatalysts

Received 00th January 20xx,
Accepted 00th January 20xx

DOI: 10.1039/x0xx00000x

Dong Tian,[abc] Steven R. Denny, [b] Kongzhai Li,*[a] Hua Wang,*[a] Shyam Kattel*[d] and Jingguang G. Chen*[bc]

Transition metal carbides and nitrides are interesting non-precious materials that have been shown to replace or reduce the loading of precious metals for catalyzing several important electrochemical reactions. The purpose of this review is to summarize density functional theory (DFT) studies, describe reaction pathways, identify activity and selectivity descriptors, and present a future outlook in designing carbide and nitride catalysts for the hydrogen evolution reaction (HER), oxygen evolution reaction (OER), oxygen reduction reaction (ORR), nitrogen reduction reaction (N_2RR), CO_2 reduction reaction (CO_2RR) and alcohol oxidation reactions. This topic is of high interest to scientific communities working in the field of electrocatalysis and this review should provide theoretical guidance for the rational design of improved carbide and nitride electrocatalysts.

1. Introduction

Transition metal carbide (TMC) and nitride (TMN) materials are synthesized by incorporating carbon and nitrogen atoms into the interstitial sites of transition metals, all 3d elements, as well as 4d and 5d elements of group IVB-VIB early transition metals.[1-3] These TMC and TMN materials have demonstrated unique physical and chemical properties, which combine the characteristic properties of covalent solids, ionic crystals, and transition metals.[4-6] For example, they often possess the extreme hardness and brittleness of covalent solids, the high melting temperature and simple crystal structures of ionic crystals, and electronic and magnetic properties similar to transition metals.[1,4] TMC and TMN materials often show characteristic properties similar to platinum-group metals (PGMs).[1,2,7-9] Currently PGM-based catalysts are the best performing catalysts for many electrochemical reactions.[10] However, the high cost and low earth-abundance of PGMs are potentially major obstacles for the large scale application of technologies that rely on the use of PGMs as catalysts. The utilization of TMC and TMN materials, either as catalysts or as catalyst supports, has the potential to replace or substantially reduce the loading of PGMs for several electrocatalytic reactions.

[a] State Key Laboratory of Complex Nonferrous Metal Resources Clean Utilization /Faculty of Metallurgical and Energy Engineering, Kunming University of Science and Technology, Kunming, Yunnan, 650093, China.
[b] Department of Chemical Engineering, Columbia University, New York, NY, 10027, USA.
[c] Chemistry Division, Brookhaven National Laboratory, Upton, NY, 11973, USA.
[d] Department of Physics, Florida A&M University, Tallahassee, FL, 32307, USA
*Corresponding author: kongzhai.li@aliyun.com (Kongzhai Li), wanghua65@163.com (Hua Wang), shyam.kattel@famu.edu (Shyam Kattel), jgchen@columbia.edu (Jingguang G. Chen).

The rational design of active and selective TMC and TMN catalysts relies on the fundamental understanding of the interactions between molecular species and the catalyst surface. However, the atomistic picture of such interactions cannot be achieved by relying on experimental techniques alone. Theoretical calculations that provide an accurate description of bond forming and breaking processes at the atomic level are suitable in this regard. Density functional theory (DFT) electronic structure calculations, based on the time-independent Schrodinger equation, have emerged as an important, reliable, and transferable method to investigate the molecular processes at the nanoscale. Thus, DFT calculations, which provide the ground state energy of a system, offer a unique opportunity to compute the energetics of a reaction on catalytic surfaces. DFT calculations have been applied extensively to understand the electrocatalytic applications of TMC and TMN catalysts. The DFT based atomistic understanding of catalyst structures and reaction mechanisms, as well as the identification of key reaction descriptors, play an important role for the accelerated discovery of catalysts based on TMC- and TMN materials.

In this review, we aim to summarize and provide an in-depth discussion of recent DFT studies of energy related electrochemical reactions performed on TMC- and TMN-based electrocatalysts. We will first introduce parameters and structural models that are typically used for DFT calculations of TMC and TMN surfaces. We will then summarize the general trends in the utilization of TMC- and TMN-based catalysts for a wide range of electrochemical reactions, including hydrogen evolution reaction (HER), oxygen evolution reaction (OER), oxygen reduction reaction (ORR), nitrogen reduction reaction (N_2RR), CO_2 reduction reaction (CO_2RR) and alcohol oxidation reactions. We will also identify opportunities and challenges for

Table 1 Summary of DFT calculated parameters for selected electrochemical reactions on TMCs and TMNs as either catalysts or catalyst supports.

Reactions	System	DFT/DFT+U	Functional (vdW=van der Waals correction)	Unit cell	k-points
		DFT			
HER	Unmodified and metal-modified NbC, TaC, TiC, VC(111) and WC, W_2C, Mo_2C(0001)[11]	DFT	GGA-PW91	3 × 3	3 × 3 × 1
		-	-	-	-
	Pt and Pd supported on W-/C-terminated WC(0001)[12]	DFT	GGA-PBE	$2 \times \sqrt{3}$	4 × 4 × 1
	β-Mo_2C(0001)[13]	DFT	GGA-PW91	3 × 3	4 × 4 × 1
	Fe_3C(001), B_4C(111), Mo_2C(011) and (101), TiC(310)[14]	DFT	GGA-RPBE	2 × 2	4 × 4 ×1
	M_1N_1 (M = Sc, Ti, Y, Hf, Ta and Mo, N is nitrogen) (100) facet[15]	DFT	GGA-RPBE	3 × 3	4 × 4 × 1
		-	-	-	-
	PdH/NbN(111) and PdH/VN(111)[16]	DFT	GGA-PW91	3 × 3	3 × 3 × 1
	Co_4N(111) and V-Co_4N(111)[17]	DFT	GGA-PBE	2 × 2	3 × 3 × 1
	$M_{n+1}C_nO_2$ and $M_{n+1}N_nO_2$ (M = Sc, Cr, Hf, Mo, Nb, Ta, Ti, V, W, Zr; n = 1, 2, 3)[18]	DFT	GGA-PBE	3 × 3	4 × 4 × 1
		-	-	-	-
	Heteroatom X (X = N, B, P, S) doping effect on the HER of M_2C MXene (M = Ti, Mo)[19]	DFT	GGA-PBE-vdW	3 × 3	5 × 5 × 1
		-	-	-	-
	Ni-Activated TMCs (M = V, Fe, Cr, and Mo)[9]	DFT	GGA-PBE	2 × 2	-
	Single atom catalysts of transition-metal (23 different TM) doped phosphorus carbide monolayer (α - PC)[20]	DFT	GGA-PBE-vdW	2 × 4	3 × 5 × 1
		-	-	-	-
OER	WC, Mo_2C, VC, NbC, TaC(110) and TiC, ZrC(0001)[3]	DFT	GGA-PW91	3 × 3	3 × 3 × 1
	V_4C_3, V_8C_7 and VC surfaces of (0001), (110) and (111)[21]	DFT	GGA-PBE	-	4 × 4 × 2
	Co-doped Fe_3C@Carbon nano-onions[22]	DFT	GGA-PBE	2 × 1	4 × 4 × 1
	M_1C_2 (M = Ti, V, Nb, Ta, and Mo, C is carbon)[5]	DFT	GGA-PBE-vdW	2 × 2	5 × 5 × 1
	IrO_2(110), IrO_2/Ni_4N(111) and IrO_2/Fe_4N(111)[23]	DFT	GGA- PW91	5 × 5	1 × 1 × 1
	$Ni_{1.5}Co_{1.5}N$ and PF/$Ni_{1.5}Co_{1.5}N$ nanorods arrays[24]	DFT	GGA-PBE-vdW	-	3 × 3 × 1
	NiFeP/MXene electrocatalyst[25]	DFT+U_{DFT}	GGA-PBE-vdW	4 × 4	3 × 3 × 1
ORR	Pt_{ML}/TiC(001)[26]	DFT	GGA-PBE	3 × 3	5 × 5 × 1
	Pd_{ML}/TiC(001)[4]	DFT	GGA-PBE	3 × 3	3 × 3 × 1
	Graphene(G) and N-doped graphene(NG) supported on Fe_3C(010) and Fe(110) [27]	DFT	BEEF-vdW	$\sqrt{3} \times \sqrt{3}$	-
		-	-	$\sqrt{2} \times \sqrt{2}$	-
	Monolayer Pt, Pd, Au supported on WC(0001)[28]	DFT	GGA-PW91	3 × 3	5 × 5 × 1
	TiN(111) and TiN(200)[29]	DFT	GGA-PBE	2 × 2	4 × 4 × 1
	Different facets of CoN[30]	DFT	GBRV-RPBE	2 × 2	8 × 8 × 1
	Pt/Pd-doped Nb_2CT_2 MXene (T = O, F and OH)[31]	DFT+U_{DFT}	GGA-PBE-vdW	3 × 3	5 × 5 × 1
N_2RR	Molybdenum carbide nanodots (Mo_2C/C)[32]	DFT	GGA-PBE	-	5 × 5 × 1
	Different facets of MoC and $MoC_{0.5}$[6]	DFT	GGA-PBE	2 × 2	4 × 4 × 1
	Surfaces of γ-MoN[33]	DFT	GGA-PBE	4 × 4	4 × 4 × 1
	Rocksalt and zinc blende of VN, ZrN, CrN and NbN[34]	DFT	GGA-RPBE	3 × 3	4 × 4 × 1
	Zincblende (110) surfaces of metal nitrides[35]	DFT	GGA-RPBE	3 × 3	4 × 4 × 1
	VNO (111)[36]	DFT	GGA-PW91	2 × 2	3 × 3 × 1
	VN(111) and $VN_{0.75}O_{0.25}$(111)[37]	DFT	GGA-PW91	4 × 4	4 × 4 × 1
	M_2XT_x MXenes (M = Ti, V, Zr, Nb, Mo, Ta, W; X = C, N)[38]	DFT	BEEF-vdW	2 × 2	4 × 4 × 1
	M_2C (M = Sc, Ti, V, Cr, Mn, Fe, Zr, Nb, Mo, Ta and Hf) MXenes[39]	DFT	GGA-PBE-vdW	4 × 4	3 × 3 × 1
		-	-	-	5 × 5 × 1
	Single TM embedded in MXene ($Mo_2TiC_2O_2$) defects[40]	DFT	GGA-PBE-vdW	3 × 3	3 × 3 × 1
	Series of single TM atom anchored Mo_2CO_2 or Ti_2CO_2[41]	DFT	GGA-PBE-vdW	2 × 2	5 × 5 × 1
CO_2RR	PdH/TaC(111) and PdH/NbC(111)[42]	DFT	GGA-PW91	3 × 3	3 × 3 × 1
	M/WC (M = Mn, Fe, Co, Ni, Cu, Zn, Ru, Rh, Pd, Ag, Ir, Pt, and Au)[43]	DFT	GGA-RPBE	2 × 2	2 × 2 × 1
		-	-	-	6 × 6 × 1
	Pt_{ML}/WC and WC[44]	DFT	GGA-RPBE	3 × 2	2 × 3 × 1
	Transition metal carbides (MXenes)[45]	DFT	GGA-PBE-vdW	-	5 × 5 × 1
	TiC- and TiN-supported single-atom[46]	DFT	GGA-RPBE-vdW	4 × 4	3 × 3 × 1
	Palladium-modified TMNs (Pd/TMN)[16]	DFT	GGA-PW91	3 × 3	3 × 3 × 1
	Ti_2CT_x and Mo_2CT_x MXenes[47]	DFT	GGA-PBE-vdW	3 × 3	3 × 3 × 1

	O-terminated M_2XO_2 type MXenes, where M = Sc, Ti, Zr, Hf,	DFT	GGA-PBE-vdW	3 × 3	2 × 2 × 1
	V, Nb, Ta, Cr, Mo, W; and X = C, N. [48]	-	-	-	-
	M_3C_2 (M = Sc, Ti, V, Cr, Mn, Y, Zr, Nb, Mo, MoTi, Hf, Ta, and	DFT	GGA-PBE-vdW	3 × 3	5 × 5 × 1
	W)[49]	-	-	-	-
	Mo_2C and Ti_3C_2 MXenes[50]	DFT+U_{DFT}	GGA-PBE	3 × 3	4 × 4 × 1
	Single transition metal (TM = Sc, Ti, V, Cr, Mn, Fe, Co, Ni,	DFT	GGA-PBE-vdW	3 × 3	3 × 3 × 1
	Cu, Zn) atom catalysts on Ti_2CN_2[51]	-	-	-	-
	Mo Carbides[52]	DFT	BEEF-vdW	3 × 3	4 × 4 × 1
	Pd/WC(0001) for MOR[53]	DFT	GGA-PW91	3 × 3	3 × 3 × 1
MOR,	Pt and α-WC surfaces for MOR[54]	DFT	GGA-PBE	3 × 3	3 × 3 × 1
EOR	Series of Pt-modified WC(0001) for MOR[55]	DFT	GGA-PBE	3 × 3	4 × 4 × 1
	Pt_{ML}/TaC(111) for EOR[56]	DFT	GGA-PW91	3 × 3	3 × 3 × 1
	Pt_{ML}/WC(0001) for EOR[57]	DFT	GGA-PW91	3 × 3	3 × 3 × 1

improving the electrocatalytic performance of these materials using DFT calculations.

2. DFT Methods

The low index thermodynamically stable surfaces (e.g. (111), (100), and (110) surfaces) are typically used to represent the nanoparticle catalyst surface to gain a mechanistic understanding of active sites, reaction mechanisms, and key activity and selectivity descriptors. The DFT optimized bulk structures are used to cleave the relevant surface to study surface reactions. Within this approach, the binding energy (BE) of an adsorbate on a catalyst surface can be calculated as[11,14,16,29,42,58-64]

$$BE = E_{(slab\text{-}adsorbate)} - E_{(slab)} - E_{(adsorbate)} \quad \textbf{(Equation 1)}$$

where $E_{(slab\text{-}adsorbate)}$, $E_{(slab)}$, and $E_{(adsorbate)}$ are the total energy of slab with adsorbate, the total energy of clean slab, and the energy of adsorbate in the gas phase, respectively. According to this definition, more negative adsorption energy indicates stronger adsorption.[29]

The DFT calculated total energy can be used to compute the Gibbs free energy (G) of a gas phase species as [14,61,65]

$$G = E + ZPE - TS \quad \textbf{(Equation 2)}$$

Here, E is the total energy of a species obtained from DFT calculations. ZPE and S are the zero-point energy and entropy of a species, respectively. First-principles DFT calculations can be used to determine the vibrational modes with reasonable accuracy. Then the entropy of a species can be calculated using the DFT calculated vibrational frequencies using the harmonic normal mode approximation as[39,66]

$$S_{vib} = k_B \sum_i^{\#\text{ of modes}} \left(\frac{x_i}{e^{x_i} - 1} - \ln\left(1 - e^{-x_i}\right)\right) \quad \textbf{(Equation 3)}$$

where x_i for each vibrational mode is defined in terms of the vibrational frequency, ν_i, as[39]

$$x_i = \frac{\hbar \nu_i}{k_B T} \quad \textbf{(Equation 4)}$$

And the ZPE value can also be calculated from ν_i as[39,66]

$$E_{ZPE} = 1/2 \sum_i^{\#\text{ of models}} \hbar \nu_i \quad \textbf{(Equation 5)}$$

Here, k_B and $\hbar$ are the Boltzmann constant and the Planck's constant, respectively, and T is temperature. Thus, the ZPE and entropy contribution can be calculated within the DFT approach.

Electrochemical reactions occur in complex environments that are influenced by the electrolyte, solution pH, applied potential (U), and other electrochemical conditions. Thus, the DFT modeling of electrochemical reactions to include all these environmental factors poses a significant challenge. A simplified approach developed by Norskov et al. has been successful in describing the thermodynamics of electrochemical reactions using the DFT calculated energetics.[67-70] Within this Computational Hydrogen Electrode (CHE) model, the free energy change (ΔG) between two states at the electrochemical environment is calculated according to the following steps:

(1) At applied potential (U) = 0 V, the chemical potential (the free energy per H) for the reaction ($H^+ + e^-$) is equal to that of $1/2H_{2(g)}$.[6,67,69,71]

(2) The effect of applied potential on the free energy change between states that involve an electron transfer is determined by the term: –eU, where U is the electrode potential.[15,30,34,41,55,67,70]

(3) The pH correction on the free energy of H^+ ions are calculated as[5,40,41,62,68,70,72,73] $G_{(pH)} = -k_B T \ln[H^+] = k_B T \ln 10 \times pH$. Thus, the change in free energy (ΔG_0) at (U) = 0 V is calculated as[6,11,15,21,61,68,71,72,74]

$$\Delta G_0 = \Delta E + \Delta ZPE - T\Delta S \quad \textbf{(Equation 6)}$$

where ΔE is the binding energy of adsorbed species calculated using DFT. The zero-point energy corrections (ΔZPE) and entropy differences (ΔS) are calculated within a harmonic approximation for adsorbed species.[15] The influence of U on the free energy change of the reaction involving an electron is calculated using the following equation: [15,30,34,55,67,70]

$$\Delta G_U = \Delta G_0 - neU \quad \textbf{(Equation 7)}$$

where n is the number of electrons transferred in the reaction. When the effect of the pH value of the electrolyte is taken into account, the following equation is used to calculate the change in free energy:[5,24,31,39-41,55,62,68,73,75,76]

$$\Delta G = \Delta G_U + \Delta G_{(pH)} = \Delta G_0 - neU + k_B T \ln 10 \times pH \quad \textbf{(Equation 8)}$$

where k_B is Boltzmann constant. When the effect of solvent is considered, the energy correction arising from the solvation effect (Δ_{Sol}) was defined as: [31,77]

$$\Delta_{sol} = E_{tot} - E_{(sur+adsorbate)} - E_{solvent} + E_{(sur+solvent)} \quad \textbf{(Equation 9)}$$

where E_{tot}, $E_{(sur+adsorbate)}$, $E_{solvent}$, and $E_{(sur+solvent)}$ represent the computed total energies of the surface with adsorbates as well as the solvent layer, surface with adsorbates, solvent layer, and clean surface with solvent layer, respectively. The following equation was used to calculate the change of free energy when the solvation effect was considered.[31,77]

$$\Delta G = \Delta G_U + \Delta G_{(pH)} + \Delta_{Sol}$$
$$= \Delta G_0 - neU + k_B T \ln 10 \times pH + \Delta_{sol} \quad \textbf{(Equation 10)}$$

Additionally, other methods such as the constant electrode potential (CEP) method have been developed to study the potential dependence of electrochemical reactions.[78-81] In such methods, the Fermi energy is adjusted to a target value by varying the number of electrons in the system during each step of the geometry optimization, which enables to fix the work function (ϕ) of the system and consequently the electrode potential (U). Thus, the U value remains constant during the electrochemical reaction. The U value of the electrode can be calculated by relating the ϕ value of the system to the experimental work function of the standard hydrogen electrode (SHE) as follows,[79,80]

$$U = \frac{\phi - \phi_{SHE}}{e} \quad \textbf{(Equation11)}$$

A value of ~4.3 eV has been proposed for ϕ_{SHE} by Anderson et al.[82,83] in their studies of various electrochemical interfaces.

The activation energy (E_a), defined as the energy difference between the transition state and the initial state, of a chemical reaction can be calculated using the climbing image nudged elastic band (CI-NEB) or dimer methods within the DFT approach.[4,26,84-86] The Brønsted–Evans–Polanyi (BEP) relations provide a correlation between kinetics with thermodynamics of a chemical reaction and can be derived from the transition state (TS) energy and reaction energy. Thus, BEP scaling relations can often be used to estimate the activation energy barrier instead of performing computationally expensive explicit transition state calculations.[87,88] Reaction network investigations with activation energies of elementary steps obtained from explicit transition state search using the methods such as CI-NEB provide a complete and accurate picture of the reactivity of catalysts. However, such investigations are often computationally very demanding. In this regard, the scaling relation and descriptors-based approach proposed by Norskov and co-workers[88-92] are advantageous for accelerating the catalyst discovery.

Table 1 summarizes the typical methodology used for DFT or DFT+U_{DFT}[25,31,50,76,93-95] calculations of TMC and TMN surfaces. For DFT+U_{DFT} calculations, the value of Hubbard U_{DFT} parameter is determined by either comparing the DFT calculated electronic bandgap with the experimental value or by linear response (LR) theory.[96-98] The low index surfaces in DFT calculations are usually modelled using (3 × 3) and/or (4 × 4) surfaces, which are large enough to minimize the lateral interactions between the adsorbates. For such surfaces, k-points between 5 × 5 × 1 to 3 × 3 × 1 are sufficient for the Brillouin-zone integration. The interactions between electrons and nuclei are treated with all-electron-like projector augmented-wave (PAW) potentials. The electronic exchange and correlation effects are typically described within the generalized gradient approximation (GGA) using Perdew–Burke–Ernzerhof (PBE), revised PBE (RPBE), or Perdew-Wang (PW91) functionals including van-der Waals (vdW) correction to account for the dispersion forces. PBE and PW91, two of the most widely used functionals, produce similar results and trends for many simple properties, such as lattice constants, bulk moduli, and atomization energies. These functionals have also been regularly used to calculate more complex properties of materials, including the catalytic properties of TMCs and TMNs.[16,23,34,36,61,99]

3. Electrochemical Reactions

3.1 Hydrogen Evolution Reaction (HER)

The water electrolysis reaction (i.e., $H_2O \rightarrow H_2 + 1/2O_2$), which involves the HER and OER half-reactions, is a promising alternative to steam methane reforming (SMR) to produce CO_2-free hydrogen. Production of CO_2-free hydrogen with renewable electricity is crucial for enabling sustainable and fossil fuel free energy technologies.[11,15]

HER is the cathodic half-reaction of water electrolysis ($2H^+ + 2e^- \rightarrow H_2(g)$).[15,100] In acid electrolyte, two reaction mechanisms of HER have been proposed, namely the Volmer-Heyrovsky and Volmer-Tafel reaction pathways,[5,62,101] both of which occur in two steps.[5,14,15] Along the Volmer-Heyrovsky pathway (**Figure 1(a)**), the Volmer step corresponds to hydrogen adsorption to the surface of the catalyst, i.e., $H^+ + e^- + {}^* \rightarrow H^*$ (where * represents the hydrogen adsorption site). In the Heyrovsky step,[62] a proton from the solution reacts with an electron and an adsorbed H on the surface to form H_2, i.e., ion-atom recombination: $H^* + H^+ + e^- \rightarrow H_2(g) + {}^*$. Along the Volmer-Tafel reaction pathway, two adsorbed hydrogen atoms on the surface of a catalyst combine and evolve as molecular hydrogen in the Tafel step, i.e., atom-atom recombination: $H^* + H^* \rightarrow H_2(g) + 2^*$. In alkaline electrolyte, the typical process of HER can be summarized in two steps, known as the Volmer–Heyrovsky reaction pathway (**Figure 1(b)**):[11,101] (1) $H_2O + e^- + {}^* \rightarrow H^* + OH^-$ and (2) $H_2O + H^* + e^- \rightarrow H_2 + OH^- + {}^*$.

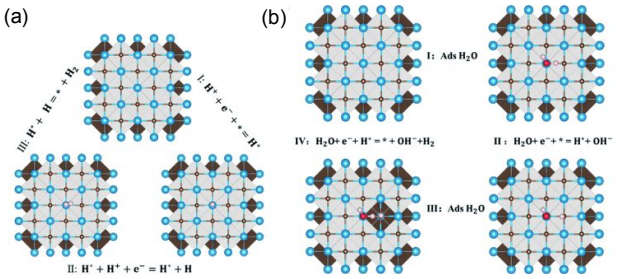

Figure 1. The mechanism of hydrogen evolution reaction (HER) in (a) acidic and (b) alkaline media. Reproduced from ref. 21 with permission from the Royal Society of Chemistry, Copyright 2019.

According to the Sabatier principle, when hydrogen binds too strongly with the catalyst surface, it leads to hydrogen poisoning that leaves no free sites for further adsorption. [5,11,15] On the other hand, if hydrogen binds too weakly to the catalyst surface, unduly high overpotentials are necessary for proton adsorption. Hence, an ideal catalyst should have optimal H^* binding energies between these two extremes.[5,6,15,21] From the perspective of both theory and experiment, the Gibbs free energy change of adsorbed hydrogen (ΔG_{H^*}) is the key factor for describing the HER activity of an electrode in acidic electrolysis.[11,12,14,15] In alkaline environments, besides thermodynamic ΔG_{H^*}, the kinetic barrier to water dissociation may also govern the overall reaction rate, in addition, OH binding energies may be an important factor.[14] Binding energy

(and the Gibbs free energy) values of the HER intermediates, which can be routinely calculated using DFT, largely rely on the geometric and electronic structures of the electrocatalysts. Therefore, DFT is uniquely positioned to be utilized as a screening tool for the discovery of new HER electrocatalysts. At present, most DFT studies of TMC and TMN based catalysts often treat ZPE and S as constants. However, for some sytemes, especially 2D MXene, this may not be valid for describing the HER. For example, in HER calculations, while ZPE is 0.04 eV for the hydrogen atom adsorbed on the Pt surface, ZPE is 0.17 eV for the carbon-based catalysts. Such a difference in ZPE can potentially lead to significant errors with respect to the optimal range of ΔG_{H^*} values.[69,102,103] Therefore, ZPE should not be treated as a constant for predicting the HER activity over TMC and TMN catalysts.

Extensive DFT calculations have been performed for HER over TMC and TMN catalysts,[5,6,9,11-14,16-21,60-62,65,71,72,85,100,101,104-119] and selected results are summarized in **Table 2**. The adsorption of atomic hydrogen has been used as a probe to compare the HER activities of various TMC surfaces, including β-Mo_2C(0001) and the (111) surfaces of TiC, VC, NbC, and TaC.[13] The DFT calculated results demonstrate that hydrogen is adsorbed more strongly on the metal-terminated carbide surfaces compared to the parent metal surfaces (**Table 2**), which is partially attributed to the tensile strain that occurs in the carbide surfaces when carbon incorporates into the corresponding metal lattice. On the contrary, when hydrogen is adsorbed on C-terminated carbide surfaces, the adsorption energies are much weaker than the corresponding closest-packed parent metal surfaces, except for some cases where very stable C-H species are formed (**Table 2**). The DFT results indicate that the hydrogen adsorption energy can be correlated to the d-band center of the carbide surfaces, provided that the contributions of the d-states resulting from hybridization with non-bonding C-s states are minimized.

Hydrogen coverage is reported to play a role in the binding energies of hydrogen on TMC surfaces. When TMC catalysts, including WC, Fe_3C, B_4C, Mo_2C, and TiC, were assessed for the effect of surface hydrogen coverage on catalyst activity, the calculated results suggested that metal carbide surfaces were more susceptible to the coverage effects, in comparison to pure metal counterparts.[14] As a note, the hydrogen coverage on these surfaces ranged from 1/4 to 1/2 monolayer hydrogen (H_{ML}), with the exception of Fe_3C(001), which ranged from 1/6 to 1/3 H_{ML}. The results showed weakened HBE due to lateral interactions (**Table 2**), in contrast to a strengthening trend that was often observed on the corresponding parent metals. This correlated with increased exchange current densities for the HER on metal carbides relative to the parent metal counterparts. The results also showed that the HER activity of monometallic carbide catalysts was between low activities observed for early transition metals and high activities observed for PGMs.

Platinum (Pt) and palladium (Pd) overlayers on W- and C-terminated WC(0001) surface, at coverages ranging from 0.25 ML to 2 ML, have been studied using DFT.[12] It was demonstrated that both Pt and Pd overlayers showed strong adhesion to the WC support, which was accompanied by the modification of the electronic structure of surface atoms. As a result of increased overlayer stability, these PGM overlayers were predicted to form on the W-terminated WC(0001) surface rather than on C-terminated WC(0001). The electronic structure of Pt and Pd monolayers on both W- and C-terminated surfaces was determined by the ligand and strain effects, however, upon deposition of a second metallic layer, the strain effect overtook the ligand effect, and the lattice mismatch became the main factor that determined the electronic structure of the supported Pt and Pd overlayers. The calculated values of the

Table 2 DFT calculated hydrogen binding energy (HBE, eV) and Gibbs free energy change (ΔG, eV) on TMC and TMN catalysts and catalyst supports. (1) metal-terminated carbide surfaces and C-terminated carbide surfaces were denoted as M-ter and C-ter, respectively, in Ref.[13]; (2) 1/4, 1/2, 1/9, 3/9 and 6/9 etc. represent the hydrogen coverage on the catalyst surface;

Species	HBE (eV)			
acidic media	M-ter	C-ter	-	-
Mo_2C(0001)[13]	-3.32	-3.00	-	-
	-	-3.36 (C-H)	-	-
Mo(110)[13]	-3.04	-	-	-
Pt(111)[13]	-2.66	-	-	-
NbC[13]	-3.37	-	-	-
Nb[13]	-3.20	-	-	-
TaC[13]	-3.40	-3.92(C-H)	-	-
Ta[13]	-3.28	-	-	-
TiC[13]	-3.58	-	-	-
Ti[13]	-3.37	-	-	-
WC(0001)[12]	-3.29	-3.47	-	-
Pt_{ML}/WC(0001)[12]	-2.57	-3.09	-	-
Pt_{2ML}/WC(0001)[12]	-2.87	-2.75	-	-
Pd_{ML}/WC(0001)[12]	-2.51	-2.56	-	-
Pd_{2ML}/WC(0001)[12]	-2.94	-2.86	-	-
Pt(111)[12]	-2.70	-	-	-
Pd(111)[12]	-2.77	-	-	-
Species	HBE (eV)[14]			
acidic media (H_{ML})	1/4	1/2	-	-
B_4C(111)	-0.69	-0.46	-	-
TiC(001)	-0.30	-0.22	-	-
Fe_3C(101)	-0.62	-0.49	-	-
Mo_2C(101)	-0.76	-0.42	-	-
WC(0001)	-0.85	-0.60	-	-
Species	HBE (eV)[16]			
acidic media (H_{ML})	1/9	3/9	6/9	-
PdH(111)	0.01	-	-	-
PdH/NbN(111)	-0.13	0.08	-0.20	-
PdH/VN(111)	0.21	0.12	0.66	-
Pd/VN(111)	-0.64	-0.67	-0.50	-
Species	ΔG_H (eV)[5]			
acidic media (H_{ML})	1/8	2/8	3/8	4/8
TiC_2	0.76	0.52	0.85	0.50
VC_2	0.49	0.47	0.43	0.36
NbC_2	0.14	0.15	-0.001	-0.004
TaC_2	0.11	0.22	-0.06	0.11
MoC_2	-0.001	0.10	0.22	0.45

HBE (**Table 2**) on the studied metal overlayers were correlated to experimental values of exchange current densities (**Figure 2(a)**). Such correlations revealed a volcano-like feature with both an explanatory and predictive capacity. The obtained results indicated that Pt/WC showed HER activity comparable to that of Pt and thus was identified to be a promising candidate to replace bulk PGM electrocatalysts for the HER.

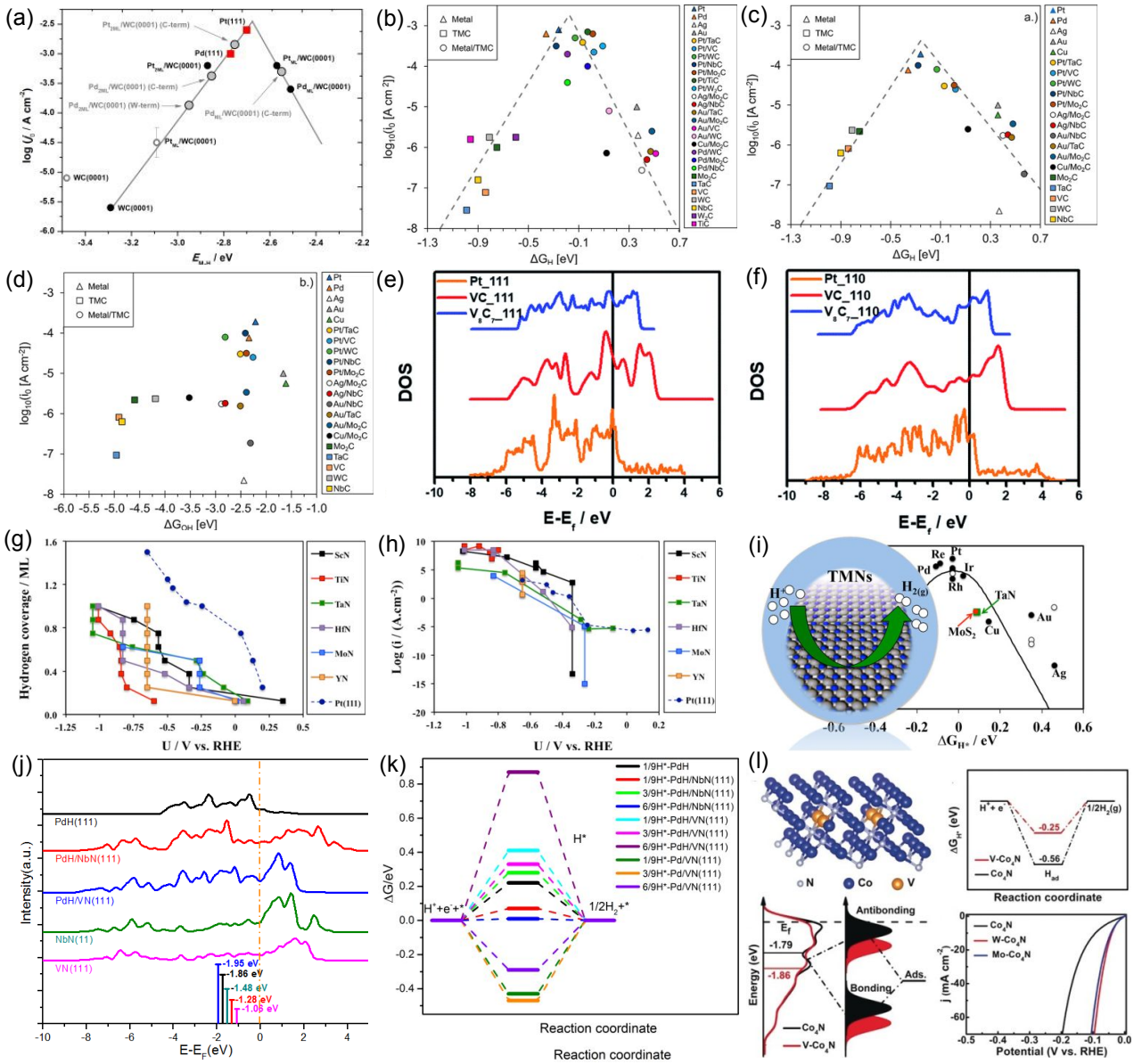

Figure 2. (a) Volcano relationship between HBE and exchange current density for HER. Reproduced with permission from ref. 12 from Elsevier, Copyright 2013; (b) Volcano relationship of HER activity as a function of ΔG_H in acidic medium, (c) Volcano relationship of HER activity as a function of ΔG_H in alkaline medium, (d) alkaline HER activity as a function of ΔG_{OH} on metals, TMCs, and metals-modified TMCs. Reproduced with permission from ref. 11 from American Chemical Society, Copyright 2019; DFT calculated density of states (DOS) of (e) (110) and (f) (111) surfaces on VC, V_8C_7, and Pt, respectively. Reproduced with permission from ref. 21 from the Royal Society of Chemistry, Copyright 2019; The calculated (g) hydrogen coverage and (h) HER theoretical current densities of the Tafel reaction on the surface of the transition-metal nitrides as a function of the applied potential (U/V vs RHE). (i) Volcano relationship of the HER activity and ΔG_H on TMNs. Reproduced with permission from ref. 15 from American Chemical Society, Copyright 2017; (j) The d-band density of states for PdH(111), PdH/NbN(111), PdH/VN(111), NbN(111), and VN(111) [The vertical orange line represents the Fermi energy (EF) of zero]. (k) DFT-calculated free energy (ΔG) diagrams for HER on PdH, PdH/NbN(111), PdH/VN(111), and Pd/VN(111) surfaces at U = 0 V, where H^* coverages are 1/9, 3/9, and 6/9 monolayer hydrogen (H_{ML}). Reproduced with permission from ref. 16 from Wiley-VcH, Copyright 2020; (l) The configuration of V-Co_4N(111) surface, DFT calculated free energy diagram for the HER on Co_4N and V-Co_4N, DFT calculated DOS on Co_4N and V-Co_4N (d-band

centers also illustrated) and linear sweep voltammetry (LSV) curves of Co_4N, W-Co_4N, and Mo-CO_4N. Reproduced with permission from ref. 17 from Wiley-VcH, Copyright 2018.

Zhang et al.[11] studied the correlation between the experimental HER activity and DFT-calculated binding energies of HER intermediates over a large number of TMC and monolayer metal-modified TMC materials. As shown in **Figures 2 (b) and (c)**, it was found that the HER activity correlated strongly with the DFT-calculated ΔG_H values on TMC and metal-modified TMC surfaces under both acidic and alkaline HER conditions. A volcano-type relationship on metal-modified TMCs indicated that the HBE should be a good descriptor for this class of materials under both electrolyte conditions. The free energy change for hydroxyl binding (ΔG_{OH}) did not exhibit a strong correlation with the measured alkaline HER activity (**Figures 2 (d)**), indicating that ΔG_{OH} was not a good descriptor for HER on TMC and metal-modified TMC materials, and that the adsorbed hydroxyl did not directly participate in the rate-determining step of the alkaline HER.[11]

DFT calculations have also been used to systematically analyze a variety of important catalytic parameters for TMCs of the same parent metal, but with different stoichiometries (M_XC_Y). For example, DFT calculations were performed to study the HER activity of various polymorphs of vanadium carbides.[21] The calculated results showed that V_8C_7 was the most active for the HER compared to V_4C_3 and VC in both acid and alkaline environments. This was attributed to a lower crystal formation energy and more facile formation of carbon defects that increased the specific surface area, as well as a larger V-C bond length and weaker bond strength that contributed to a more desirable HBE and smaller ΔG_{H^*}. Moreover, the calculated d-band density of states on the (110) and (111) surface of VC/V_8C_7 showed a similar electronic signature of surface atoms to Pt (**Figures 2 (e) and (f)**).

DFT calculations were also used as a screening tool to identify stable and active TMN (TM = Sc, Ti, Y, Hf, Ta, and Mo) catalysts for HER.[15] DFT was employed to calculate the free energy change ΔG_{H^*} at various H coverages (from 1/8 to 1 ML) on the (100) surfaces of TMNs, as well as the activation energy of the Tafel reaction to form H_2. The calculated results predicted TaN as a promising HER catalyst with a low overpotential around -0.09 V vs RHE (**Figure. 2(g)**). Meanwhile, the calculated barrier
for the Tafel reaction on TaN was 0.84 eV, which was very close to the value (0.85 eV) on Pt(111). More interestingly, it was also found that the rate of the Tafel reaction on TaN was very similar to that previously reported on Pt(111) at around the equilibrium potential (**Figure. 2(h)**. Thus, TaN was predicted to be a good candidate based on the calculated HER current densities as a function of applied potentials (**Figure. 2(i)**).

TMN materials have also been studied as supports of ML PGM for HER. In one study, the HER activity of Pd supported on NbN and VN was evaluated as a potential catalyst with 2 ML coverage of Pd.[16] Supported Pd was unique from other PGM analogs because of the formation of the Pd hydride (PdH) phase under HER conditions. Consequently, HBE (**Table 2**) and ΔG_{H^*} values (**Figure 2(k)**) for H^* coverage ranging from 1/9 to 6/9 ML were calculated on PdH(111), PdH/NbN(111), and PdH/VN(111), representing the experimental Pd/C, Pd/NbN, and Pd/VN catalysts, respectively. Pd/VN was also considered to address a scenario of incomplete Pd hydride formation on the VN substrate. In agreement with the experimental observations, the calculated results (**Figure 2(k)**) predicted that the HER activity should follow the order: PdH/NbN(ΔG_{H^*} = 0.07) > PdH (ΔG_{H^*} = 0.22) > PdH/VN (ΔG_{H^*} = 0.41) > Pd/VN (ΔG_{H^*} = -0.43).[16] Interestingly, it was noted that the trends in the ΔG_{H^*} values remained the same even at higher coverages of H^* (6/9 H_{ML}) on the PdH(111), PdH/VN(111), PdH/NbN(111) and Pd/VN(111) surfaces. This was also consistent with the d-band center (E_d, **Figure 2(j)**) shift in PdH due to the interaction with the nitride supports. Compared to PdH (E_d = -1.86 eV), PdH/NbN (E_d=-1.28 eV) exhibited a positive shift in E_d, which strengthened the binding for the reaction intermediate H^*. In contrast, PdH/VN (E_d = -1.95 eV) showed a negative shift in E_d, which led to a weakened binding of H^*. Recent studies have suggested that the electronic signature of p orbitals (e. g. p-band center, Fermi-abundance, peak-positions etc) can be used to correlate the catalytic activities of heteroatom doped graphene-based catalysts.[120-123] Thus, a similar strategy would be useful for the design of TMC and TMN based catalysts with C/N atoms exposed to the surface of catalyst nanoparticles.

Chen et al.[17] proposed that by introducing certain transition metals (e.g. V, Mo, and W) to Co_4N, the d-band center could be tailored to manipulate the material as an efficient HER catalyst. As shown in **Figure 2(l)**, the calculations confirmed that doping Co_4N with V, Mo, and W, made water adsorption more favorable in comparison to unmodified Co_4N. Moreover, the ΔG_{H^*} values of V-Co_4N (-0.25 eV), Mo-Co_4N (-0.21 eV), and W-Co_4N (-0.25 eV) were more thermoneutral than that of Co_4N (-0.56 eV), suggesting that metal doping could facilitate the hydrogen adsorption/desorption process. The calculated d-band center (E_d) of Co_4N, V-Co_4N, Mo-Co_4N, and W-Co_4N were -1.79 eV, -1.86 eV, -1.91 eV, and -1.92 eV, respectively, indicating a change in the d-band center after metal doping. The DFT calculations were in good agreement with the experimental results (**Figure 2(l)**) in that V-Co_4N, Mo-Co_4N and W-Co_4N exhibited an overpotential of 37 mV, 44 mV, and 40 mV at 10 mA cm^{-2}, respectively. These overpotentials were all substantially lower than Co_4N. Overall, these results confirmed that the HER catalytic activity of TMN can be effectively modulated by tailoring the d-band center, an insight that should be useful for the design of more efficient TMC and TMN catalysts for HER and other electrochemical reactions.

First-principles calculations have also been accepted to study HER performance on emerging 2D MC_2 (TiC_2, VC_2, NbC_2, TaC_2, MoC_2) MXenes[5], which are a class of two-dimensional inorganic compounds that consist of a few atoms-thick layers of transition metal carbides, nitrides, or carbonitrides, i.e., $M_{n+1}X_nT_x$, here, n = 1-4, M = early transition metals, X = C and/or N, T_x = O, F and OH[18,31,47,48,50,124]. As shown in **Table 2,** the DFT results showed that the ΔG_H^* values of TiC_2 and VC_2 were positive and higher than 0.3 eV at different H^* coverages, which indicated that they were not ideally suited to promote HER. In comparison, the ΔG_H value on TaC_2 was 0.06 e V at 3/8 ML of H,

very close to the value of 0.09 eV reported on Pt. MoC_2, at low H coverage (1/8 ML), was predicted to possess a superior HER activity with an ideal $|\Delta G_{H^*}|$ value of 0.001 eV. In addition, DFT calculations were performed to calculate the activation energies of elementary steps in HER. It was found that the energy barrier of the Heyrovsky step (0.26 eV) was significantly lower than that of both Tafel steps studied (1.49 eV and 1.69 eV) at different reaction pathways for the MoC_2 catalyst, suggesting that the HER of 2D MoC_2 should follow the Volmer-Heyrovsky mechanism. Moreover, Ding et al.[19] also investigated the HER performance of heteroatom X (X = N, B, P, S) doped M_2C MXene (M = Ti, Mo) with and without oxygen functional groups using DFT calculations. Compared with the X-doped pristine M_2C MXene, the calculated results predicted better HER activity over X-doped M_2CT_2 (M = Mo, Ti; T = O). In particular, the calculated ΔG_H^* for N-doped Ti_2CO_2 was 0.087 eV, which suggested that the HER activity of N-doped Ti_2CO_2 should be comparable to the Pt(111) surface (**Figure 3(a)**).

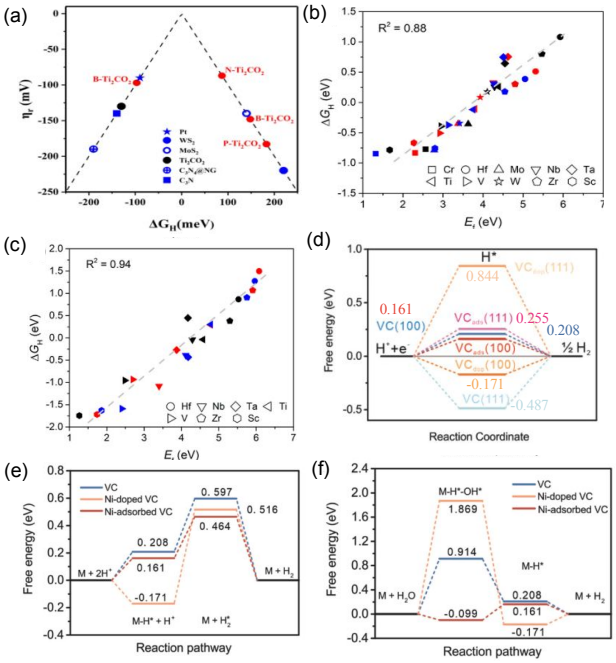

Figure 3. (a) The calculated overpotential ($\eta_r = \pm\Delta G_H/e^-$) vs ΔG_H^* on X-doped Ti_2CO_2 (X = B, N, P, S) and pristine Ti_2CO_2. Reproduced with permission from ref. 19 from Elsevier, Copyright 2020; The calculated linear relationship between free energy of hydrogen adsorption (ΔG_H) and oxygen vacancy formation energy (E_f) of (b) $M_{n+1}C_nO_2$ and (c) $M_{n+1}N_nO_2$. Black, blue, and red, symbols represent M_2XO_2, $M_4X_3O_2$, and $M_3X_2O_2$, respectively. Reproduced with permission from ref. 18 from American Chemical Society, Copyright 2018; Mechanisms of HER enhancement by Ni activated TMCs under acidic and alkaline conditions (d) the calculated ΔG_{H^*}, the calculated schematic and free energy diagrams of the proposed HER pathway on the surface of Ni-GF/VC catalyst in (e) acidic and (f) alkaline media. The VC_{ads} and VC_{dop} represent the Ni-adsorbed VC and Ni-doped VC, respectively. Reproduced with permission from ref. 9 from Wiley-VcH, Copyright 2020.

DFT calculations were also used to screen a large set of 2D oxygen-terminated MXene-based materials, including 30 transition-metal carbides ($M_{n+1}C_nO_2$) and 30 transition-metal nitrides ($M_{n+1}N_nO_2$) to identify potential MXenes with improved HER activity.[18] The screening results showed that the oxygen vacancy formation energy (E_f) scaled linearly with the ΔG_H^* (**Figures 3(b) and (c)**), suggesting that E_f could be used as a descriptor of HER on this class of MXene. These investigations provided new insights into the design of promising MXene based HER electrocatalysts.

In a recent combined experimental and DFT study, Yang et al.[9] proposed a universal strategy to improve the HER performance of TMCs. According to their proposed scheme, the HER activity of TMCs (M = V, Co, Fe, and Cr) could be significantly increased by Ni single atom incorporation on the surfaces of TMCs. Experimental results showed that the TMCs catalysts exhibited superior HER performance in alkaline and acidic electrolyte after introducing the Ni atom into TMCs. DFT calculations were performed on VC(111) and VC(100) surfaces to identify the origin of such enhanced activity of Ni incorporated TMCs. The results showed that the Ni atom energetically favored to be adsorbed on VC(111) and VC(100) surfaces. Furthermore, the calculated ΔG_H^* of Ni-adsorbed VC, Ni-doped VC, and pure VC suggested that Ni-adsorbed VC(100) surface exhibited an optimal HER activity with a small ΔG_H^* value of 0.161 eV (**Figure 3(d)**), and thus the corresponding active site was predicted to be the adsorbed Ni single atom. In addition, the authors also calculated the kinetic energy barriers of a Heyrovsky step and Volmer step on Ni-adsorbed, Ni-doped, and pure VC catalysts (**Figures 3(e) and (f)**). The calculated ΔG_H^* for the Volmer and Heyrovsky steps for a Ni-adsorbed VC catalyst were 0.161 eV and 0.464 eV, respectively. These values were found to be slightly lower than the corresponding values (-0.171 eV and 0.516 eV) on Ni-doped VC catalyst and (0.208 eV and 0.597 eV) on a pure VC in the acidic solution (**Figure 3(e)**). In alkaline electrolyte, the free energy barrier of water dissociation (ΔG_{H2O}) and the ΔG_H^* on Ni-adsorbed VC were also lower than those on the Ni-doped VC and pure VC catalysts (**Figure 3(f)**). These studies indicated that the introduction of the single Ni atom on the surface of the VC could decrease the free energy barrier of the Volmer and Heyrovsky steps in both acidic and alkaline electrolytes.

3.2 Oxygen Evolution Reaction (OER)

The OER is a critical half-reaction of electricity-driven water splitting[24] and is the oxidation process at the anode,[5,22] i.e., $2H_2O \rightarrow O_2 + 4H^+ + 4e^-$ (in acidic media)[21] and $4OH^- \rightarrow O_2 + 2H_2O + 4e^-$ (in alkaline media).[24] In general, in acidic media (**Figure 4 (a)**), the half-reaction proceeds through the following sequential elementary steps:[5,21,125] (1) $^* + H_2O \rightarrow OH^* + H^+ + e^-$, (2) $OH^* \rightarrow O^* + H^+ + e^-$, (3) $O^* + H_2O \rightarrow OOH^* + H^+ + e^-$, and (4) $OOH^* \rightarrow ^* + O_2 + H^+ + e^-$. In alkaline electrolytes, the OER proceeds via the following sequential elementary steps:[22,24,76] (1) $^* + OH^- \rightarrow OH^* + e^-$, (2) $OH^* + OH^- \rightarrow O^* + H_2O + e^-$, (3) $O^* + OH^- \rightarrow OOH^* + e^-$, and (4) $OOH^* + OH^- \rightarrow O_2 + ^* + H_2O + e^-$. Thus, in the first step, an H_2O molecule dissociates into OH^* and H^* in acidic media, or OH^- adsorbs on the catalyst surface and forms

OH^* in alkaline media (step 1). Then, the formed OH^* subsequently undergoes a deprotonation reaction (in acidic media) or reacts with OH^- (in alkaline media) to form O^* (step 2). In the following step, the O^* binds with a second H_2O molecule (in acidic media) or OH^- (in alkaline media) to form the OOH^* intermediate (step 3). Finally, OOH^* undergoes deprotonation reaction (in acidic media) or binds with OH^- (in alkaline media) to form O_2^*, which desorbs from the catalytic sites as O_2(g) leaving the sites free for the next cycle of the reaction (step 4).[22] The change in free energy (ΔG) of step 1, step 2, step 3, and step 4 are denoted as ΔG_1, ΔG_2, ΔG_3, and ΔG_4, respectively. The binding energy (BE) and change in free energy (ΔG) are calculated by using the equations (1) to (10) as described in the introduction. Commonly, the theoretical overpotential (η^{OER}), defined as η^{OER} = max (ΔG_1, ΔG_2, ΔG_3, and ΔG_4)/e − 1.23 V,[5,24,31,76,125,126] is used to evaluate the OER activity of a catalyst (here 1.23 V is the overpotential for water oxidation at ambient conditions (T = 298.15 K, P = 1 bar, pH = 0)).[5,21] Compared with the HER, which consists of two-electron transfer processes, the OER involves four proton-coupled electron transfer reactions (O-H bond breaking and attendant O-O bond formation),[5,24] is kinetically more sluggish, and proceeds at high overpotentials. The sluggish kinetics of OER is considered to be a bottleneck of water oxidation technologies. Hence, OER is the key process that controls the overall efficiency of electrochemical water splitting.

At present, the state-of-the-art OER catalysts are Predominantly PGM-based catalysts (e.g., supported RuO_2 and IrO_2).[5,22-24] The high cost and global scarcity of PGM resources may limit the use of these catalyst materials in OER technologies.[21,23,24] Furthermore, the short-term durability of some PGM-based OER catalysts at reaction conditions presents serious limitations to water oxidation technologies. In particular, RuO_2 is highly unstable under high anodic potentials in acid and alkaline electrolytes, oxidizing to form RuO_4 and dissolving in solution during the OER. Thus, it is of great significance to develop low-cost, stable, and highly efficient OER catalysts as an alternative to precious metal-based catalysts.[5,24]

Many DFT calculations have been performed for OER over TMC and TMN catalysts,[3,5,21-25,31,100,109,125,127-136] and selected results are summarized in Table 3. A fundamental understanding of the OER mechanism and the origin of the reaction overpotential is necessary to rationally design the improved OER performance of TMC and TMN catalysts. **Table 3** summarizes the DFT calculated binding energies (BE) and the change in free energy (ΔG) of OER intermediates (i.e., O_2, O, OH, and OOH) on TMC and TMN materials. DFT calculations were performed to study the OER on various polymorphs of vanadium carbides (including VC, V_4C_3, and V_8C_7).[21] The results showed that the (001) surfaces exhibit higher catalytic performance for OER, compared to other surfaces. However, the calculated overpotentials (η^{OER}) were 1.55, 1.80, and 1.70 V on V_4C_3(001), V_8C_7(001), and VC(001) (**Table 3**), respectively. Such relatively large overpotentials may arise from the strong affinity of reaction intermediates (i.e., O_2, O, OH, and OOH). All of these values were relatively larger when compared to that of RuO_2 (0.37 V) and IrO_2 (0.56 V),[21] suggesting that such classes of vanadium carbides are not ideal for OER.

The electrochemical stability of the transition metal carbides (TMCs, TM = Ti, V, Zr, Nb, Mo, and Ta) over a wide pH and potential range has been investigated by using chronopotentiometry (CP) titration measurements and DFT calculations.[3] It was observed (**Figure 4 (c)**) that the stability of TMCs correlates well to the oxygen binding energy (OBE) of the parent metal, i.e., the higher the stability (higher carbide oxidation potential vs RHE) of TMCs, the higher the DFT-calculated OBE (more negative values) of the parent metal. The correlation demonstrated that all of the studied TMC electrocatalysts have stability for HER/HOR in a large range of pH. Furthermore, the carbides of TaC, TiC, and ZrC were predicted to be stable for ORR or OER.

The OER on the pristine and Co-doped cementite (210) surfaces were studied via the DFT calculations to gain a deeper insight into their OER performances.[22] The DFT calculated change in Gibbs free energies (ΔG) of the elementary steps were used to identify the rate-determining step on undoped and doped cementite (210) surfaces. The results showed that the formation of OOH^* is the rate-determining step, and the ΔG values were 2.78, 2.69, 2.73, 2.73, and 2.75 eV for the four mono-Co-doped and the pure cementite systems (**Table 3**), respectively. The DFT predictions were not consistent with the experimental results, which showed that Co-doped cementite has much lower OER overpotential than pure cementite. Further DFT calculations were performed to calculate the OER free energy diagrams on surfaces with Fe and Co at the same lattice position of cementite. The calculated results (**Table 3** and **Figure 4 (d)**) illustrated that the ΔG for the rate-determining step is 2.35 eV for the Co-doped cementite which is lower than that (2.75 eV) calculated on pristine cementite, implying that the Co-doped cementite catalyzes OER more efficiently and requires a lower overpotential. Furthermore, it was observed that the surface Co sites tend to bind the OER intermediates mildly with a moderate reaction barrier for the rate-determining step of OER, compared with pure cementite. Similar calculations were performed to calculate the OER free energy profiles on Ni- and Mn-doped cementite systems (**Table 3**). The calculated results showed that the ΔG for the rate-determining step were 3.16 eV and 2.01 eV for Mn- and Ni-doped cementite, respectively, suggesting that the OER performance of Ni-doped cementite is superior to Mn and Fe doped systems. The theoretical results were in good agreement with the experimental measurement of OER performance, i.e., Co ≈ Ni > Fe > Mn.

The potential of emerging 2D MC_2 (TiC_2, VC_2, NbC_2, TaC_2, MoC_2) electrocatalysts for the OER has been systematically investigated by extensive DFT calculations.[5] The stability of MC_2 monolayers in electrochemical conditions was studied using surface Pourbaix diagrams (plotting the most thermodynamically stable state under relevant standard hydrogen electrode (U_{SHE}) and pH values) (**Figure 4 (b)**). The calculated U_{SHE} in the acidic medium were 1.91, 1.37, 1.04, 0.86, and 0.38 V for VC_2, MoC_2, TiC_2, TaC_2, and NbC_2, respectively, indicating that these MC_2 monolayers exhibit excellent stability in acid conditions. Theoretically calculated overpotential (η^{OER}) were 0.95, 0.68, 0.93, 0.72, and 0.45 V for TiC_2, VC_2, NbC_2, TaC_2, and MoC_2, respectively, implying that MoC_2 catalyzes the OER

most efficiently among all MC_2 systems. More importantly, the predicted overpotential on MoC_2 is comparable to that on RuO_2 (0.42 V) and IrO_2 (0.56 V), which suggests that MoC_2 could be a candidate to replace precious metal-based catalysts for OER.

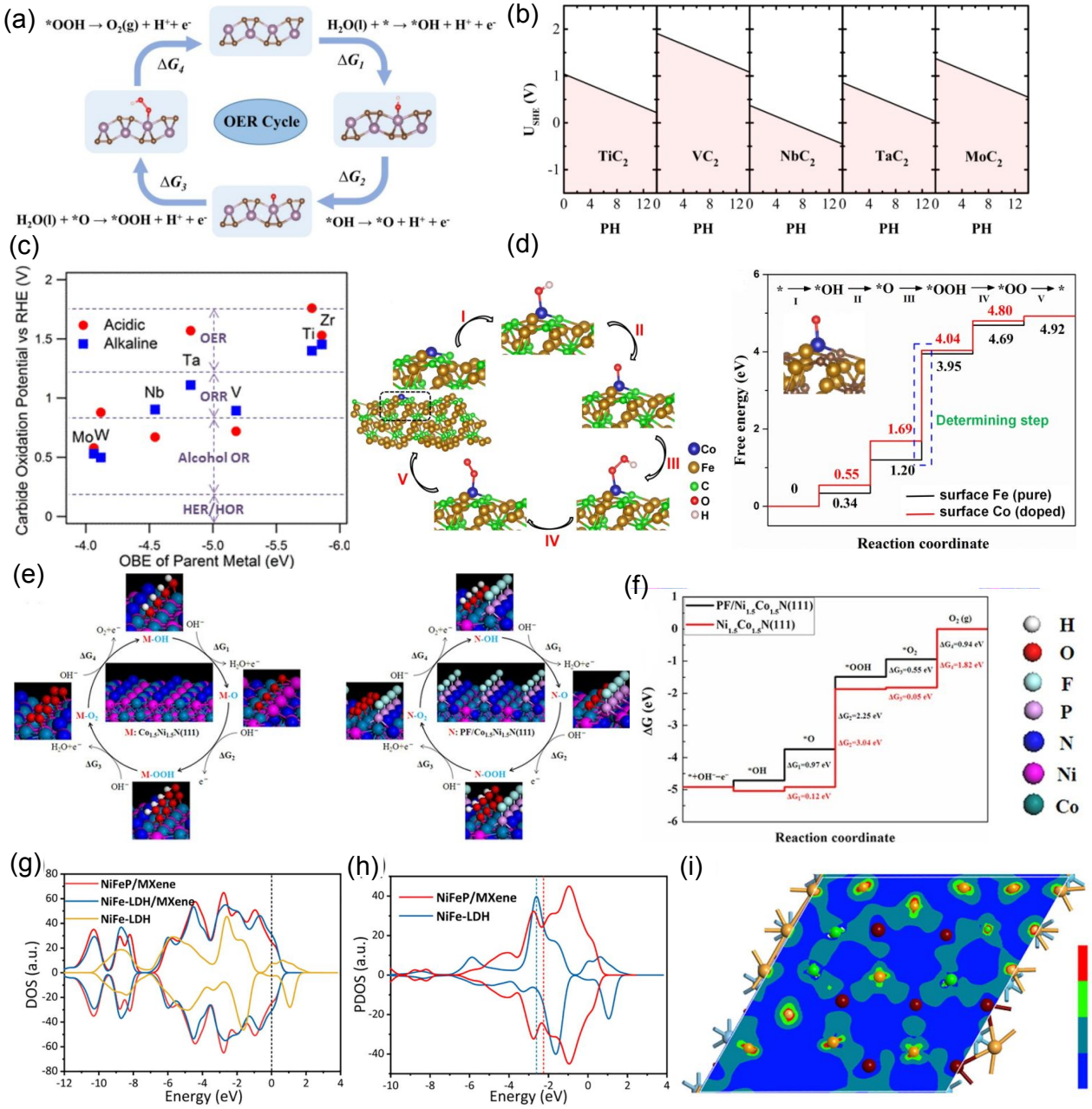

Figure 4. (a) Reaction scheme of the 4e⁻ OER, (b) Surface Pourbaix diagrams of TiC_2, VC_2, NbC_2, TaC_2, and MoC_2 monolayers. Reproduced with permission from ref. 5 from Wiley-VcH, Copyright 2020; (c) The stability (carbide oxidation potential vs RHE) of transition metal carbides (TMCs, TM = Ti, V, Zr, Nb, Mo, and Ta) in acidic (pH = 1) and alkaline (pH = 12) media as a function of parent metal oxygen binding energy (OBE). Reproduced with permission from ref. 3 from American Chemical Society, Copyright 2014; (d) The mechanism and Gibbs free energy changes for the OER elementary steps over pristine and Co-doped cementite. Reproduced with permission from ref. 22 from Elsevier, Copyright 2019; (e) The mechanism and (f) Gibbs free energy changes for the OER elementary steps on $Ni_{1.5}Co_{1.5}N$ and $PF/Ni_{1.5}Co_{1.5}N$ electrocatalysts. Reproduced with permission from ref. 24 from Wiley-VcH, Copyright 2017; (g) The calculated density of states (DOS) for NiFeP/MXene, NiFe-LDH/MXene, and NiFe-LDH (the zero point energy refers to the Fermi level), (h) Local density of states (LDOS) about 3d orbitals of Ni and Fe for the NiFeP/MXene and NiFe-LDH nanosheets (the dashed lines represent the d-band center for the corresponding catalyst) and (i) the charge density

distribution diagrams show the differences between NiFe-LDH and NiFeP/MXene (light red: O, dark grey: C, blue: Ti, pink: H, yellow: Ni, green: Fe, dark red: P). Reproduced with permission from ref. 25 from Elsevier, Copyright 2021.

Core-shell type of material structures have also been explored for OER in an effort to reduce the precious metal loading from the catalyst design. For example, the OER performance of Iridium overlayer on low-cost metal nitrides (Ir/M_4N, M = Fe, Co, and Ni) have been probed by the combination of experimental measurements and theoretical calculations.[23] The experimental results showed that the Ir/Fe_4N core@shell catalyst exhibited good OER activity and stability. The DFT calculated values of [$\Delta G(O^*)$ - $\Delta G(OH^*)$], a descriptor of OER activity, were 1.72, 1.69, and 1.85 eV for IrO_2(110), IrO_2/Ni_4N, and IrO_2/Fe_4N surfaces, respectively. When compared with pristine IrO_2(110), the results showed that the value of [$\Delta G(O^*)$ - $\Delta G(OH^*)$] shifted positively by 0.13 eV on IrO_2/Fe_4N, whilst shifted negatively by 0.03 eV on IrO_2/Ni_4N. The positive shift on IrO_2/Fe_4N brings the OER activity of IrO_2/Fe_4N close to the peak of the volcano. In line with the experimental observations, the DFT calculated results predicted that the OER performance of IrO_2/Fe_4N is superior to IrO_2 and IrO_2/Ni_4N. This study demonstrated that core@shell type structures, such as IrO_2/Fe_4N, could be promising candidates to reduce Ir loading from the catalyst design.

The electronic structure of surface catalytic sites can be modified by doping with promoters. Phosphorus (P) and fluorine (F) co-doping on NiCo bimetallic nitride surfaces have

Table 3 Summary of DFT calculated the binding energies (BE, eV) or the change in free energy (ΔG, eV) of possible OER species (i.e., O_2, O, OH, and OOH) on TMC and TMN catalyst and catalyst supports. Note: ΔG_{Sol} represent the calculated free energies are considering the salvation effect on the selected catalysts.

Models		OH	O	OOH	O_2	η^{OER} (V)
V_4C_3[21]	(001)	ΔG=0.77	ΔG=1.11	ΔG=3.90	-	1.55
	(110)	ΔG=-1.50	ΔG=-0.07	ΔG=-2.82	-	6.51
	(111)	ΔG=-0.42	ΔG=-1.38	ΔG=-2.99	-	6.68
VC[21]	(001)	ΔG=0.64	ΔG=0.76	ΔG=3.90	-	1.70
	(110)	ΔG=-0.97	ΔG=0.02	ΔG=-1.47	-	5.16
	(111)	ΔG=-1.75	ΔG=-1.09	ΔG=-3.97	-	7.66
V_8C_7[21]	(001)	ΔG=0.32	ΔG=0.66	ΔG=3.44	-	1.80
	(110)	ΔG=-0.22	ΔG=-1.38	ΔG=-1.99	-	5.68
	(111)	ΔG=-0.70	ΔG=-1.64	ΔG=2.14	-	4.10
M-Cementite[22]	pure	ΔG=0.34	ΔG=1.20	ΔG=3.95	-	-
	Co dope at Fe1	ΔG=0.38	ΔG=1.30	ΔG=4.08	-	-
	Co dope at Fe2	ΔG=0.38	ΔG=1.32	ΔG=4.01	-	-
	Co dope at Fe3	ΔG=0.35	ΔG=1.25	ΔG=3.98	-	-
	Co dope at Fe4	ΔG=0.36	ΔG=1.24	ΔG=3.97	-	-
	Co dope at Fe	ΔG=0.55	ΔG=1.69	ΔG=4.04	-	-
	Mn dope at Fe1	ΔG=0.14	ΔG=0.64	ΔG=3.80	-	-
	Ni dope at Fe1	ΔG=0.83	ΔG=2.32	ΔG=4.33	-	-
MC_2[5]	TiC_2	ΔG=1.04	ΔG=2.17	ΔG=4.35	-	0.95
	VC_2	ΔG=1.91	ΔG=2.36	ΔG=4.03	-	0.68
	NbC_2	ΔG=0.57	ΔG=2.09	ΔG=4.25	-	0.93
	TaC_2	ΔG=0.86	ΔG=1.94	ΔG=3.89	-	0.72
	MoC_2	ΔG=1.37	ΔG=2.48	ΔG=4.16	-	0.45
IrO_2/M_4N[23]	IrO_2	BE=-0.24	BE=-1.48	-	-	-
	IrO_2/Ni_4N	BE=-0.28	BE=-1.41	-	-	-
	IrO_2/Fe_4N	BE=-0.34	BE=-1.51	-	-	-
PF/$Ni_{1.5}Co_{1.5}N$[24]	$Ni_{1.5}Co_{1.5}N$	-	ΔG=0.12	ΔG=3.16	ΔG=3.21	1.81
	PF/$Ni_{1.5}Co_{1.5}N$	-	ΔG=0.97	ΔG=3.22	ΔG=3.77	1.02
Nb_2CT_2 (T = O, F, and OH) with Pt/Pd single atoms[31]	Nb_2CO_2	ΔG=0.19	ΔG=2.36	ΔG=3.35	BE=-0.29	0.94
	Nb_2CF_2	ΔG=0.22	ΔG=3.02	ΔG=3.65	BE=-0.22	1.53
	Nb_2CO_2-Pd	ΔG=1.79	ΔG=3.24	ΔG=4.59	-	0.56
	Nb_2CO_2-Pt	ΔG=0.51	ΔG=2.85	ΔG=3.75	-	1.01
	Nb_2CF_2-Pd	ΔG=1.37	ΔG=2.79	ΔG=4.47	-	0.45
	Nb_2CF_2-Pt	ΔG=0.52	ΔG=2.27	ΔG=3.92	-	0.97
	Nb_2CO_2-V_O-Pd	ΔG=1.14	ΔG=2.51	ΔG=4.20	-	0.44
	Nb_2CO_2-V_O-Pt	ΔG=0.76	ΔG=2.38	ΔG=3.81	-	0.39
		ΔG_{Sol}=0.88	ΔG_{Sol}=2.31	ΔG_{Sol}=4.18	-	0.64
	Nb_2CF_2-V_F-Pd	ΔG=0.93	ΔG=3.04	ΔG=4.16	-	0.58

	Nb_2CF_2-V_F-Pt	ΔG=0.83	ΔG=2.25	ΔG=3.85	-	0.37
		ΔG_{Sol}=0.80	ΔG_{Sol}=2.39	ΔG_{Sol}=4.02	-	0.40

been explored as a strategy to enhance the OER activity of bimetallic nitrides.[24] DFT calculations were performed to compute the formation energy and explore the stability of P and F heteroatom-doped $Ni_{1.5}Co_{1.5}N$ structures, i.e., PF/$Ni_{1.5}Co_{1.5}N$, and NPF/$Ni_{1.5}Co_{1.5}N$. The calculated results showed that the formation energies were -4.73 eV and -4.60 eV for PF/$Ni_{1.5}Co_{1.5}N$ and NPF/$Ni_{1.5}Co_{1.5}N$, respectively, indicating that P and F co-doping on $Ni_{1.5}Co_{1.5}N$ is energetically more favorable to form PF/$Ni_{1.5}Co_{1.5}N$ rather than NPF/$Ni_{1.5}Co_{1.5}N$. As shown in **Table 3** and **Figures 4 (e)** and **(f)**, DFT calculations demonstrated that the rate-determining step on $Ni_{1.5}Co_{1.5}N$ and PF/$Ni_{1.5}Co_{1.5}N$ was the formation of OOH^* during the OER process. The DFT calculated overpotential was lower on PF/$Ni_{1.5}Co_{1.5}N$ compared to $Ni_{1.5}Co_{1.5}N$, indicating a superior OER activity of the former, in agreement with the experimental results. The PF/$Ni_{1.5}Co_{1.5}N$ hybrid catalyst manifested a low overpotential of 280 mV at 10 mA cm^{-2}, a Tafel slope of 66.1 mV dec^{-1}, and excellent durability in 1.0 m KOH solution in comparison to the IrO_2 catalyst. These findings demonstrated that heteroatom-doping of bimetallic nitride surfaces is a potential strategy to design advanced OER catalyst.

Chen et al.[25] experimentally studied NiFeP/MXene as an OER electrocatalyst. The NiFeP/MXene showed a Tafel slope of 35 mV dec^{-1} and a low overpotential of 286 mV at 10 mA cm^{-2}, which surpassed the performance of several existing NiFe-based catalysts.[137-140] In an alkaline electrolyte, NiFeP/MXene also exhibited a cell voltage of only 1.61 V to achieve a current density of 10 mA cm^{-2}. DFT+U calculations were performed to understand the origin of the excellent OER performance of the NiFeP/MXene electrocatalyst. The calculated density of states (DOS) illustrated that the NiFeP/MXene showed higher DOS than NiFe-LDH near the Fermi level (**Figure 4 (g)**). Furthermore, the calculated local DOS (LDOS) of 3d orbitals of the Ni and Fe atoms in NiFeP/MXene and NiFe-LDH catalysts revealed that the d-band centers of the Ni and Fe atoms in NiFeP/MXene (-2.24 eV) were upward shifted, compared to the single NiFe-LDH (-2.61 eV) system (**Figure 4 (h)**), implying that the introduction of MXene and phosphating process could effectively manipulate the location of the d-band center and electron density distribution (**Figure 4 (i)**) and resulting in an enhanced OER performance.

The OER activity of Pt/Pd SACs on a series of MXene-based catalysts of Nb_2CT_2 (T = O, F, and OH) have been investigated.[31] In one study, DFT+U calculations including solvation effect were performed on Pt/Pd deposited (denoted as Nb_2CO_2-Pt, Nb_2CO_2-Pd, Nb_2CF_2-Pt, Nb_2CF_2-Pd, and $Nb_2C(OH)_2$-Pt, and $Nb_2C(OH)_2$-Pd) and doped (denoted as Nb_2CO_2-V_O-Pt, Nb_2CO_2-V_O-Pd, Nb_2CF_2-V_F-Pt, Nb_2CF_2-V_F-Pd, $Nb_2C(OH)_2$-V_{OH}-Pt, and $Nb_2C(OH)_2$-V_{OH}-Pd) on Nb_2CT_2 MXenes. The calculated formation energy and diffusion barrier of single Pd/Pt atom on Nb_2CT_2 substrates suggested that these O/F-terminated systems possessed high stability and dispersibility, especially for Pt/Pd dopants, whereas the OH-terminated systems were found to be unstable. **Table 3** summarized the calculated ΔG and overpotentials (η^{OER}) of OER on the stable Pt/Pd SACs supported on Nb_2CT_2. The overpotential on doped SACs was much closer to (or even smaller than) that of IrO_2(110) (1.63 V), the best performing OER catalyst. Nb_2CO_2-V_O-Pt and Nb_2CF_2-V_F-Pt showed the lowest voltages of 0.39 and 0.37 V, respectively, which resulted in the lowest η^{OER}. Including the solvation effects in DFT calculations on Nb_2CF_2-V_F-Pt, the best SAC candidate identified in the study, resulted in a small change in the adsorption energy and free energy of OER intermediates but no significant change was observed on the general trend of their inherent catalytic properties (**Table 3**).

3.3 Oxygen Reduction Reaction (ORR)

Electrocatalysis of the ORR is of paramount importance in enhancing the performance of various next-generation energy conversion and storage devices, such as fuel cells, metal-air batteries, and certain electrolyzers. Fuel cells can convert the chemical energy in fuels into electrical energy directly through electrochemical reactions, and possess the ability to reach higher efficiencies than heat engines. The proton-exchange membrane fuel cell (PEMFC) is particularly promising for future use in light transport (e.g., cars) and certain portable applications.[27,141] PEMFCs function as electrochemical engines that convert the chemical energy of H_2 and O_2 directly into electrical energy, with H_2O as the only by product. At the anode, H_2 is catalytically split into protons and electrons ($H_2 \rightarrow 2H^+ + 2e^-$). While the formed protons permeate through an electronically insulating membrane, the electrons travel along an external load circuit to the cathode to create the current output. Simultaneously, a stream of oxygen is delivered to the cathode, where the oxygen is reduced and water molecules are formed as a product.[4] Despite its promise, PEMFC technology suffers from the sluggish kinetics of ORR at the cathode, even when the most efficient Pt/C catalysts are used.[28,30] Pt/C ORR catalysts are not only expensive, but also suffer from Pt dissolution durability, poor tolerance to CO poisoning, and poor corrosion resistance of carbon black in alkaline electrolyte,[29,30] due to which the large-scale commercialization of fuel cell powered technologies is seriously limited.[142] Therefore, it is of great interest to reduce or replace the use of precious metals from the design of ORR catalysts to obtain low cost, durable, corrosion-resistant, and active cathode catalysts.

Depending on the number of overall electrons transferred during the reaction, the ORR can be divided into two classes,[4,26-28,67,84,142-145] that is, $4e^-$ ORR to H_2O/OH^- or $2e^-$ ORR to hydrogen peroxide (H_2O_2). In acid electrolyte, the direct $4e^-$ pathway is $O_2 + 4H^+ + 4e^- \rightarrow H_2O$, and the $2e^-$ pathway plus $2e^-$ pathway is $O_2 + 2H^+ + 2e^- \rightarrow H_2O_2$ followed by $H_2O_2 + 2H^+ + 2e^- \rightarrow 2H_2O$. In alkaline media, the direct $4e^-$ pathway is $O_2 + 2H_2O + 4e^- \rightarrow 4OH^-$, and the $2e^-$ pathway plus $2e^-$ pathway is $O_2 + H_2O + 2e^- \rightarrow OOH^- + OH^-$, followed by $OOH^- + H_2O + 2e^- \rightarrow 3OH^-$. Alternatively, hydrogen peroxide can be the end product of $2e^-$ ORR. In acidic medium, the $2e^-$ pathway is $O_2 + 2H^+ + 2e^- \rightarrow H_2O_2$, and In

alkaline medium, the $2e^-$ pathway is $O_2 + H_2O + 2e^- \rightarrow OOH^- + OH^-$.

Thus, the overall ORR proceeds through either a direct four electron-proton ($4e^-$) transfer step or two-step of two electron-proton ($2e^- + 2e^-$) transfer by reducing O_2 to H_2O (H_2O_2) or OH^-. In acid electrolyte, the direct $4e^-$ pathway proceeds via a dissociative pathway.[27,145-147] The dissociative route follows the reactions, (1) $O_2 + {}^* \rightarrow O^* + O^*$, (2) $O^* + H^+ + e^- \rightarrow OH^*$, and (3) $OH^* + H^+ + e^- \rightarrow H_2O + {}^*$. In contrast, the $4e^-$ pathway of two-step $2e^-$ transfer includes two possible mechanisms, the associative and peroxo pathways. The associative pathway follows:[27,143-145,147] (1) $^* + O_2 + H^+ + e^- \rightarrow OOH^*$, (2) $OOH^* + H^+ + e^- \rightarrow O^* + H_2O$, (3) $O^* + H^+ + e^- \rightarrow OH^*$, and (4) $OH^* + H^+ + e^- \rightarrow {}^* + H_2O$. The second possible mechanism is the peroxo pathway, which is a competitive reaction to the step (2) in the associative pathway.[27] In this step a proton may attack the oxygen directly bound to the surface, resulting in the parasitic formation of H_2O_2. The peroxo pathway thus follows:[143,144,146] (1) $^* + O_2 + H^+ + e^- \rightarrow OOH^*$, (2) $OOH^* + H^+ + e^- \rightarrow HOOH^*$, (3) $HOOH^* \rightarrow OH^* + OH^*$, and (4) $OH^* + H^+ + e^- \rightarrow H_2O^*$. In alkaline electrolytes, the direct $4e^-$ pathway includes the following process:[73,75,76,148] (1) $O_2 + {}^* + H_2O + e^- \rightarrow OOH^* + OH^-$, (2) $OOH^* + e^- \rightarrow O^* + OH^-$, (3) $O^* + H_2O + e^- \rightarrow OH^* + OH^-$, and (4) $OH^* + e^- \rightarrow {}^* + OH^-$.

The overall rate of a chemical reaction is often dictated by the most energetically demanding step. The DFT calculated ORR free energy diagrams allow for these steps to be identified as a function of external potential (U).[30,67,142] In these calculations, the thermodynamic limiting potential (U_L) is defined as the highest potential at which all the reaction steps are downhill in free energy[76], and the theoretical overpotential (η^{ORR}) is defined as the difference between the equilibrium potential of U = 1.23 V and the limiting potential.[5,148] Thus, η^{ORR} can be used as a measure of the activity of a catalyst: the lower the η^{ORR} the more active the catalyst, and vice versa. In addition, it is well known that the Gibbs free energy of O_2 cannot be accurately calculated with DFT methods.[5,28,31,148] Hence, the free energy of O_2 is typically evaluated from the Gibbs free energy change of the reaction $2H_2 + O_2 \rightarrow 2H_2O$, which is experimentally determined to be 4.92 eV.[22,24,28,31,73,76]

Several DFT studies have been performed for ORR over TMC and TMN catalysts.[3-5,26-31,67,75,84,100,105,128,133,141-145,147,149-157] **Table 4** provides a summary of DFT calculated the binding energies (BE) of ORR intermediates (i.e., O_2, H, O, OH, and H_2O) and the energetics (heats of reaction ΔH_0, activation energies E_a, and the change in free energy ΔG) of all of the possible ORR elementary reactions on TMC and TMN materials.

DFT based calculations were performed to study the ORR performance of Pt- and Pd-modified TMCs.[4,26] In one study, the adsorption, diffusion, and dissociation of O_2 on a palladium monolayer supported on a TiC(001) (Pd_{ML}/TiC(001)) surface were investigated using ab initio DFT calculations.[4] The strong adhesion of monolayer palladium to the TiC(001) support helped maintain the monolayer configuration and avoid clustering or sintering. The presence of the TiC(001) substrate was also found to strongly modify the electronic structure of the supported Pd, resulting in a similar d-band center as that of Pt(111) (**Figure 5(a)**, -2.38 eV vs -2.39 eV). The supported Pd_{ML} on TiC(001) was found to strengthen O_2 adsorption capacity, resulting in dissociation and diffusion barriers of O_2 comparable to those on a Pt(111) surface. For instance, as shown in **Table 4**, on the Pd_{ML}/TiC(001) (3×3) surface, O_2 preferentially adsorbed at the hollow site with an adsorption energy of -2.20 eV. For the lowest energy path, the energy barriers were 0.48 eV and 0.42 eV for O_2 dissociation and diffusion, respectively. Meanwhile, it was also found that the stronger adsorption energy of oxygen, the lower the dissociation barrier of oxygen on Pd_{ML}/TiC(001), consistent with the Brønsted-Evans-Polanyi (BEP) relationship.[4] Furthermore, O^*(originated from the dissociation of the adsorbed $O_2{}^*$) also preferentially adsorbed at the hollow site with a binding energy of -1.54 eV, which is comparable to the value of -1.50 eV on Pt(111). It was also found that the O diffusion barrier on Pd_{ML}/TiC(001) was much smaller than Pt(111) (0.38 eV vs 0.71 eV). The favorable O_2 dissociation and diffusion predicted from DFT calculations suggested that Pd_{ML}/TiC(001) could be a potential candidate for ORR.

Similar DFT calculations were performed on Pt_n/TiC(001) P(2×2), with various coverages of Pt (1/4 ML, ½ ML, ¾ ML, and 1 ML), and Pt_{ML}/TiC(001) P(3×3) surfaces.[26] The structure-property relationship of the Pt-modified systems was evaluated on Pt_n/TiC(001) via the calculations of activation energy of O_2 dissociation. The activation energy to break the O-O bond was found to decrease with increased Pt coverage for the Pt_n/TiC(001) P(2×2) surface. For Pt_{ML}/TiC(001) P(3×3), (**Table 4**), the energy barrier for O_2 dissociation was 0.36 eV, which was lower than that of Pt_n/TiC(001) P(2×2) (0.81-1.35 eV) and close to the energy barrier (0.37 eV) calculated on the Pt(111) surface. Furthermore, it was found that a decrease of dissociative adsorption energy (more negative) corresponding to the lower dissociation barrier of O_2, which was also in consistent with the BEP relation. Additionally, the authors in this study also calculated the OBE values on TiC(001) for P(2×2) and P(3×3) surfaces (**Table 4**). Compared with the pristine TiC(001) and Pt(111) surfaces, it was found that the Pt_{ML}/TiC(001) P(3×3) surface can effectively dissociate $O_2{}^*$ and release the produced O^* atoms due to its lower O_2 dissociation barrier and weaker OBE. These results suggest that Pt_{ML}/TiC(001) may be a low-cost alternative to Pt/C for ORR catalysis.

A comparative study of structure, electronic properties, and the ORR activity on M_{ML}/WC(0001) (M = Pt, Pd, and Au) was performed using the DFT calculations.[28] The strong interactions between the WC substrate and the supported ML metal resulted in the improved stability of M_{ML}/WC(0001). As shown in Table **4**, the ORR intermediates on Au_{ML}/WC(0001) were moderately bound compared to Pt_{ML}/WC(0001) and Pd_{ML}/WC(0001). The dissociative channel for ORR on M_{ML}/WC(0001) surfaces was found to be kinetically hindered because of the large energy barrier associated with direct O_2 dissociation. Thus, the ORR most likely proceeds via the associative pathway on metal-modified TMC surfaces. The DFT calculated results (**Table 4**) showed that Au_{ML}/WC(0001) could be a possible Pt-free candidate for ORR. On Au_{ML}/WC(0001), the ORR proceeds through O_2 adsorption, its hydrogenation to OOH^*, OOH^* dissociation to O^*, followed by the hydrogenation of O^* to OH^*, and the hydrogenation of OH^* to produce H_2O^*. The rate-determining step was predicted to be the hydrogenation of OH^* to form H_2O^*, and had an activation

energy barrier of 0.83 eV, which is comparable to that on low index Pt surfaces. The final product H_2O^* easily desorbed from the catalyst with a desorption energy barrier of 0.46 eV (**Table 4**), and the surface active sites then recovered to perform the next cycle of ORR on Au_{ML}/WC(0001) catalyst. In contrast, the intermediates O^* and OH^* were found to bind strongly on both Pt_{ML}/WC(0001) and Pd_{ML}/WC(0001) surfaces, which inhibited the recovery of the surface active sites and led to the deactivation of the catalysts. Thus, Au_{ML}/WC(0001) was predicted to be a promising candidate based on the calculated Gibbs free energy change along the dissociative pathway.

The ORR activity of other low-cost materials supported on TMCs has also been investigated. In one such study, DFT calculations including explicit water layers were conducted on graphene (G) and N-doped graphene (NG) supported on Fe_3C(010) and Fe(110), i.e, Fe_3C(010)/G, Fe_3C(010)/NG, Fe(110)/G and Fe(110)/NG.[27] Both Fe_3C and Fe substrates significantly stabilized the ORR intermediates (OOH^*, O^* and OH^*) on G and NG, of which binding on the latter was much stronger than the former. Notably, among the ORR intermediates, the O^* binding affinity was much stronger than other ORR intermediates on these catalytic systems. The OBE followed the order: unsupported system < Fe_3C support < Fe support (**Figure 5(b)**). A correlation was also found between the oxygen binding strength and the Bader charge on adsorbed O, caused by the presence of the substrate (**Figure 5(b)**). As the O binding increased, there was an increasing negative charge on the adsorbed O. The calculated free energy diagrams (**Figure 5(c)**) showed that the calculated overpotentials η^{ORR} were 1.10, 0.78, 0.96, 1.23, and 0.65 V for Fe_3C(010)/G, Fe_3C(010)/NG, Fe(110)/G, Fe(110)/NG, and Pt(111), respectively, suggesting that Fe_3C(010)/NG should be more active for the ORR than Fe-supported NG, and similar to Pt(111). Therefore, Fe_3C(010)/NG was predicted to be a good candidate to replace Pt for ORR catalysis. The Fe_3C/NG system exhibited higher ORR activity than the Fe-supported NG, mainly because of the non-linear tuning of the binding energies of ORR reaction intermediates (i.e. breaking the scaling relation between the adsorption energy of OH^* and O^* ($\Delta_{ads}G(O) = 2\Delta_{ads}G(OH)$) (**Figure 5(c)**). This finding suggested that a heterostructure consisting of an NG overlayer and a substrate with stronger electron-donating properties, between Fe_3C and Fe, may approach or even exceed the ORR activity of the Pt(111) surface.

The electrochemical ORR on two different facets of TiN, including TiN(111) and TiN(200) surfaces, were studied by DFT calculations.[29] The stronger binding of the ORR reaction intermediates: O_2^*, OH^*, and H_2O^* (**Figure 5(d)**) on these surfaces suggested that pure TiN does not efficiently catalyze the ORR.[29]

Different from pure TMNs, DFT calculations performed on overlayer cobalt oxide on cobalt nitride (CoO/CoN) have been shown to significantly promote the ORR.[30] Different facets of two different phases of cobalt nitrides, i.e., the facets of (100), (110), and (111) on rocksalt (CoN_{RS}) and zinc blende (CoN_{ZB}) were considered. The DFT computed η^{ORR} were 1.09, 1.07, and 1.73 V for (100), (110), and (111) facets of CoN_{RS}, respectively, suggesting that the CoN_{RS} would not be suitable as an ORR catalyst. However, on CoN_{ZB}, the calculated η^{ORR} were 1.40, 0.96, and 0.64 V for (100), (110), and (111) facets, respectively, suggesting that CoN_{ZB}(111) was the most active facet for the ORR (**Figure 5(e)**). The rate determining step for which was

Table 4 Summary of DFT calculated binding energies (BE, eV) of possible ORR species (i.e., O_2, H, O, OH, and H_2O) and the energetics (heats of reaction (ΔH_0, eV) and activation energies (E_a, eV) of all of the possible ORR elementary reactions on TMC and TMN catalyst and catalyst supports. The bold font E_a represents the rate-determining step (RDS) of ORR. The activation energy of the rate-determining step of the ORR is 0.79 eV on the Pt(111)[28,84] and 0.80 eV on the Pt(100).[28,84]

ORR species and elementary reactions	Pt_{ML}/TiC(001)[26]	Pd_{ML}/ TiC(001)[4]	Pt_{ML}/ WC(0001)[28]	Au_{ML}/ WC(0001)[28]	Pd_{ML}/ WC(0001)[28]
O_2	BE=-2.35 on P(3 × 3) surface BE=-2.30 on P(2 × 2) surface	BE=-2.20	BE=-1.55	BE=-0.30	BE=-1.37
H	-	-	BE=-2.69	BE=-1.87	BE=-2.76
O	BE=-1.86 on P(3 × 3) surface BE=-1.69 on P(2 × 2) surface	BE=-1.54	BE=-4.01	BE=-2.87	BE=-4.13
OH	-	-	BE=-2.78	BE=-1.83	BE=-3.25
H_2O	-	-	BE=-0.97	BE=-0.46	BE=-0.49
Dissociative path($4e^-$)					
1. $O_2 \rightarrow 2O^*$	ΔH_0=-0.79 **E_a=0.36**	ΔH_0=-0.84 **E_a=0.48**	ΔH_0=-0.38 **E_a=1.14**	ΔH_0=-0.42 **E_a=1.56**	ΔH_0=-0.83 **E_a=1.03**
2. $O^* + H^+ + e^- \rightarrow OH^*$	- -	- -	- -	- -	- -
3. $OH^* + H^+ + e^- \rightarrow H_2O + ^*$	- -	- -	- -	- -	- -
Associative path($2e^-$+$2e^-$)					
1.$O_2{}^* + H^+ + e^- \rightarrow OOH^*$	- -	- -	ΔH_0=-0.36 **E_a=0.84**	ΔH_0=-0.91 E_a=0.31	ΔH_0=-0.56 **E_a=1.14**
2.$OOH^* + H^+ + e^- \rightarrow O^* + H_2O$	- -	- -	ΔH_0=-1.32 E_a=0.28	ΔH_0=-0.69 E_a=0.68	ΔH_0=-1.66 E_a=0.38
3.$O^* + H^+ + e^- \rightarrow OH^*$	- -	- -	- -	ΔH_0=-1.65 E_a=0.22	-

$4.OH^* + H^+ + e^- \rightarrow H_2O^*$	-	-	-	ΔH_0=-1.19	-
	-	-	-	**E_a=0.83**	-

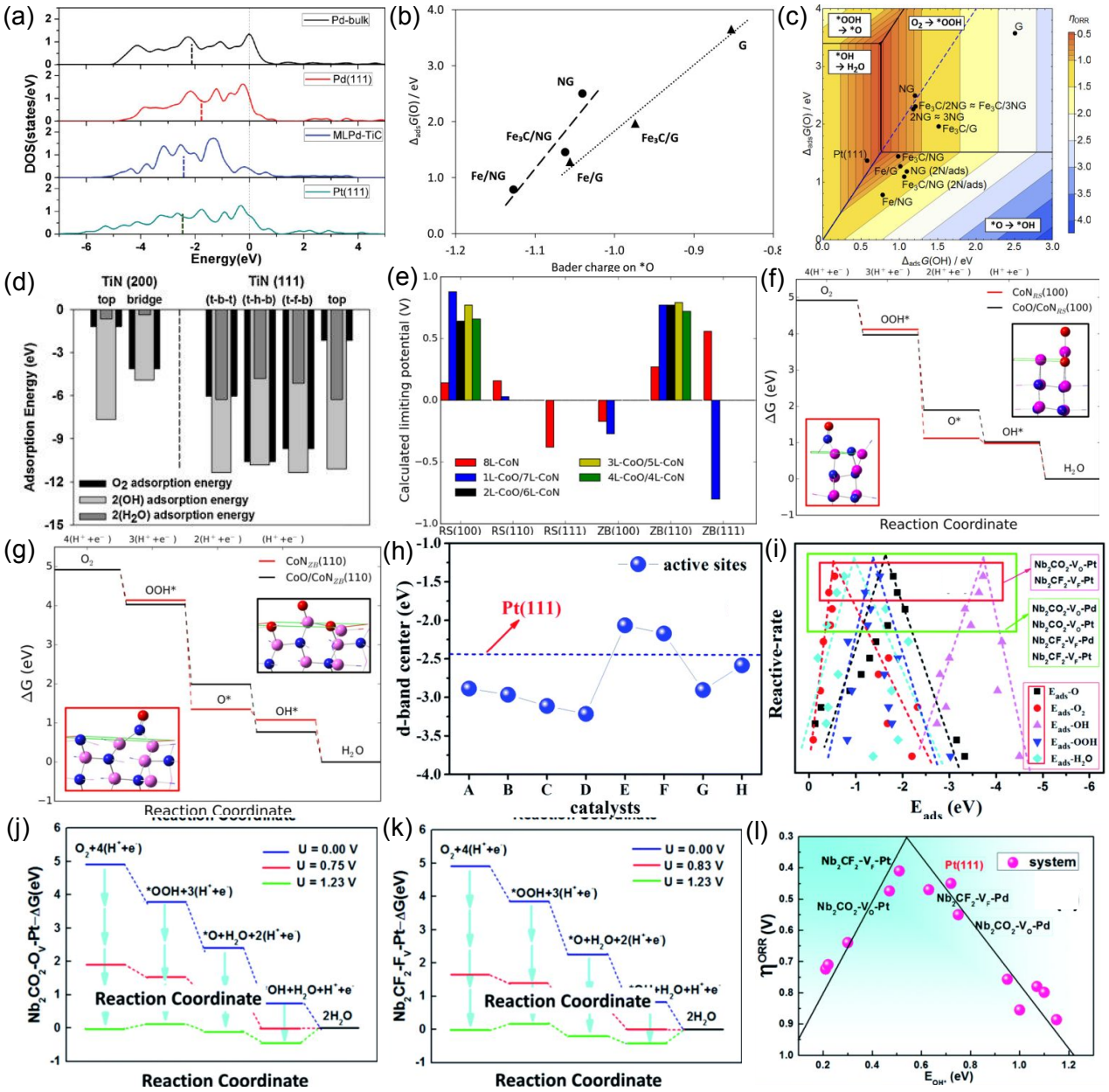

Figure 5. (a) Density of state (DOS) of Pd bulk, Pd(111), Pd ML/TiC(001) and Pt(111), the vertical broken thick lines represent the location of d-band center. Reproduced with permission from ref. 4 from AIP, Copyright 2016; (b) The correlation between the oxygen adsorption Gibbs free energy and Bader charge for the adsorbed O on graphene (G) and N-doped graphene (NG) supported on Fe_3C(010) and Fe(110). (c) The theoretical ORR potential as a function of $\Delta_{ads}G(O)$ and $\Delta_{ads}G(OH)$ on graphene (G) and N-doped graphene (NG) supported on Fe_3C(010) and Fe(110). Reproduced with permission from ref. 27 from American Chemical Society, Copyright 2018; (d) The DFT calculated binding energies of O_2, 2OH, and $2H_2O$ on different sites of TiN(200) and TiN(111) surfaces. Reproduced with permission from ref. 29 from Elsevier, Copyright 2014; (e) The theoretical different facets of ORR limiting potential for RS and ZB CoN. Calculated ORR free energy diagram on (f) RS CoN(100) and (g) ZB CoN(110) with and without a supported overlayer of CoO. Reproduced with permission from ref. 30 from American Chemical Society, Copyright 2018. The calculated d-band center (h) and volcano relationship (i) of Nb_2CO_2-Pd, Nb_2CO_2-Pt, Nb_2CF_2-Pd, Nb_2CF_2-Pt, Nb_2CO_2-V_O-Pd, Nb_2CO_2-V_O-Pt, Nb_2CF_2-V_F-Pd, and Nb_2CF_2-V_F-Pt, respectively. (j) and (k) are the corresponding calculated ΔG of elementary steps along $4e^-$

pathay toward ORR for Nb_2CO_2-V_O-Pt and Nb_2CF_2-V_F-Pt. (l) The calculated volcano plots of η^{ORR} vs. the OH^* binding energy (E_{OH*}) for the selected catalysts. Reproduced with permission from ref. 31 from the Royal Society of Chemistry, Copyright 2020.

predicted to be the reduction of O^* to OH^*. The calculated Pourbaix diagrams showed that the TMN surfaces can be easily oxidized (low oxidation potential ~0.2 V) to form a layer of the corresponding metal oxides under the ORR operating potential. The DFT calculations were performed on CoO/CoN to consider the oxide overlayer formation on CoN at ORR operating conditions. On CoO, the author concluded that only a few top layers of CoN are converted to CoO due to the diffusion-limited kinetics. It was found that the CoO overlayers could significantly alter the calculated ORR limiting potential. Among the CoO/CoN configurations investigated, ML CoO formed on the CoN_{RS}(100) and CoN_{ZB}(110) surfaces possess the high U_L of 0.88 and 0.77 V, respectively. These values of U_L were in good agreement with the experimental value of 0.85 V, leading to a lower η^{ORR} of 0.35 and 0.46 V for CoN_{RS}(100) and CoN_{ZB}(110), respectively, suggesting that the formed oxide layer can significantly improve the performance of ORR on CoN (**Figures 5(f) and (g)**).

The potential of the emerging 2D MXenes (TiC_2, VC_2, NbC_2, TaC_2, MoC_2) as electrocatalysts for ORR has been systematically investigated using the first-principles calculations.[5] The DFT-calculated results showed that each elementary reaction step of ORR on MC_2 was downhill in energy at U = 0 V, suggesting that the ORR should proceed spontaneously. The protonation of adsorbed O_2^* to OOH^* was considered as a potential-determining step (PDS). The calculated η^{ORR} were relatively high, at 0.66, 0.78, and 0.58 V for TiC_2, VC_2, and NbC_2, respectively, indicating an unfavorable ORR on these materials. In contrast, the DFT-calculated η^{ORR} are 0.37 and 0.47 V on TaC_2 and MoC_2, respectively. These values are smaller than the value of η^{ORR} calculated on Pt-based electrocatalysts. Hence, TaC_2 was predicted to be an promising ORR electrocatalyst.

In addition, DFT+U based study has been used to investigate MXene-supported Pt/Pd SACs for ORR, the solvation effect was considered.[31] It was demonstrated that Pt/Pd single atoms were kinetically unstable on OH terminated Nb_2CT_2, while the stable configuration of Pt/Pd was found on O/F terminated Nb_2CT_2. A volcano-like relationship between the d-band center and the binding energies of ORR reaction intermediates was observed on Nb_2C Mexene systems (**Figures 5(h) and (i)**). Among the selected catalysts, the d-band center (E_d) of Nb_2CO_2-V_O-Pt and Nb_2CF_2-V_F-Pt were -2.53 eV and -2.61 eV, respectively, very close to that of Pt(111) (E_d=-2.44 eV), indicating that the above two selected catalysts should possess excellent ORR activity. The DFT calculated ORR free energy diagrams of these two catalysts, Nb_2CO_2-V_O-Pt (**Figure 5(j)**) and Nb_2CF_2-V_F-Pt (**Figure 5 (k)**), suggested that the rate-limiting step was the formation of OH^*, and the corresponding η^{ORR} values were 0.48 and 0.40, respectively. The η^{ORR} of Nb_2CF_2-V_F-Pt was smaller than Pt(111) (0.45 V), and the reaction barrier for the rate-limiting step was comparable to Pt(111) (0.73 eV vs. 0.79 eV), implying that Nb_2CF_2-V_F-Pt should be a promising ORR catalyst (**Figure 5(l)**).

3.4 Nitrogen Reduction Reaction (N_2RR)

Ammonia (NH_3) is one of the most common and important industrial chemicals, used in synthetic fertilizers and other industrial applications.[32,40] The current industrial process for ammonia synthesis still relies on a century-old Haber-Bosch process,[6,32,34,36,39-41] in which NH_3 is produced from the reaction of hydrogen and atmospherically-abundant, inert dinitrogen (N_2) at high pressure and temperature using a promoted metal catalyst.[32,34,39] Conventionally, this process consumes large quantities of energy derived from fossil fuels, and releases a significant amount of CO_2 into the atmosphere. In comparison, the electrochemical nitrogen reduction reaction (N_2RR, $N_{2(g)} + 6H^+ + 6e^- \rightarrow 2NH_{3(g)}$) at ambient conditions using renewable electricity is a promising alternative for nitrogen fixation.[32,35,40,68] This strategy can significantly reduce the energy input, carbon emissions, and dependence on fossil fuel-derived hydrogen.[62] In addition, the NH_3 produced by electrochemical N_2RR can be easily separated from the hydrogen feed gas, and the N_2RR process can be tuned by adjusting the electrolyte, operating potential, pH, etc., to significantly improve the production yield of NH_3. Therefore, the electrochemical N_2RR is considered a promising alternative to the Haber-Bosch process to produce NH_3 at ambient conditions.[32,36,39,40]

The electrochemical N_2RR has attracted much interest in recent years as a preferred way to produce NH_3 at mild conditions. However, the atomistic understanding of reaction mechanisms and catalyst design principles for electrochemical N_2RR remain limited. In general, electrochemical N_2 to NH_3 conversion occurs via two main mechanisms[33,40,41,158-160] (**Figure 6(a)**: One is the dissociative mechanism, where the N≡N triple bond of adsorbed N_2 would first split to form two N atoms adsorbed on the surface. Then the adsorbed N atoms undergo reduction reactions to produce the NH_3. Another is the associative mechanism, where the adsorbed N_2 molecule is first reduced to form $N_2H_x^*$, followed by the N-N bond scission and reduction reactions to form NH_3. Furthermore, the associative pathway involves three possible reaction channels,[159,160] including distal, alternating, and enzymatic pathways (**Figure 6(a)**). On transition metal nitride surfaces, the Mars-van Krevelen (MvK) mechanism has been found to be energetically favorable.[34-36] Along the MvK pathway of N_2RR, a surface N atom is first reduced to NH_3 by protonation and the N vacancy (generated on the surface) is then filled by N_2 adsorption. N_2^* then undergoes reduction reactions to form the second NH_3, either by associative (A-MvK) or dissociative (D-MvK) pathways.[34,35,161] Along the D-MvK mechanism, N_2 adsorption and reduction can proceed on either a single-vacancy or dimer N-vacancy.[34,35,161] In the case of a single-vacancy, one of the N atoms generated from N_2^* dissociation fill the single N-vacancy, while the other N atom will bind on the top of neighboring surface metal sites. The adsorbed N^* atoms then undergo three sequential hydrogenation reactions to form NH_3^*. Finally, NH_3^* desorbs as a final product. On a dimer (N-vacancy pair), this

process only occurs when the nitrogen atom from the gaseous N_2 dissociation filling the single-vacancy is endothermic. In this situation, the produced single-vacancy will remain until another surface N atom through the MvK mechanism produces a second NH_3 molecule, resulting in the second N-vacancy. Then, the N atoms from the dissociation of N_2 fill the two N-vacancies and the active sites on the surface are regenerated.

The overall electrochemical N_2RR process consists of two different kinds of elementary steps: electrochemical steps which involve proton plus electron transfer and non-electrochemical steps that do not involve proton/electron transfer (e.g. N_2 adsorption, N_2 dissociation, and NH_3 desorption).[34,35,161] The largest difference between two adjacent electrochemical steps is defined as the potential-determining step (PDS) with the corresponding largest free energy change values named ΔG_{PDS}.[34,62] The limiting potential, i.e., the bias (U_L) is defined as a potential required to make all electrochemical steps exothermic can be calculated via the following equation:[40,41] $U_L = -\max(\Delta G_1, \Delta G_2, \Delta G_3, \Delta G_4 \ldots, \Delta G_i)/e = -\Delta G_{PDS}/e$, where ΔG_i is the free energy change of each elementary electrochemical step in the NRR. The limiting potential U_L has been used as a well-accepted activity descriptor of N_2RR. However, the non-electrochemical steps cannot be tuned by applying bias (U). Such non-electrochemical steps that determine the overall rate of the N_2RR are the rate-determining step, with the corresponding free energy change values named ΔG_{RDS}.

N_2 is a stable molecule as evidenced by the strong triple bond between nitrogen atoms. Catalysts that have the ability to back donate electrons to the antibonding orbitals (π^*) of N_2 leads to the elongation of N-N bond in N_2^* and thus facilitate the N-N bond cleavage, a bottleneck in N_2RR.[41,162] TMCs and TMNs, which exhibit similar adsorption behaviors as noble metals, are ideally suited in this regard.[32,34] More specifically, the sp hybridized orbital of TMC and TMN materials deviates from parent transition metals, and again hybridizes with the s state of carbon or nitrogen and the d state of the TM at the surface center. After these hybridizations, the excess occupied orbitals have an ability to back donate electrons to the π^* orbitals of N_2. On the other hand, the HER is a competing reaction that likely occurs on the same catalytic sites responsible for the N_2RR. Thus, a good N_2RR catalyst should selectively promote the N_2RR and suppress the HER.[6,34]

Several DFT calculations have been performed for the N_2RR over TMC and TMN catalysts,[6,32-41,62,159-161,163-165] selected results are summarized in **Table 5**. Mo_2C embedded on ultrathin carbon nanosheets (Mo_2C/C) has been reported to show excellent catalytic performance for N_2RR: a high NH_3 yield rate (11.3 μg $h^{-1}mg^{-1}$ Mo_2C) and Faradic efficiency (7.8%). DFT calculations were used to gain an insight into the origin of high activity of Mo_2C/C catalysts. The DFT results showed that N_2 binding is much stronger on Mo_2C (-0.84 eV) compared to MoO_x-Mo_2C (-0.16 eV).[32] This suggested that N_2 activation readily occurs and thus a facilitated N_2RR is expected on Mo_2C. Based on the DFT calculated free energy changes, the limiting potential (U_L) was predicted to be -0.61 V on Mo_2C, and the N_2RR preferably occurred via the following sequential steps (**Table 5(a)**, the distal channel of the associative pathway in **Figure 6(a),** and **Figure 6(b)**): $N_2^* \rightarrow NNH^* \rightarrow NNH_2^* \rightarrow NNH_3^* \rightarrow N^* + NH_3 \rightarrow NH^* \rightarrow NH_2^* \rightarrow NH_3^* \rightarrow NH_3$. Among all the electrochemical steps in the N_2RR on Mo_2C, $NH_2^* \rightarrow NH_3^*$ was found to be the rate-determining step (RDS) with an activation energy of 0.92 eV (**Table 5(a)**). In addition, the free energy and energy barrier of possible pathways for NRR on MoO_x-Mo_2C were also calculated. The calculated results showed that the most favourable pathway proceeds via the following elementary steps (**Table 5(a),** and the alternative channel of the associative pathway in **Figure 6(a)**): $N_2^* \rightarrow NNH^* \rightarrow NNH_2^* \rightarrow NHNH_2^* \rightarrow NHNH_3^* \rightarrow NH^* + NH_3 \rightarrow NH_2^* \rightarrow NH_3^* \rightarrow NH_3$. The rate-determining step (RDS) was predicted to be the desorption of NH_3^* with an energy barrier of 1.53 eV. The calculated results were in good agreement with the experimental observation that Mo_2C/C nanosheets were highly efficient and robust N_2 fixation catalysts. The excellent NRR catalytic activity was mainly attributed to the abundant nitrogen adsorption active sites and unique electronic structure of Mo_2C nanodots, which enabled an efficient cleavage of the N≡N bond.

First-principles DFT calculations were used to explore the possibility of using cubic MoC as an electro-catalyst for NRR.[6] The binding energies of reaction intermediates of N_2RR were calculated on various crystallographic surfaces (including (100), (110), (111), (311), and (111)* surfaces, where * represent Mo-defects) of cubic MoC (**Table 5(b)**). The DFT calculated changes in Gibbs free energies of N_2 adsorption and its direct dissociation to $2N^*$ are -0.40 eV (-2.01 eV), -0.24 eV (-1.55 eV), and -0.14 eV (-0.61 eV) on the MoC(111), MoC(111)* and MoC(311) surfaces, respectively, implying that these surfaces promote the adsorption and dissociation of N_2. The calculated Gibbs free energies for the adsorption of hydrogen atoms ($H^+ + e^- \rightarrow H^*$) and dissociation and adsorption of nitrogen atoms ($^* + 1/2N_2 \rightarrow N^*$) were used to determine surface coverage of N and or H atoms. The results showed that MoC(111), in comparison to the other MoC surfaces studied, was more resistant to the accumulation of H-atoms at low cell potential due to the stronger binding of N relative to H. The free energy changes were also calculated along all possible reaction pathways (via dissociative and associative mechanism) on MoC(111) (**Table 5(a)**). It was found that the potential-determining step (PDS) and the thermodynamic limiting step via the dissociative mechanism were the formations of adsorbed NH_2^* and the desorption of NH_3^* with the free energy change of 0.44 (ΔG_{PDS}) and 0.60 eV (ΔG_{RDS}), respectively. However, for the associative mechanism, the PDS and RDS were the hydrogenation of N_2^* to form NNH^* and the desorption NH_3^*, and the corresponding ΔG_{PDS} and ΔG_{RDS} were 0.28 and 0.60 eV, respectively, suggesting that the N_2RR on the MoC(111) surface is expected to follow the associative mechanism. Furthermore, the effect of carbon vacancies on the N_2RR on the MoC(111) surface, i.e., $MoC_{0.5}$(111) was also studied. The results (**Table 5(b)**) showed that an increase in the Mo:C ratio significantly increased the binding affinity for N_2 and N on (111), (111) *, and (311) surfaces of $MoC_{0.5}$. Such an increase in the Mo:C ratio was found to prevent the accumulation of H-adatoms on $MoC_{0.5}$(111). The DFT calculated the free energy diagrams (**Table 5(a)**) for all of possible N_2RR elementary reactions on $MoC_{0.5}$(111) showed that the overpotentials along the dissociative and associative pathways were -0.51 and -0.52 V, respectively. But NH_3 desorption was found to be energetically facile with ΔG_{RDS} value of 0.49 eV. This study illustrated that the introduction of carbon vacancies on the MoC(111) surface could be beneficial to selective

N_2RR catalysis. Thus, MoC could be a good candidate catalyst for electrochemical N_2RR.

Theoretical calculations, primarily based on DFT methods, have also been performed to investigate the N_2RR activity of γ-MoN. Low index catalyst surfaces such as (001), (100), (101), and (111) were selected to model the N_2RR.[33] The DFT-calculated free energy diagrams showed that γ-Mo_2N(111) promotes the N_2RR via the associative pathway and has a relatively small limiting potential (U_L = -0.70 V, **Table 5(a)**). The facilitated N_2RR on MoN(111) surface is mainly ascribed to the favourable binding of N_2/N intermediates (**Table 5 (b)**), resulting in facile N-N bond scission. The stronger affinity to N* also prohibits the adsorption of H*, an HER intermediate, and suppresses the competing HER.

The electrochemical N_2RR was predicted to proceed via the MvK mechanism on TMN-based catalysts. DFT based calculations have been employed to study the catalytic performance of low index surfaces (rocksalt (100/111) and zinc blende (100/110) surfaces) of ZrN, NbN, CrN, and VN for electrochemical N_2RR.[34] Extensive DFT calculations showed that the N_2RR is not accessible via the associative and dissociative pathways on these nitrides. The dissociation pathway on TMN-based catalysts is hindered due to the high activation energy barrier of direct N_2 dissociation to 2N*. On the other hand, the associative pathway is predicted to be inaccessible

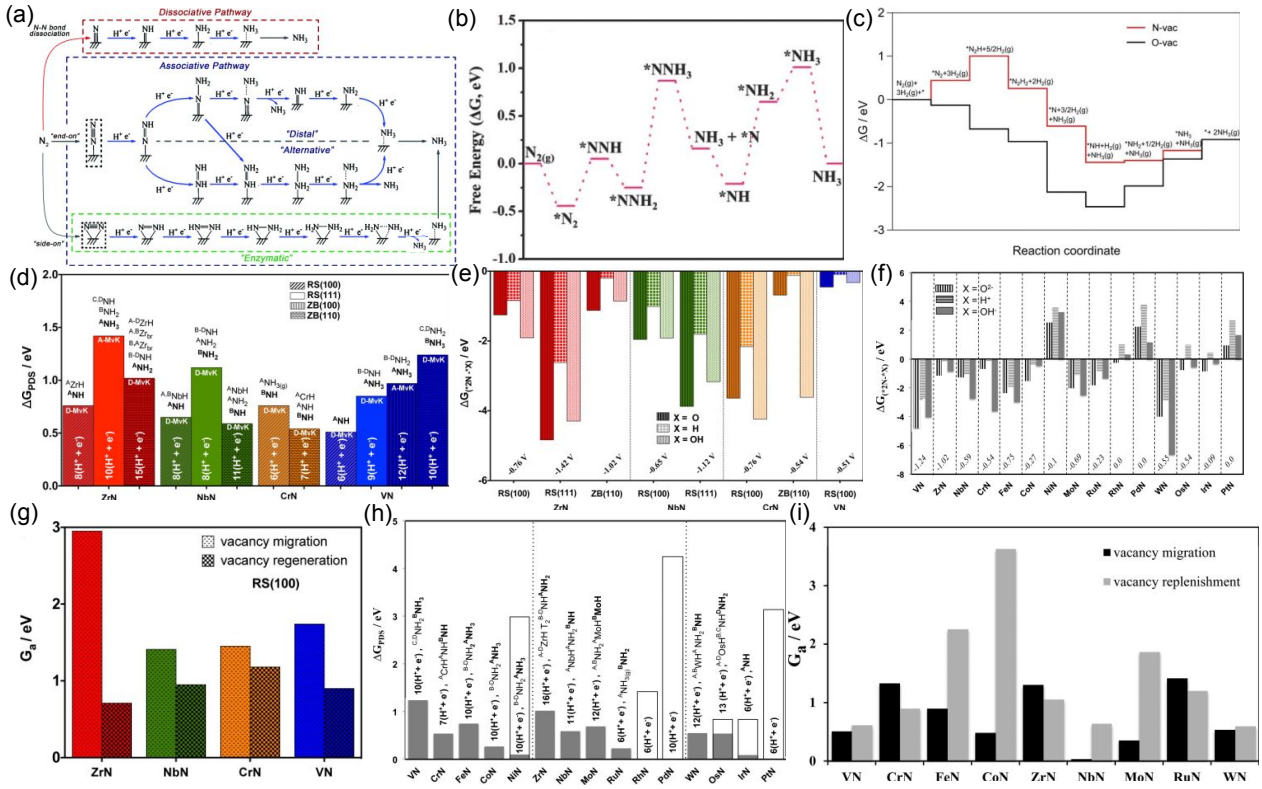

Figure 6. (a) The possible electrochemical NRR mechanism on catalyst surfaces, including the direct dissociative mechanism and the distal, alternating, and enzymatic of associative mechanism. Reproduced with permission from ref. 158 from the Royal Society of Chemistry, Copyright 2019; (b) The calculated Gibbs free energy change of electrochemical NRR on Mo_2C. Reproduced with permission from ref. 32 from Wiley-VcH, Copyright 2018; (c) DFT-calculated free energy diagrams of electrochemical NRR on N-vac and O-vac of the VNO(111) surface at U = 0 V. Reproduced with permission from ref. 36 from Wiley-VcH, Copyright 2019; Comparison of the free energy change (ΔG_{PDS}, the ΔG of the potential-determining step (PDS)) of the most endothermic electrochemical step of NH_3 formation on (d) four different facets of ZrN, NbN, CrN and VN (Reproduced with permission from ref. 34 from American Chemical Society, Copyright 2016) and (h) the (110) facets of the ZB structures of TMN surfaces (Reproduced with permission from ref. 35 from American Chemical Society, Copyright 2017) via MvK mechanism. The number inside (or above) each bar indicates the number of protons and electrons required to complete the catalytic cycle of $2NH_3$ formation. The labels above each bar indicate the species formed prior to PDS, and the bolded texts indicate the species formed right at the PDS. For Figure (d), the most favourable reaction mechanism for filling the N-vacancy, either associative (A-MvK) or dissociative (D-MvK), is specified inside the bar corresponding to each surface; Comparison of the calculated free energy of adsorption of O, OH, or H (relative to 2N) to the surface vacancy of catalytically active nitrides ($\Delta G_{(2N^*-X^*)}$, in eV, where X = O, OH or H) of (e) stable facets of ZrN, NbN, CrN and VN (Reproduced with permission from ref. 34 from American Chemical Society, Copyright 2016) and (f) the (110) facets of the ZB structure of TMNs (Reproduced with permission from ref. 35 from American Chemical Society, Copyright 2017). Free energies are calculated relative to $N_{2(g)}$, $H_{2(g)}$, and $H_2O_{(g)}$. A negative value of $\Delta G_{(2N^*-X^*)}$ indicates that it is thermodynamically favourable to fill the vacancy with N, rather than O, OH, or H. All free energies are evaluated at the calculated onset potential (V vs RHE) for each nitride listed at the bottom of the figure; Calculating and comparing the activation free energy barrier (G_a) of regenerating the catalyst by N_2 dissociation and the migration of nitrogen atoms from the bulk toward the surface to refill the N-vacancy of (g) the RS(100) facet of ZrN, NbN, CrN and VN (Reproduced

with permission from ref. 34 from American Chemical Society, Copyright 2016) and (i) the (110) facet of ZB structures of TMN surfaces (Reproduced with permission from ref. 35 from American Chemical Society, Copyright 2017). If the G_a value of vacancy migration much larger than the vacancy replenishment, the catalyst is likely to be able to regenerate itself and endure the catalytic cycle.

Table 5 Summary of DFT calculated parameters: (a) the energetics (heats of reaction ΔH_0 and activation energies E_a, eV), Gibbs free energy change (ΔG, eV) and (b) binding energies (BE, eV) of possible N_2RR species (i.e., N, N_2H, N_2H_2, N_2, NH, NH_2, NH_3, NNH, NNH_2, NHNH, $NHNH_2$, NH_2NH_2 and N_2H_2) of all of the possible N_2RR elementary reactions on TMC and TMN catalysts and catalyst supports, where * represent Mo-defects; (c) Gibbs free energy change of the potential-determining step (ΔG_{PDS}, eV) in the mechanism of forming the first ammonia molecule via the Mvk mechanism on TMN catalysts; (d) Gibbs free energy change of the potential-determining step (ΔG_{PDS}, eV) and rate-determining step (ΔG_{RDS}) for nitrogen electroreduction to ammonia via both a single and a dimer N-vacancy MvK mechanism on TMN catalysts; (e) Gibbs free energy change of the potential-determining step (ΔG_{PDS}, eV) for formation the second ammonia molecule via an associative or dissociative mechanism, and barrier of N_2 dissociation (E_a, eV) on TMN catalysts. The optimal reaction pathway of the potential-determining step (PDS) or rate-determining step (RDS) are in bold font.

(a) Species	Reaction mechanism	Corresponding reaction steps of N_2RR in different mechanism
Mo_2C[32]	**Distal**	$\mathbf{N_2(g) \xrightarrow{BE=-0.84\ eV} N_2^* \xrightarrow{E_a=0.90\ eV} NNH^* \xrightarrow{E_a=-0.01\ eV} NNH_2^* \xrightarrow{E_a=0.58\ eV} NNH_3^* \xrightarrow{E_a=-0.00\ eV} N^* + NH_3(g) \xrightarrow{E_a=-0.02\ eV} NH^* + NH_3(g) \xrightarrow{E_a=0.92\ eV} NH_3^* + NH_3(g) \xrightarrow{E_a=0.00\ eV} 2NH_3(g)}$
	Alternative	$N_2(g) \xrightarrow{BE=-0.84\ eV} N_2^* \xrightarrow{E_a=0.90\ eV} NNH^* \xrightarrow{E_a=0.15\ eV} NHNH^* \xrightarrow{E_a=0.68\ eV} NHNH_2^* \xrightarrow{E_a=0.54\ eV} NH_2NH_2^* \xrightarrow{E_a=1.35\ eV} NH_2NH_3^* \xrightarrow{E_a=0.} +NH_3(g) \xrightarrow{E_a=0.00\ eV} 2NH_3(g)$
		$N_2(g) \xrightarrow{BE=-0.84\ eV} N_2^* \xrightarrow{E_a=0.90\ eV} NNH^* \xrightarrow{E_a=0.15\ eV} NHNH^* \xrightarrow{E_a=0.68\ eV} NHNH_2^* \xrightarrow{E_a=2.42\ eV} NHNH_3^* \xrightarrow{E_a=0.00\ eV} NH^* + NH_3(g) NH_3^* + NH_3(g) \xrightarrow{E_a=0.00\ eV} 2NH_3(g)$
MoO_x-Mo_2C[32]	Distal	$N_2(g) \xrightarrow{BE=-0.16\ eV} N_2^* \xrightarrow{E_a=0.69\ eV} NNH^* \xrightarrow{E_a=0.22\ eV} NNH_2^* \xrightarrow{E_a=0.55\ eV} NNH_3^* \xrightarrow{E_a=-0.52\ eV} N^* + NH_3(g) \xrightarrow{E_a=0.14\ eV} NH^* + NH_3(NH_3^* + NH_3(g) \xrightarrow{E_a=1.53eV} 2NH_3(g)$
	Alternative	$N_2(g) \xrightarrow{BE=-0.16\ eV} N_2^* \xrightarrow{E_a=0.69\ eV} NNH^* \xrightarrow{E_a=0.48\ eV} NHNH^* \xrightarrow{E_a=0.47\ eV} NHNH_2^* \xrightarrow{E_a=0.58\ eV} NH_2NH_2^* \xrightarrow{E_a=1.65\ eV} NH_2NH_3^* \xrightarrow{E_a=0.} + NH_3(g) \xrightarrow{E_a=1.53\ eV} 2NH_3(g)$
		$\mathbf{N_2(g) \xrightarrow{BE=-0.16\ eV} N_2^* \xrightarrow{E_a=0.69\ eV} NNH^* \xrightarrow{E_a=0.22\ eV} NNH_2^* \xrightarrow{E_a=0.36\ eV} NHNH_2^* \xrightarrow{E_a=0.44\ eV} NHNH_3^* \xrightarrow{E_a=0.38\ eV} NH^* + NH_3(g) NH_3^* + NH_3(g) \xrightarrow{E_a=1.53\ eV} 2NH_3(g)}$
$MoC(111)$[6]	Dissociative	$N_2(g) \xrightarrow{\Delta G=-0.41\ eV} N_2^* \xrightarrow{\Delta G=-2.00\ eV} 2N^* \xrightarrow{\Delta G=-0.47\ eV} N^* + NH^* \xrightarrow{\Delta G=-0.47\ eV} 2NH^* \xrightarrow{\mathbf{\Delta G=0.44\ eV}} NH^* + NH_2^* \xrightarrow{\Delta G=0.43\ eV} 2NH_2^* 2NH_3^* \xrightarrow{\Delta G=0.60\ eV} NH_3^* + NH_3(g) \xrightarrow{\mathbf{\Delta G=0.60\ eV}} 2NH_3(g)$
	Associative	$N_2(g) \xrightarrow{\Delta G=-0.41\ eV} N_2^* \xrightarrow{\Delta G=0.28\ eV} NNH^* \xrightarrow{\Delta G=-0.26\ eV} NNH_2^* \xrightarrow{\Delta G=-1.81\ eV} NH_3^* + N^* \xrightarrow{\Delta G=0.60\ eV} N^* + NH_3(g) \xrightarrow{\Delta G=-0.47\ eV} NH)\xrightarrow{\Delta G=0.24\ eV} NH_3^* + NH_3(g) \xrightarrow{\mathbf{\Delta G=0.60\ eV}} 2NH_3(g)$
		$\mathbf{N_2(g) \xrightarrow{\Delta G=-0.41\ eV} N_2^* \xrightarrow{\Delta G=0.28\ eV} NNH^* \xrightarrow{\Delta G=-0.50\ eV} NHNH^* \xrightarrow{\Delta G=-0.04\ eV} NHNH_2^* \xrightarrow{\Delta G=-0.14\ eV} NH_2NH_2^* \xrightarrow{\Delta G=-0.83\ eV} NH_3(g \xrightarrow{\Delta G=0.60\ eV} 2NH_3(g)}$
$MoC_{0.5}(111)$[6]	Dissociative	$N_2(g) \xrightarrow{\Delta G=-0.59\ eV} N_2^* \xrightarrow{\Delta G=-3.58\ eV} 2N^* \xrightarrow{\Delta G=0.42\ eV} N^* + NH^* \xrightarrow{\Delta G=0.42\ eV} 2NH^* \xrightarrow{\mathbf{\Delta G=0.51\ eV}} NH^* + NH_2^* \xrightarrow{\mathbf{\Delta G=0.51\ eV}} 2NH_2^* \xrightarrow{\Delta} 2NH_3^* \xrightarrow{\Delta G=0.49\ eV} NH_3^* + NH_3(g) \xrightarrow{\mathbf{\Delta G=0.49\ eV}} 2NH_3(g)$
	Associative	$N_2(g) \xrightarrow{\Delta G=-0.59\ eV} N_2^* \xrightarrow{\Delta G=-0.06\ eV} NNH^* \xrightarrow{\Delta G=-0.17\ eV} NNH_2^* \xrightarrow{\Delta G=-2.16\ eV} NH_3^* + N^* \xrightarrow{\Delta G=0.49\ eV} N^* + NH_3(g) \xrightarrow{\Delta G=0.42\ eV} NH g)\xrightarrow{\Delta G=0.26\ eV} NH_3^* + NH_3(g) \xrightarrow{\mathbf{\Delta G=0.49\ eV}} 2NH_3(g)$
Sc_2C[39]	Enzymatic	$N_2(g) \xrightarrow{\Delta G=-2.65\ eV} N^* - N^* \xrightarrow{\Delta G=0.08\ eV} N^* - NH^* \xrightarrow{\Delta G=0.14\ eV} NH^* - NH^* \xrightarrow{\Delta G=1.37\ eV} NH^* - NH_2^* \xrightarrow{\Delta G=-3.58\ eV} NH_2^* - N \xrightarrow{\Delta G=1.20\ eV} NH_3^* - NH_3^* \xrightarrow{\Delta G=0.85\ eV} 2NH_3(g)$
Ti_2C[39]	Enzymatic	$N_2(g) \xrightarrow{\Delta G=-2.82\ eV} N^* - N^* \xrightarrow{\Delta G=-0.02\ eV} N^* - NH^* \xrightarrow{\Delta G=0.29\ eV} NH^* - NH^* \xrightarrow{\Delta G=1.58\ eV} NH^* - NH_2^* \xrightarrow{\Delta G=-3.06\ eV} NH_2^* - \xrightarrow{\Delta G=1.22\ eV} NH_3^* - NH_3^* \xrightarrow{\Delta G=0.79\ eV} 2NH_3(g)$
V_2C[39]	Enzymatic	$N_2(g) \xrightarrow{\Delta G=-2.85\ eV} N^* - N^* \xrightarrow{\Delta G=-0.08\ eV} N^* - NH^* \xrightarrow{\Delta G=-2.00\ eV} NH^* - NH^* \xrightarrow{\Delta G=0.61\ eV} NH^* - NH_2^* \xrightarrow{\Delta G=0.53\ eV} NH_2^* - \xrightarrow{\Delta G=0.66\ eV} NH_3^* - NH_3^* \xrightarrow{\Delta G=1.45\ eV} 2NH_3(g)$
Cr_2C[39]	Enzymatic	$N_2(g) \xrightarrow{\Delta G=-2.04\ eV} N^* - N^* \xrightarrow{\Delta G=0.28\ eV} N^* - NH^* \xrightarrow{\Delta G=-2.49\ eV} NH^* - NH^* \xrightarrow{\Delta G=0.44\ eV} NH^* - NH_2^* \xrightarrow{\Delta G=0.35\ eV} NH_2^* - N \xrightarrow{\Delta G=0.68\ eV} NH_3^* - NH_3^* \xrightarrow{\Delta G=1.40\ eV} 2NH_3(g)$
Fe_2C[39]	Enzymatic	$N_2(g) \xrightarrow{\Delta G=0.12\ eV} N^* - N^* \xrightarrow{\Delta G=0.23\ eV} N^* - NH^* \xrightarrow{\Delta G=-0.52\ eV} NH^* - NH^* \xrightarrow{\Delta G=-0.01\ eV} NH^* - NH_2^* \xrightarrow{\Delta G=-0.94\ eV} NH_2^* - NH_2^* \xrightarrow{\Delta G=-0.37\ eV} NH_2^* - NH_3^* \xrightarrow{\Delta G=-0.11\ eV} NH_3^* - NH_3^* \xrightarrow{\Delta G=0.31\ eV} 2NH_3$ (g)

Zr_2C[39]	Enzymatic	$N_2(g) \xrightarrow{\Delta G = -2.53\ eV} N^* - N^* \xrightarrow{\Delta G = 0.05\ eV} N^* - NH^* \xrightarrow{\Delta G = -2.70\ eV} NH^* - NH^* \xrightarrow{\Delta G = 0.97\ eV} NH^* - NH_2^* \xrightarrow{\Delta G = 0.20\ eV} NH_2^* - N$ $\xrightarrow{\Delta G = 1.16\ eV} NH_3^* - NH_3^* \xrightarrow{\Delta G = 0.48\ eV} 2NH_3(g)$
Nb_2C[39]	Enzymatic	$N_2(g) \xrightarrow{\Delta G = -2.16\ eV} N^* - N^* \xrightarrow{\Delta G = 0.21\ eV} N^* - NH^* \xrightarrow{\Delta G = 0.38\ eV} NH^* - NH^* \xrightarrow{\Delta G = -2.29\ eV} NH^* - NH_2^* \xrightarrow{\Delta G = 0.39\ eV} NH_2^* - N$ $\xrightarrow{\Delta G = 0.51\ eV} NH_3^* - NH_3^* \xrightarrow{\Delta G = 0.98\ eV} 2NH_3(g)$
Hf_2C[39]	Enzymatic	$N_2(g) \xrightarrow{\Delta G = -2.69\ eV} N^* - N^* \xrightarrow{\Delta G = -0.01\ eV} N^* - NH^* \xrightarrow{\Delta G = -3.00\ eV} NH^* - NH^* \xrightarrow{\Delta G = 1.26\ eV} NH^* - NH_2^* \xrightarrow{\Delta G = 0.27\ eV} NH_2^* -$ $\xrightarrow{\Delta G = 1.55\ eV} NH_3^* - NH_3^* \xrightarrow{\Delta G = 0.51\ eV} 2NH_3(g)$
Hf_2C[39]	Enzymatic	$N_2(g) \xrightarrow{\Delta G = -1.94\ eV} N^* - N^* \xrightarrow{\Delta G = 0.22\ eV} N^* - NH^* \xrightarrow{\Delta G = -1.98\ eV} NH^* - NH^* \xrightarrow{\Delta G = 0.01\ eV} NH^* - NH_2^* \xrightarrow{\Delta G = 0.22\ eV} NH_2^* - N$ $\xrightarrow{\Delta G = 0.67\ eV} NH_3^* - NH_3^* \xrightarrow{\Delta G = 1.26\ eV} 2NH_3(g)$
Mo_2C[39]	Distal	$N_2(g) \xrightarrow{\Delta G = -0.67\ eV} N_2^* \xrightarrow{\mathbf{\Delta G = 0.94\ eV}} NNH^* \xrightarrow{\Delta G = 0.17\ eV} NNH_2^* \xrightarrow{\Delta G = -2.26\ eV} NNH_3^* \xrightarrow{\Delta G = 0.15\ eV} N^* \xrightarrow{\Delta G = 0.02\ eV} NH^* \xrightarrow{\Delta G = 0.20\ eV} NH$
	Alternative	$N_2(g) \xrightarrow{\Delta G = -0.67\ eV} N_2^* \xrightarrow{\mathbf{\Delta G = 0.94\ eV}} NNH^* \xrightarrow{\Delta G = 0.26\ eV} NHNH^* \xrightarrow{\Delta G = -0.60\ eV} NHNH_2^* \xrightarrow{\Delta G = -0.05\ eV} NH_2NH_2^* \xrightarrow{\Delta G = -1.50\ eV} NH_2NH$ $\xrightarrow{\mathbf{\Delta G = 0.58\ eV}} 2NH_3(g)$
	Enzymatic	$N_2(g) \xrightarrow{\Delta G = -1.49\ eV} N^* - N^* \xrightarrow{\Delta G = 0.20\ eV} N^* - NH^* \xrightarrow{\Delta G = -0.11\ eV} NH^* - NH^* \xrightarrow{\Delta G = 0.02\ eV} NH^* - NH_2^* \xrightarrow{\Delta G = -1.70\ eV} NH_2^* -$ $\xrightarrow{\Delta G = 0.46\ eV} NH_3^* - NH_3^* \xrightarrow{\Delta G = 1.27\ eV} NH_3^* - NH_3(g) \xrightarrow{\Delta G = 0.51\ eV} NH_3(g)$
Mn_2C[39]	Distal	$N_2(g) \xrightarrow{\Delta G = -0.85\ eV} N_2^* \xrightarrow{\mathbf{\Delta G = 0.89\ eV}} NNH^* \xrightarrow{\Delta G = -0.78\ eV} NNH_2^* \xrightarrow{\Delta G = -0.26\ eV} NNH_3^* \xrightarrow{\Delta G = -0.67\ eV} N^* \xrightarrow{\Delta G = -0.58\ eV} NH^* \xrightarrow{\Delta G = 0.37\ eV} N$ (g)
	Alternative	$N_2(g) \xrightarrow{\Delta G = -0.85\ eV} N_2^* \xrightarrow{\mathbf{\Delta G = 0.89\ eV}} NNH^* \xrightarrow{\Delta G = 0.59\ eV} NHNH^* \xrightarrow{\Delta G = -0.31\ eV} NHNH_2^* \xrightarrow{\Delta G = -0.51\ eV} NH_2NH_2^* \xrightarrow{\Delta G = -1.03\ eV} NH_2NH$ $\xrightarrow{\mathbf{\Delta G = 0.61\ eV}} 2NH_3(g)$
	Enzymatic	$N_2(g) \xrightarrow{\Delta G = -0.89\ eV} N^* - N^* \xrightarrow{\Delta G = 0.25\ eV} N^* - NH^* \xrightarrow{\Delta G = -1.18\ eV} NH^* - NH^* \xrightarrow{\Delta G = -0.62\ eV} NH^* - NH_2^* \xrightarrow{\Delta G = -0.08\ eV} NH_2^* -$ $\xrightarrow{\Delta G = 0.28\ eV} NH_3^* - NH_3^* \xrightarrow{\Delta G = 0.41\ eV} NH_3^* - NH_3(g) \xrightarrow{\Delta G = 0.61\ eV} NH_3(g)$
$Mo_2TiC_2O_2$-Mo_{SA}[40]	**Distal**	$\mathbf{N_2(g) \xrightarrow{\Delta G = -0.05\ eV} N_2^* \xrightarrow{\Delta G = 0.06\ eV} NNH^* \xrightarrow{\Delta G = -1.09\ eV} NNH_2^* \xrightarrow{\Delta G = -0.05\ eV} NNH_3^* \xrightarrow{\Delta G = -0.02\ eV} N^* \xrightarrow{\Delta G = -1.24\ eV} NH^* \xrightarrow{\Delta G = 0.34\ eV}}$ $\mathbf{_3(g)}$
	Alternative	$N_2(g) \xrightarrow{\Delta G = -0.05\ eV} N_2^* \xrightarrow{\Delta G = 0.06\ eV} NNH^* \xrightarrow{\Delta G = -0.93\ eV} NHNH^* \xrightarrow{\Delta G = -0.12\ eV} NHNH_2^* \xrightarrow{\mathbf{\Delta G = 1.04\ eV}} NH_2NH_2^* \xrightarrow{\Delta G = -1.63\ eV} NH_2NH$ $\xrightarrow{\mathbf{\Delta G = 0.58\ eV}} 2NH_3(g)$
$Mo_2TiC_2O_2$-Hf_{SA}[40]	**Distal**	$\mathbf{N_2(g) \xrightarrow{\Delta G = 0.01\ eV} N_2^* \xrightarrow{\Delta G = 0.11\ eV} NNH^* \xrightarrow{\Delta G = -1.08\ eV} NNH_2^* \xrightarrow{\Delta G = -0.13\ eV} NNH_3^* \xrightarrow{\Delta G = -0.12\ eV} N^* \xrightarrow{\Delta G = -1.12\ eV} NH^* \xrightarrow{\Delta G = 0.25\ eV}}$ **(g)**
	Alternative	$N_2(g) \xrightarrow{\Delta G = 0.01\ eV} N_2^* \xrightarrow{\Delta G = 0.11\ eV} NNH^* \xrightarrow{\mathbf{\Delta G = 0.87\ eV}} NHNH^* \xrightarrow{\Delta G = 0.21\ eV} NHNH_2^* \xrightarrow{\Delta G = 0.74\ eV} NH_2NH_2^* \xrightarrow{\Delta G = -2.37\ eV} NH_2NH_3^*$ $\xrightarrow{\mathbf{\Delta G = 0.98\ eV}} 2NH_3(g)$
$Mo_2TiC_2O_2$-Zr_{SA}[40]	**Distal**	$\mathbf{N_2(g) \xrightarrow{\Delta G = -0.04\ eV} N_2^* \xrightarrow{\Delta G = 0.15\ eV} NNH^* \xrightarrow{\Delta G = -1.11\ eV} NNH_2^* \xrightarrow{\Delta G = -0.1\ eV} NNH_3^* \xrightarrow{\Delta G = 0.05\ eV} N^* \xrightarrow{\Delta G = -1.18\ eV} NH^* \xrightarrow{\Delta G = 0.09\ eV}}$ **(g)**
	Alternative	$N_2(g) \xrightarrow{\Delta G = -0.04\ eV} N_2^* \xrightarrow{\Delta G = 0.15\ eV} NNH^* \xrightarrow{\mathbf{\Delta G = 0.91\ eV}} NHNH^* \xrightarrow{\Delta G = -1.78\ eV} NHNH_2^* \xrightarrow{\Delta G = 0.82\ eV} NH_2NH_2^* \xrightarrow{\Delta G = -2.19\ eV} NH_2NH_3$ $\xrightarrow{\mathbf{\Delta G = 0.97\ eV}} 2NH_3(g)$
$Mo_2TiC_2O_2$-Ta_{SA}[40]	**Distal**	$\mathbf{N_2(g) \xrightarrow{\Delta G = 0.23\ eV} N_2^* \xrightarrow{\Delta G = -0.09\ eV} NNH^* \xrightarrow{\Delta G = -0.98\ eV} NNH_2^* \xrightarrow{\Delta G = -0.22\ eV} NNH_3^* \xrightarrow{\Delta G = -0.19\ eV} N^* \xrightarrow{\Delta G = -0.86\ eV} NH^* \xrightarrow{\Delta G = 0.22\ e}}$ $\mathbf{2NH_3(g)}$
	Alternative	$N_2(g) \xrightarrow{\Delta G = 0.23\ eV} N_2^* \xrightarrow{\Delta G = -0.09\ eV} NNH^* \xrightarrow{\mathbf{\Delta G = -0.40\ eV}} NHNH^* \xrightarrow{\Delta G = -0.44\ eV} NHNH_2^* \xrightarrow{\Delta G = 0.42\ eV} NH_2NH_2^* \xrightarrow{\Delta G = -2.84\ eV} NH_2NI$ $\xrightarrow{\mathbf{\Delta G = 0.77\ eV}} 2NH_3(g)$
$Mo_2TiC_2O_2$-W_{SA}[40]	**Distal**	$\mathbf{N_2(g) \xrightarrow{\Delta G = 0.10\ eV} N_2^* \xrightarrow{\Delta G = 0.00\ eV} NNH^* \xrightarrow{\Delta G = -1.15\ eV} NNH_2^* \xrightarrow{\Delta G = 0.22\ eV} NNH_3^* \xrightarrow{\Delta G = -0.50\ eV} N^* \xrightarrow{\Delta G = -1.14\ eV} NH^* \xrightarrow{\Delta G = 0.46\ eV}}$ **(g)**
	Alternative	$N_2(g) \xrightarrow{\Delta G = 0.10\ eV} N_2^* \xrightarrow{\Delta G = 0.00\ eV} NNH^* \xrightarrow{\mathbf{\Delta G = 0.87\ eV}} NHNH^* \xrightarrow{\Delta G = -0.95\ eV} NHNH_2^* \xrightarrow{\Delta G = -0.15\ eV} NH_2NH_2^* \xrightarrow{\Delta G = -1.81\ eV} NH_2NH$ $\xrightarrow{\mathbf{\Delta G = 0.81\ eV}} 2NH_3(g)$
$Mo_2TiC_2O_2$-Re_{SA}[40]	**Distal**	$\mathbf{N_2(g) \xrightarrow{\Delta G = 0.02\ eV} N_2^* \xrightarrow{\Delta G = 0.05\ eV} NNH^* \xrightarrow{\Delta G = -1.09\ eV} NNH_2^* \xrightarrow{\Delta G = 0.03\ eV} NNH_3^* \xrightarrow{\Delta G = -0.17\ eV} N^* \xrightarrow{\Delta G = -1.23\ eV} NH^* \xrightarrow{\Delta G = 0.48\ eV}}$ **(g)**
	Alternative	$N_2(g) \xrightarrow{\Delta G = 0.02\ eV} N_2^* \xrightarrow{\Delta G = 0.05\ eV} NNH^* \xrightarrow{\Delta G = -0.98\ eV} NHNH^* \xrightarrow{\mathbf{\Delta G = 0.88\ eV}} NHNH_2^* \xrightarrow{\Delta G = 0.14\ eV} NH_2NH_2^* \xrightarrow{\Delta G = -1.67\ eV} NH_2NH_3$ $\xrightarrow{\mathbf{\Delta G = 0.81\ eV}} 2NH_3(g)$
	Distal	$\mathbf{N_2(g) \xrightarrow{\Delta G = 0.11\ eV} N_2^* \xrightarrow{\Delta G = 0.26\ eV} NNH^* \xrightarrow{\Delta G = -1.15\ eV} NNH_2^* \xrightarrow{\Delta G = -0.28\ eV} NNH_3^* \xrightarrow{\Delta G = -0.32\ eV} N^* \xrightarrow{\Delta G = -1.14\ eV} NH^* \xrightarrow{\Delta G = 0.32\ eV}}$ $\mathbf{_3(g)}$

$Mo_2TiC_2O_2$-Os_{SA}[40]	Alternative		$N_2(g) \xrightarrow{\Delta G = 0.11eV} N_2^* \xrightarrow{\Delta G = 0.26\ eV} NNH^* \xrightarrow{\mathbf{\Delta G = 0.59\ eV}} NHNH^* \xrightarrow{\Delta G = -0.80\ eV} NHNH_2^* \xrightarrow{\Delta G = 0.03\ eV} NH_2NH_2^* \xrightarrow{\Delta G = -1.38\ eV} NH_2NH_3^* \xrightarrow{\mathbf{\Delta G = 0.72\ eV}} 2NH_3(g)$
Mo@Ti_2CO_2[41]	Distal		$N_2^* \xrightarrow{\mathbf{\Delta G = 0.79\ eV}} NNH^* \xrightarrow{\Delta G = -0.27\ eV} NNH_2^* \xrightarrow{\Delta G = -0.48\ eV} NNH_3^* \xrightarrow{\Delta G = -0.77\ eV} NH^* \xrightarrow{\Delta G = -0.23\ eV} NH_2^* \xrightarrow{\Delta G = -0.51eV} NH_3^* \xrightarrow{\mathbf{\Delta G = 0.33\ eV}}$
Ru@Ti_2CO_2[41]	Distal		$N_2^* \xrightarrow{\mathbf{\Delta G = 0.70\ eV}} NNH^* \xrightarrow{\Delta G = -0.46\ eV} NNH_2^* \xrightarrow{\Delta G = -0.28\ eV} NNH_3^* \xrightarrow{\Delta G = 0.15\ eV} NH^* \xrightarrow{\Delta G = -0.76\ eV} NH_2^* \xrightarrow{\Delta G = -0.37\ eV} NH_3^* \xrightarrow{\mathbf{\Delta G = 0.58\ eV}}$
Ru@Mo_2CO_2[41]	Distal		$N_2^* \xrightarrow{\mathbf{\Delta G = 0.46\ eV}} NNH^* \xrightarrow{\Delta G = -0.26\ eV} NNH_2^* \xrightarrow{\Delta G = -0.25\ eV} NNH_3^* \xrightarrow{\Delta G = 0.16\ eV} NH^* \xrightarrow{\Delta G = -0.56\ eV} NH_2^* \xrightarrow{\Delta G = -0.35\ eV} NH_3^* \xrightarrow{\mathbf{\Delta G = 0.59\ eV}}$
Ti@Mo_2CO_2[41]	Distal		$N_2^* \xrightarrow{\mathbf{\Delta G = 0.64\ eV}} NNH^* \xrightarrow{\Delta G = -0.59\ eV} NNH_2^* \xrightarrow{\Delta G = -0.77\ eV} NNH_3^* \xrightarrow{\Delta G = -0.41\ eV} NH^* \xrightarrow{\Delta G = -0.76\ eV} NH_2^* \xrightarrow{\Delta G = 0.47\ eV} NH_3^* \xrightarrow{\mathbf{\Delta G = 0.58\ eV}}$
γ-Mo_2N surfaces[33]	Dissociative	(100/010)	$N_2(g) \xrightarrow{\Delta G = 0.02\ eV} N_2^* \xrightarrow{\mathbf{\Delta G = 1.52\ eV}} 2N^* \xrightarrow{\Delta G = -0.28\ eV} N^* + NH^* \xrightarrow{\Delta G = -0.28\ eV} 2NH^* \xrightarrow{\Delta G = -0.79\ eV} NH^* + NH_2^*$ $2NH_3^* \xrightarrow{\Delta G = 0.05\ eV} NH_3^* + NH_3(g) \xrightarrow{\Delta G = 0.05\ eV} 2NH_3(g)$
		(101)	$N_2(g) \xrightarrow{\Delta G = -0.88\ eV} N_2^* \xrightarrow{\Delta G = -1.74\ eV} 2N^* \xrightarrow{\Delta G = -0.53\ eV} N^* + NH^* \xrightarrow{\Delta G = -0.53\ eV} 2NH^* \xrightarrow{\Delta G = -0.43\ eV} NH^* + NH$ $2NH_3^* \xrightarrow{\Delta G = 0.70\ eV} NH_3^* + NH_3(g) \xrightarrow{\Delta G = 0.70\ eV} 2NH_3(g)$
		(111)	$N_2(g) \xrightarrow{\Delta G = -0.68\ eV} N_2^* \xrightarrow{\Delta G = -3.64\ eV} 2N^* \xrightarrow{\Delta G = 0.09\ eV} N^* + NH^* \xrightarrow{\Delta G = 0.09\ eV} 2NH^* \xrightarrow{\Delta G = 0.70\ eV} NH^* + NH_2^*$ $2NH_3^* \xrightarrow{\Delta G = 0.92\ eV} NH_3^* + NH_3(g) \xrightarrow{\mathbf{\Delta G = 0.92\ eV}} 2NH_3(g)$
		(111)-defects	$N_2(g) \xrightarrow{\Delta G = -0.82\ eV} N_2^* \xrightarrow{\Delta G = -4.01\ eV} 2N^* \xrightarrow{\Delta G = 0.02\ eV} N^* + NH^* \xrightarrow{\Delta G = 0.01\ eV} 2NH^* \xrightarrow{\Delta G = 0.74\ eV} NH^* + NH_2^*$ $2NH_3^* \xrightarrow{\Delta G = 0.50\ eV} NH_3^* + NH_3(g) \xrightarrow{\Delta G = 0.50\ eV} 2NH_3(g)$
	Associative	(100/010)	$N_2(g) \xrightarrow{\Delta G = 0.02\ eV} N_2^* \xrightarrow{\mathbf{\Delta G = 1.40\ eV}} NNH^* \xrightarrow{\Delta G = 0.17\ eV} NNH_2^* \xrightarrow{\Delta G = -1.23\ eV} NH_3^* + N^* \xrightarrow{\Delta G = -0.27\ eV} NH^* + NH$ $(g) \xrightarrow{\Delta G = 0.05\ eV} 2NH_3(g)$
		(101)	$N_2(g) \xrightarrow{\Delta G = -0.88\ eV} N_2^* \xrightarrow{\Delta G = 0.16\ eV} NNH^* \xrightarrow{\Delta G = 0.13\ eV} NNH_2^* \xrightarrow{\Delta G = -1.12\ eV} NH_3^* + N^* \xrightarrow{\Delta G = -0.53\ eV} NH^* + NH$ $(g) \xrightarrow{\Delta G = 0.70\ eV} 2NH_3(g)$
		(111)	$N_2(g) \xrightarrow{\Delta G = -0.68\ eV} N_2^* \xrightarrow{\Delta G = -0.06\ eV} NNH^* \xrightarrow{\Delta G = -0.14\ eV} NNH_2^* \xrightarrow{\Delta G = -1.68\ eV} NH_3^* + N^* \xrightarrow{\Delta G = 0.09\ eV} NH^* + NH$ $(g) \xrightarrow{\mathbf{\Delta G = 0.92\ eV}} 2NH_3(g)$
		(111)-defects	$N_2(g) \xrightarrow{\Delta G = -0.82\ eV} N_2^* \xrightarrow{\Delta G = 0.18\ eV} NNH^* \xrightarrow{\Delta G = 0.0.03\ eV} NNH_2^* \xrightarrow{\Delta G = -2.21\ eV} NH_3^* + N^* \xrightarrow{\Delta G = 0.02\ eV} NH^* + NH$ $(g) \xrightarrow{\Delta G = 0.50\ eV} 2NH_3(g)$

(b) Species		The binding energies (BE) of possible N_2RR species on TMC and TMN catalysts and catalyst supports.
MoC[6]	(111)	BE_{NH} = -6.02 eV, BE_{NH_2} = 3.89 eV, BE_{NH_3} = -1.50 eV, BE_{NNH} = -3.19 eV, BE_{NNH_2} = -4.83 eV, BE_{NHNH} = -5.05 eV, BE_{NHNH_2} = -3.80 eV, $BE_{NH_2NH_2}$ = -2.02 eV BE_H = -3.26 eV, BE_N = -4.88/ - 6.86 eV and BE_{N_2} = -0.89/ - 1.06 eV
	(100)	BE_H = -2.07 eV, BE_N = -4.39/ - 6.25 eV and BE_{N_2} = -0.23/ - 0.05 eV
	(110)	BE_H = -2.77 eV, BE_N = -4.39/ - 5.48 eV and BE_{N_2} = -0.80/ - 0.89 eV
	(111)*	BE_H = -3.30 eV, BE_N = -4.95/ - 6.54 eV and BE_{N_2} = -0.89 eV
	(311)	BE_H = -3.03 eV, BE_N = -4.88/ - 6.03 eV and BE_{N_2} = -0.77/ - 0.80 eV
$MoC_{0.5}$[6]	(111)	BE_{NH} = -6.01 eV, BE_{NH_2} = -3.71 eV, BE_{NH_3} = -1.39 eV, BE_{NNH} = -3.71 eV, BE_{NNH_2} = -5.24 eV, BE_{NHNH} = -5.18 eV, BE_{NHNH_2} = -3.65 eV, $BE_{NH_2NH_2}$ = -1.98 eV BE_H = -3.37 eV, BE_N = -7.73 eV and BE_{N_2} = -0.93/ - 1.24 eV
	(100/010)	BE_H = -2.96 eV, BE_N = -3.95/ - 5.72 eV and BE_{N_2} = -0.44/ - 0.01 eV
	(101)	BE_H = -3.00 eV, BE_N = -6.04 eV and BE_{N_2} = -0.73/ - 1.13 eV
	(111)*	BE_H = -3.31 eV, BE_N = -7.62 eV and BE_{N_2} = -0.74/ - 1.65 eV
	(311)	BE_H = -3.50 eV, BE_N = -7.53/ - 7.28 eV and BE_{N_2} = -0.91/ - 1.60 eV
γ-Mo_2N surfaces[33]	(100/010)	BE_{NH} = -3.86 eV, BE_{NH_2} = - 2.97 eV, BE_{NH_3} = -0.95 eV, BE_{NNH} = -1.65 eV, BE_{NNH_2} = -2.94 eV, BE_{NHNH_2} = -2.41 eV, BE_H = -2.53 eV, BE_N = -4.88 eV and BE_{N_2} = -0.65 eV
	(101)	BE_{NH} = -6.19 eV, BE_{NH_2} = -4.93 eV, BE_{NH_3} = -1.68 eV, BE_{NNH} = -3.79 eV, BE_{NNH_2} = -5.12 eV, BE_{NHNH_2} = -4.56 eV, BE_H = -3.80 eV, BE_N = -6.96 eV and BE_{N_2} = -0.80/ - 1.54 eV
	(111)	BE_{NH} = -6.42 eV, BE_{NH_2} = -4.03 eV, BE_{NH_3} = -1.82 eV, BE_{NNH} = -3.81 eV, BE_{NNH_2} = -5.41 eV, BE_{NHNH_2} = -4.17 eV,

	(111)-defects	BE_H = -3.48 eV, BE_N = -7.84 eV and BE_{N_2} = -0.92/ - 1.34 eV BE_{NH} = -6.75 eV, BE_{NH_2} = -4.32 eV, BE_{NH_3} = -1.40 eV, BE_{NNH} = -3.71 eV, BE_{NNH_2} = -5.14 eV, BE_{NHNH_2} = -5.64 eV, BE_H = -3.34 eV, BE_N = -7.13/ - 8.07 eV and BE_{N_2} = -1.01/ - 1.48 eV
VNO(111)-N_{vac}[36]	BE_N = -5.79 eV, BE_{N_2} = -0.21 eV, BE_{HN_2} = -2.12 eV, BE_{NH_3} = -1.14 eV, BE_{NH} = -5.45 eV, BE_{NH_2} = -3.68 eV, and $BE_{N_2H_2}$ = -4.24 eV	
VNO(111)-O_{vac}[36]	BE_N = -7.31 eV, BE_{N_2} = -0.80 eV, BE_{HN_2} = -3.82 eV, BE_{NH_3} = -1.34 eV, BE_{NH} = -6.48 eV, BE_{NH_2} = -4.26 eV, and $BE_{N_2H_2}$ = -5.53 eV	

(c) Gibbs free energy change of the potential-determining step (ΔG_{PDS}, eV) in the mechanism of forming the first ammonia molecule via the Mvk mechanism

Species	Reaction mechanism	Rocksalt (100)	Rocksalt (111)	Zinc blende (100)	Zinc blende (110)
ZrN[34]	Mvk mechanism	ΔG_{PDS} =0.76	ΔG_{PDS} =1.42	-	ΔG_{PDS} =1.02
NbN[34]		ΔG_{PDS} =0.65	ΔG_{PDS} =1.12	-	ΔG_{PDS} =0.59
CrN[34]		ΔG_{PDS} =0.46	ΔG_{PDS} =0.58	ΔG_{PDS} =1.11	ΔG_{PDS} =0.54
VN[34]		ΔG_{PDS} =0.51	ΔG_{PDS} =0.85	ΔG_{PDS} =0.97	ΔG_{PDS} =1.06

(d)

Species	Reaction mechanism	Zinc blende (110)[35]			
		Single vacancy		Dimer vacancy	
		ΔG_{PDS}	ΔG_{RDS}	ΔG_{PDS}	ΔG_{RDS}
RuN	D-Mvk mechanism	-	1.89	0.23	-
CoN		0.27	1.31	0.27	-
NiN		0.10	2.98	0.10	3.76
NbN		0.59	-	0.68	-
CrN		0.54	-	0.54	0.88
RhN		-	4.57	-	1.41
ZrN		1.23	-	1.23	-
OsN		-	1.26	0.52	0.65
WN		0.55	-	0.55	-
FeN		0.75	-	0.75	-
IrN		-	3.17	-	0.58
PtN		-	4.26	3.11	-
PdN		-	4.21	-	4.27
VN		-	-	-	1.24

(e) Gibbs free energy change of the potential-determining step (ΔG_{PDS}, eV) for formation the second ammonia molecule via an associative (Assoc.) or dissociative (Dissoc.) mechanism, and barrier of N_2 dissociation (E_a) on TMN catalysts

Species	Rocksalt (100)			Rocksalt (111)			Zinc blende (100)			Zinc blende (110)		
	Assoc.	Dissoc.		Assoc.	Dissoc.		Assoc.	Dissoc.		Assoc.	Dissoc.	
	ΔG_{PDS}	ΔG_{PDS}	E_a	ΔG_{PDS}	ΔG_{PDS}	E_a	ΔG_{PDS}	ΔG_{PDS}	E_a	ΔG_{PDS}	ΔG_{PDS}	E_a
ZrN[34]	0.76	0.76	0.11	1.42	1.56	0.18	-	-	-	1.02	1.02	0.46
NbN[34]	0.65	0.65	0.35	1.12	1.12	0.45	-	-	-	0.59	0.59	0.04
CrN[34]	0.85	0.76	0.58	0.77	0.71	1.27	1.24	1.11	2.09	0.76	0.54	0.30
VN[34]	0.51	0.51	0.30	0.85	0.85	0.55	0.97	1.22	1.57	1.06	1.24	0.21

due to unfavorable thermodynamics for the formation of NH_2^*, a key reaction intermediate of N_2RR. However, the N_2RR is predicted to occur via the MvK mechanism on these TMN surfaces. Following the A-MvK and D-MvK mechanisms (**Table 5 (c) and 5(e)**), the first NH_3 molecule is formed by the protonation of a surface N atom, forming a N vacancy. A N_2 molecule is then activated on the N vacancy, which undergoes a series of reduction and dissociation reactions to form the second NH_3. Among all TMNs, rocksalt (100) of VN and CrN have been predicted to show excellent NRR activity with relatively low overpotentials (-0.51 and -0.76 V, respectively) via the D-MvK mechanism. Furthermore, these two catalysts also endow the low number of proton-electron pairs ($6(H^+ + e^-)$, **Figure 6(d)**) that are required to form $2NH_3$ to complete the catalytic cycle, and might result in relatively high current efficiencies. Moreover, these two nitride catalysts were predicted to have excellent stability (**Figure 6(e) and 6(g)**) in a N_2RR-relevant electrochemical environment. As such, VN and CrN are TMN materials predicted to have excellent catalytic activity for N_2RR.

TMNs in the zinc blende (ZB) phase have also been explored for electrochemical N_2RR.[35] Detailed DFT calculations on the ZB(110) facets of 23 TMNs identified RuN and CrN as the best catalytic candidates. The calculated free energy change of the potential-determining step (ΔG_{PDS}) and rate-determining step (ΔG_{RDS}) for electrochemical N_2RR to NH_3 via both a single and a dimer N-vacancy with D-MvK mechanism on TMN catalyst are summarized in **Table 5(d).** The potential-determining step (PDS) for the ZB(110) facets of

RuN and CrN were the formation of NH_2^* and NH^*, respectively. The calculated ΔG_{PDS} and the number of proton-electron pairs required to produce $2NH_3$ on all TMNs are shown in **Figure 6(h)**. The calculated free energy of adsorption of O, OH, or H relative to dissociated $2N^*$ ($\Delta G_{(2N^*-X^*)}$, where X = O, OH or H, a negative value of $\Delta G_{(2N^*-X^*)}$ indicates that it is thermodynamically favorable to fill the vacancy with N, rather than O, OH, or H) on the surface vacancy of catalytically active nitrides are shown in **Figure 6(f)**, which inform the resistance to the poisoning of the surface vacancy. Comparison of the calculated activation free energy barrier (G_a) of catalyst replenishment by N_2 dissociation for refilling the N-vacancy and the migration of nitrogen atoms from the bulk toward the surface to fill the vacancy is shown in **Figure 6(i).** These calculations predict the stability of nitrogen vacancies and the possibility of catalyst regeneration. Generally, If the G_a value of vacancy migration is much larger than that of vacancy replenishment, the catalyst is likely able to regenerate and endure the catalytic cycle. Based on the calculated ΔG_{PDS}, the number of proton-electron pairs required for the formation of $2NH_3$, the poison tolerance of surface vacancies, and the regeneration of the active site during the electrochemical N_2RR process, it is apparant that RuN and CrN can serve as good candidates for electrochemical N_2RR.

Furthermore, DFT calculations were performed to understand the N_2RR mechanism on a surface N-vacancy (N-vac) and an O-vacancy (O-vac) of VNO (111).[36] The study showed that the N_2RR proceeds via the MvK mechanism combined with the distal channel of the associative mechanism (**Figure 6(a)**), and N-vac facilitated N_2RR is predicted to be more facile than O-vac facilitated N_2RR. This is primarily due to the over binding of some of the N_2RR intermediates (**Table 5(b)**) on the surface O-vac of VNO (111). For N-vac facilitated electrochemical NRR (**Figure 6(c)**), the PDS was predicted to be the reduction of N_2^* to N_2H^* (i.e. $N_2^* + 1/2H_2(g) \rightarrow N_2H^*$), with an endothermic energy change of 0.56 eV, consistent with the experimental observation that the first electron-transfer step was the PDS. For O-vac facilitated electrochemical N_2RR (**Figure 6(c)**), the PDS was $NH_2^* + 1/2H_2(g) \rightarrow NH_3^*$, with a thermodynamic energy change of 0.62 eV. The slightly smaller uphill energy change for the PDS on the N-vac compared to that on the O-vac surface indicates that the electrochemical N_2RR on the N-vac surface is more favourable. The stronger binding of N_2RR intermediates on the O-vac led to the deactivation of the catalytic sites as observed in the corresponding experiments.[37] This study demonstrated that N vacancies on VNO surfaces are the active sites for the electrochemical transformation of N_2 to NH_3.

The electrocatalytic N_2RR activity and mechnism on MXene based materials have also been investigated using DFT calculations.[38,39] In a recent study, Johnson et al.[38] explored the N_2RR activity on a set of bare and functionalized MXenes via a DFT high-throughput computational investigation. Their study revealed that the PDS was NH_3^* formation from NH_2^* on bare MXenes, whereas, the PDS was the formation of N_2H^* on functionalized MXenes via an associative mechanism. The calculated onset potentials on M_2XT_x MXenes (M = Ti, V, Zr, Nb, Mo, Ta, W; X = C, N; T_x = bare, H, O, N) were shown in **Figure 7(a)**, which suggested that the overpotential on the bare MXene increased with the period number of the M constituent of the MXene. It was also found that the pristine Mo_2C had the lowest overpotential (0.56 V) and Ti_2CO_2 showed the largest overpotential among the studied pristine and functionalized MXenes. On the other hand, it was also found that the type of functional group played an important role in regulating the stability and performance of N_2RR on MXenes. For instance, pristine MXenes were not stable and were transformed into functionalized MXenes under the electrochemical N_2RR conditions based on Pourbaix diagrams and selectivity analysis (**Figures 7(b) and (c)**). Therefore, it was concluded that only the functionalized MXenes should have low theoretical overpotentials, remained stable, and possessed high selectivity toward NH_3 compared to the competing HER under the electrochemical conditions.

Wang et al.[39] also have systematically studied electrochemical N_2RR on a series of transition metal M_2C (M = Sc, Ti, V, Cr, Mn, Fe, Zr, Nb, Mo, Ta, and Hf) MXenes, and computed their U_L to identify promising electrochemical N_2RR catalysts. The DFT-calculated BE of N_2 adsorption on M_2C indicated that N_2 favorably adsorbed on the atop metal site in an end-on configuration and the two-fold hollow site with a side-on configuration. For the 3d TM M_2C (M = Sc, Ti, V, Cr, Mn and Fe), the BE of N_2 followed the order: $Sc_2C > Ti_2C > V_2C >$

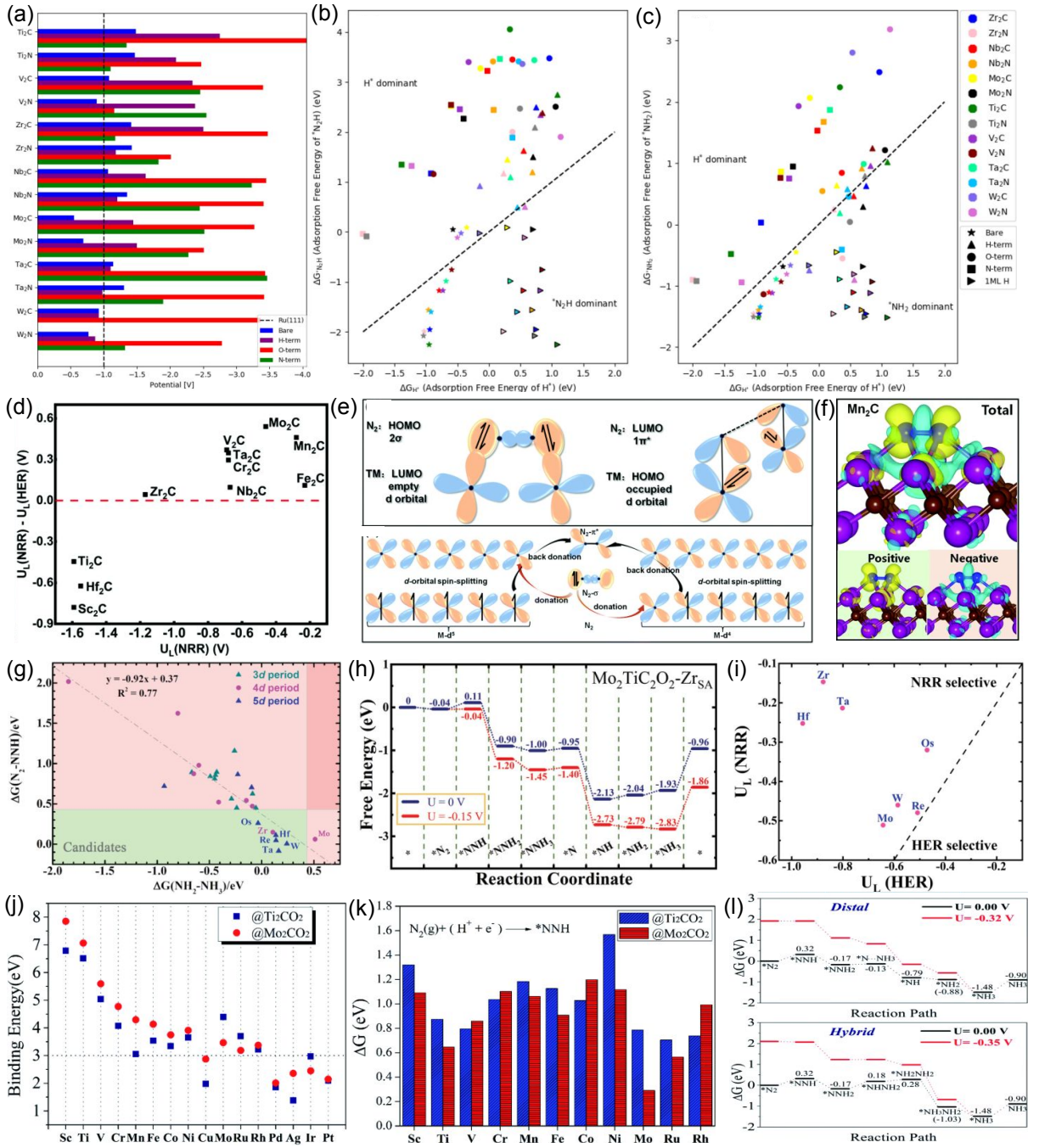

Figure 7. (a) The calculated onset potentials of M_2XT_x with different functional group, the comparison of adsorption free energies of (b) N_2H^* and (c) NH_2^* vs the adsorption free energy of H^*. Reproduced with permission from ref. 38 from American Chemical Society, Copyright 2020; (d) The calculated limiting potentials of N_2RR and HER, i.e., $U_L(N_2RR)$-$U_L(HER)$ vs $U_L(N_2RR)$, (e) the d-orbital spin-split rule to interpret the behaviour of electron acceptance and back donation between N_2 and surface metals during the electrochemical N_2RR process, and (f) the charge density difference Mn_2C with the side-on N_2 adsorption, where the isosurface value is set to be 0.003 e Å^{-3}. Reproduced with permission from ref. 39 from Royal Society of Chemistry, Copyright 2020; (g) Screening results of $Mo_2TiC_2O_2$-TM_{SA} for N_2RR based on $\Delta G(N_2\text{-}NNH)$ and $\Delta G(NH_2\text{-}NH_3)$, (h) the calculated free-energy profiles of N_2RR on $Mo_2TiC_2O_2$-Zr_{SA} through the distal path, and (i) the calculated limiting potentials for HER ($U_L(HER)$) and NRR ($U_L(N_2RR)$) on the selected candidates. Reproduced with permission from ref. 40 from Wiley-Vch, Copyright 2019. (j) The calculated BE of single metal atom adsorptions on Ti_2CO_2 and Mo_2CO_2 MXenes, (k) the calculated reaction free energies for N_2^* to NNH^* on various TM@Ti_2CO_2 and TM@Mo_2CO_2, and (l) the calculated free energy profiles of N_2RR on Mo@Mo_2CO_2 through distal and hybrid mechanisms. Reproduced with permission from ref. 41 from the Royal Society of Chemistry, Copyright 2019.

Cr_2C > Mn_2C > Fe_2C, while the 4d-5d M_2C BE followed the order: Zr_2C > Nb_2C > Mo_2C and Hf_2C > Ta_2C. According to the calculated ΔG of each elementary step of electrochemical N_2RR (**Table 5(a)**), it was found that Mo_2C showed the lowest U_L of -0.46 V and the N_2RR followed the associative pathway. The corresponding PDS was predicted to be the reaction of $NH_2^*NH_3^*$ + (H^+ + e^-) → $NH_3^*NH_3^*$. Mn_2C and Fe_2C were predicted to possess significantly small U_L values -0.28 and -0.23 V, respectively (**Table 5(a)**). The DFT calculated $U_L(N_2RR)$-U_L(HER) on M_2C MXenes (**Figure 7(d)**) suggested that the N_2RR should be more selective than the competing HER on most 3d-5d M_2C MXenes, except for M = Sc, Ti, and Hf. It was found that the N_2RR activity could be explained with the d-orbital electron configuration of M in MXene (**Figure 7(e)**). For example, Mn_2C and Fe_2C possessed excellent N_2RR performance because of their $3d^5$ or $3d^6$ electron arrangements. Such 3d electron configurations allow the adsorbed N_2 to donate 1 σ electrons to the higher-energy spin-down empty 3d orbitals of Mn and Fe (**Figure 7(f)**) enhancing the adsorption of N_2 molecule and consequently the overall N_2RR activity.

In addition, DFT calculations also were employed to investigate the N_2RR performance on SACs anchored on MXenes.[40,41] In one study, 3d-5d TM single atoms were embedded in the defective $MoTiC_2O_2$ MXene to create a library of SACs of the type $Mo_2TiC_2O_2$-TM_{SA}.[40] The free energy barriers of the first (N_2^* to NNH^*, $\Delta G(N_2$-$NNH)$, and the last (NH_2^* to NH_3^*, $\Delta G(NH_2$-$NH_3)$) hydrogenation steps in N_2RR were used as descriptors to screen potential SACs for efficient N_2RR (**Figure 7(g)**). Such screening criterion (**Figure 7(g)**) showed that Zr, Mo, Hf, Ta, W, Re, and Os single atoms supported on defective $Mo_2TiC_2O_2$ should have an ability to promote the overall N_2RR process. The free energy diagrams calculated for the complete reduction of N_2 to NH_3 illustrated that the distal mechanism is thermodynamically favorable over the alternating mechanism, and thus the N_2RR on $Mo_2TiC_2O_2$-TM_{SA} was predicated to follow the distal channel of the associative mechanism (**Table 5(a)**). Among the studied catalysts, $Mo_2TiC_2O_2$-Zr_{SA} showed the lowest ΔG_{PDS} (0.15 eV), and the corresponding potential determining step was predicted to be N_2^*→NNH^* (U_L=-0.15 V, **Figure 7(h)**). Interestingly, the UL values of N_2RR were lower than HER for the selected catalysts (**Figure 7(i)**). **Figure 7(i)** suggesting that the N_2RR should be favored over the HER on the selected candidates.

To explore how single atomic catalysts (SACs) regulate the selectivity and activity of electrochemical N_2RR on MXene-based SACs, the author investigated serious of single TM atom anchored on the Ti_2CO_2 and Mo_2CO_2 MXene monolayers as efficient N_2RR electrocatalysts via DFT calculations.[41] The author study the stability of single TM atom anchored on MXene in first, the calculated BE of single TM atom on MXene were shown in **Figure 7(j)**, implying that the BE decrease with increasing d electrons in 3d metal elements. The author only considered the SACs of BE upon the horizontal dash line in **Figure 7(j),** because the weak binding strength may cause TM atoms to detach from the substrate, resulting in the electrocatalysts having poor performance and stability. The calculated BE of N_2 on $TM@Ti_2CO_2$ and $TM@Mo_2CO_2$ surfaces indicated that the N_2 molecule with the end-on configuration was preferential comparing to those with the side-on configuration. The calculated free energies of N_2^* to NNH^* step on various $TM@Ti_2CO_2$ and $TM@Mo_2CO_2$ suggested that only Ru and Mo anchored MXene catalysts have better catalytic performance for the common potential determining step (PDS) (**Figure 7(k)**), based on the criteria that the PDS of most SACs is the step of NNH^* and NH_3^* formation, and the free energy of corresponding PDS not surpass 0.8 eV (ΔG_{PDS}). The calculated complete reaction paths of electrochemical N_2RR on Ru and Mo anchored Ti_2CO_2 and Mo_2CO_2 MXene indeed confirmed that the mentioned catalysts possessed high N_2RR activity toward the production of NH_3 via the distal mechanism (**Table 5(a)**). Especially, the U_L for $Ru@Mo_2CO_2$ was -0.46 V, which was less negative than the substrate of Ti_2CO_2 because the substrate of Mo_2CO_2 have the high conductivity. In addition, comparing the ΔG of each N_2 and H as well as first N_2 protonation and H adsorption, the author studied the activity and selectivity of the electrochemical N_2RR on $Mo@Mo_2CO_2$. The calculated results shown that the electrochemical N_2RR via the distal or hybrid mechanism with the U_L is -0.32 V or -0.35 V, corresponding theoretical overpotential is 0.16 or 0.19 V, implying that $Mo@Mo_2CO_2$ exhibit rapid electrochemical N_2RR performance (**Figure 7(l)**).

3.5 Carbon Dioxide Reduction Reaction (CO_2RR)

Large-scale utilization of fossil fuels has tremendously contributed to the economic development and the improvement of the living standard of people around the globe. However, the large-scale use of fossil fuels has also led to an increase in anthropogenic CO_2 emissions into the atmosphere. Such CO_2 emission has been linked to adverse environmental effects such as global warming, ocean acidification, climatic variation, etc.[42,45,166] The development of CO_2 utilization technologies, such as the electrochemical CO_2 reduction reaction (CO_2RR) powered by electricity generated from renewable energy sources[46], are promising and sustainable methods for the reduction of CO_2 emissions. The electrochemical CO_2RR at ambient conditions not only mitigates net CO_2 emission but also produces energy dense fuels and value-added feedstocks.[16] The mechanism of CO_2RR is complex because of the possibility of the formation of multiple (a mixture of C_1 and C_2) products. The final product of CO_2RR depends on the number of H^+/e^- pairs transferred to CO_2. [43,45] For instance, it has been shown that CO_2 can be electrochemically converted to various gaseous and liquid chemicals including carbon monoxide and hydrogen (CO and H_2, syngas),[16,42,43] hydrocarbon fuels (CH_4 and C_2H_4),[44-46,167] and hydrocarbon oxide fuels (CH_3OH and C_2H_5OH)[166-168] under ambient and aqueous condition. Fundamental understanding of the CO_2RR mechanism is necessary for the design of catalysts for the selective transformation of CO_2 to desired products.

Recent theoretical and experimental studies have identified Au, Ag, Cu, and Pd[42,166] metal oxides, and metal-organic complexes as the best performing CO_2RR catalysts.[166] Among the various metals explored, Ag and Au exhibit high selectivity for CO, while Cu is the only metal that shows selectivity for hydrocarbons.[166] Cu_2O and RuO_2 were found to promote the CH_3OH production.[166,167] Fine-tuning the product selectivity of CO_2RR is challenging and often requires a nonlinear tuning of the binding energy of reaction intermediates.[46] TMCs and TMNs serve as a platform materials in this regard. Recent studies have demonstrated that TMC- and

TMN-based catalysts not only reduce precious metal (e.g. Au, Ag, Pd) loading, but also show enhanced activity/selectivity for CO_2RR to C_1 (CO, CH_4, HCOOH, and CH_3OH)[16,42-46,166,168] and C_2 (C_2H_4 and C_2H_5OH)[167] products (**Figure 8**), due in part to the high electrical conductivity and stability under reaction conditions.

The binding energy and change in free energy (ΔG) involved in electrochemical CO_2RR can be calculated using equations (1) to (10) as described in the introduction. The limiting potential (U_L) is a theoretical onset potential calculated from the maximum free energy change (ΔG_{MAX}) along the lowest energy pathway by using a relation U_L (vs RHE) = $-\Delta G_{MAX}/e$.[47,48,52] Thus, TMC and TMN surfaces with less negative U_L relative to parent transition metals can be identified as candidates for CO_2RR catalysis.[46,51,52,168]

Extensive DFT studies have been performed for CO_2RR over TMC and TMN catalysts,[16,42-52,166-170] the selected results of which are summarized in Table 6. DFT calculations, combined with experimental measurements, were performed to explore the CO_2RR activity of PdH layers supported on TMC substrates.[42] PdH overlayers were considered in theoretical calculations because in situ X-ray absorption spectroscopy (XANES and EXAFS) and in situ X-ray diffraction (XRD) indicated the transformation of Pd to PdH phase during the CO_2RR. The DFT calculated free energy diagrams (**Figure 9(a)**) predicted an enhanced CO_2RR over PdH supported on TMCs. In agreement with the experimental findings, the performance of CO_2RR was predicted to follow the sequence: PdH/TaC(111) > PdH/NbC(111) > PdH(111) (**Table 6(a)** and **Figure 9(a)**). The enhanced CO_2RR was mainly attributed to the stronger binding of $HOCO^*$ (**Table 6(a)**), a key intermediate of CO_2RR. The results from this study show that Pd supported on TaC exhibits higher activity than the commercial Pd/C catalyst, resulting in a significantly reduced Pd loading compared with commercial Pd/C.

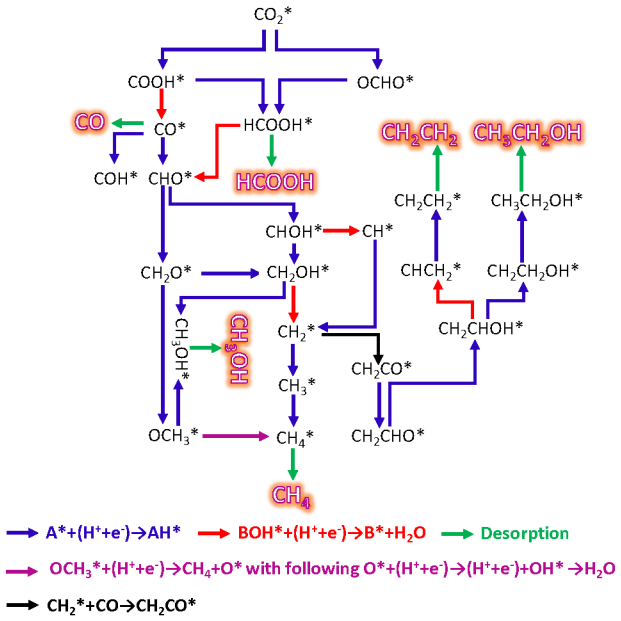

Figure 8. Proposed electrochemical CO_2RR pathways for C_1 (CO, HCOOH, CH_3OH, and CH_4) and C_2 (CH_2CH_2 and CH_3CHOH) products.[166-168] A and B represent different species.

Catalytic activity and product selectivity trends for electrochemical CO_2RR on transition metal monolayer coated tungsten carbides (M/WC core-shell metal/metal-carbide particles, M = Mn, Fe, Co, Ni, Cu, Zn, Ru, Rh, Pd, Ag, Ir, Pt, and Au) have been studied by means of DFT calculations.[43] The trend in activity and product selectivity was investigated by calculating the free energy change along several pathways leading to various C_1 products (**Figures 9(b) and (c)**). The results showed that when the interaction between the supported metals and the reaction intermediates was weak, the main product of CO_2RR was CO. WC supported catalysts, such as Zn/WC, Ag/WC, and Au/WC, had similar limiting potentials compared to those of pristine metal surfaces. Consequently, these core-shell M/WC architectures may help reduce the loading of precious metals (e.g. Au, Ag) for the design of CO_2RR catalysts. The DFT predicted limiting potentials for CO_2RR to CO were relatively low (U_L~-0.2 V) on Cu/WC and Pd/WC. Interestingly, it was found that generated CO could be further reduced to CH_4 and CH_3OH on Cu/WC and Pd/WC core-shell catalysts, respectively, at the limiting potential U_L~-0.88 V (**Figure 9(b)**). The OBE on the catalyst surface was found to significantly influence the formation of C_1 products. CH_4 was predicted to be the main product of CO_2RR on catalyst surfaces that bind O strongly, while surfaces that bind O weakly were predicted to promote CH_3OH formation. Furthermore, it was observed that the binding energy of CO^*, a key CO_2RR intermediate, was linearly correlated with the binding energy of other reaction intermediates such as $COOH^*$, CHO^*, and COH^*, which bound to the surface via the C atom. On the other hand, the OBE was linearly correlated with the binding energy of the OH^* and CH_3O^* reaction intermediates. Thus, the binding energies of CO^* and O^* were proposed as descriptors of catalytic activity and selectivity of CO_2RR. The DFT calculations performed on M/WC showed that the binding energy of CO^* and O^* correlate linearly with the d-band center of the supported metal (M) on the WC substrate, suggesting that the d-band center could serve as a single-parameter descriptor to predict the product selectivity of CO_2RR on TMC-supported metal catalysts (**Figure 9(c)**).

The eight electron-transfer CO_2RR to CH_4 on WC and transition-metal-decorated WC surfaces have been explored via DFT calculations.[44] It was found that the adsorption of reaction intermediates during electrochemical CO_2RR to CH_4 on these complex surfaces is governed by binding site-specific directional electronic effects that could not be accounted for in the conventional d-band model. To address this issue, an extended component-resolved d-band model was developed, where the intermediate binding at top sites is primarily affected by the d_{z^2} component of the d-band, whereas the symmetrically equivalent d_{xz} and d_{yz} components govern binding at hollow sites, as well as at bridge sites (between two metal atoms). Such a model was able to explain both site preference and binding-energy trends on metal-decorated WC surfaces. Various WC surfaces with Fe coverages ranging from 1/9 to 1/2 ML were considered in DFT calculations to examine the spatial extent of perturbations to the WC electronic structure, and the calculated binding energy variations (**Figure 9(i)**) validated the extended d-band model. The author also took 1/4- and 1/2-ML Fe/WC

Table 6. Summary of DFT calculated energetics of CO_2RR. (a) the binding energies (BE, eV) of key intermediates (i.e., O, OH, HOCO, COOH, CO and CHO) during the electrochemical CO_2RR on TMC and TMN catalysts and catalyst supports; (b) free energy difference (ΔG, eV) for each elementary step along the electrochemical CO_2RR via various pathways to produce different products (**Figure 8**). The optimal reaction pathways and the potential-determining step (PDS) are in bold font.

(a) Species	The calculated binding energy of electrochemical CO_2RR intermediates (BE, eV) via different pathways to produce different products (**Figure 8**)	
Pd/TMC[42]	PdH/NbC(111)	BE_{HOCO} = -1.62 eV and BE_{CO} = -0.93 eV
	PdH/TaC(111)	BE_{HOCO} = -1.67 eV and BE_{CO} = -0.96 eV
	PdH(111)	BE_{HOCO} = -1.56 eV and BE_{CO} = -0.79 eV
Pd/TMN[16]	PdH/NbN(111)	BE_{HOCO} = -1.67 eV and BE_{CO} = -0.90 eV
	PdH/VN(111)	BE_{HOCO} = -1.38 eV and BE_{CO} = -0.41 eV
	Pd/VN(111)	BE_{HOCO} = -2.13 eV and BE_{CO} = -2.06 eV
	PdH(111)	BE_{HOCO} = -1.57 eV and BE_{CO} = -0.80 eV
M@d-TiC[46]	Ag	BE_{COOH} = -0.07 eV, BE_{CHO} = 0.03 eV, and BE_{CO} = -0.70 eV
	Au	BE_{COOH} = -0.08 eV, BE_{CHO} = 0.03 eV, and BE_{CO} = -0.70 eV
	Co	BE_{COOH} = -0.16 eV, BE_{CHO} = -0.24 eV, and BE_{CO} = -1.11 eV
	Cu	BE_{COOH} = -0.18 eV, BE_{CHO} = 0.05 eV, and BE_{CO} = -0.70 eV
	Fe	BE_{COOH} = -0.05 eV, BE_{CHO} = -0.01 eV, and BE_{CO} = -0.92 eV
	Ir	BE_{COOH} = 0.11 eV, BE_{CHO} = -0.02 eV, and BE_{CO} = -1.18 eV
	Ni	BE_{COOH} = 0.04 eV, BE_{CHO} = -0.02 eV, and BE_{CO} = -0.72 eV
	Os	BE_{COOH} = 0.30 eV, BE_{CHO} = 0.20 eV, and BE_{CO} = -1.02 eV
	Pd	BE_{COOH} = 0.11 eV, BE_{CHO} = 0.08 eV, and BE_{CO} = -0.71 eV
	Pt	BE_{COOH} = 0.10 eV, BE_{CHO} = -0.01 eV, and BE_{CO} = -0.81 eV
	Rh	BE_{COOH} = 0.01 eV, BE_{CHO} = -0.04 eV, and BE_{CO} = -0.98 eV
	Ru	BE_{COOH} = 0.18 eV, BE_{CHO} = 0.14 eV, and BE_{CO} = -1.00 eV
	TiC	BE_{COOH} = -0.15 eV, BE_{CHO} = -0.12 eV, and BE_{CO} = -1.78 eV

		O^*	OH^*	CO^*	COH^*	CHO^*
Fe/WC[44]	WC(3 × 2)	BE=-1.87 eV	BE=-1.26 eV	BE=-1.48 eV	BE=-1.45 eV	BE=-1.84 eV
	WC(2 × 2)	BE=-1.84 eV	BE=-1.21 eV	BE=-1.50 eV	BE=-1.40 eV	BE=-1.79 eV
	1/2 ML Fe/WC	BE=-0.55 eV	BE=-0.19 eV	BE=-1.32 eV	BE=-1.51 eV	BE=-1.47 eV
	1/4 ML Fe/WC	BE=-1.20 eV	BE=-0.46 eV	BE=-1.21 eV	BE=-1.26 eV	BE=-1.41 eV
	1/6 ML Fe/WC	BE=-1.65 eV	BE=-0.93 eV	BE=-1.34 eV	-	-
	1/9 ML Fe/WC	BE=-1.77 eV	BE=-1.04 eV	BE=-1.42 eV	-	-
$Mo_2C(100)$[52]	Mo-terminated	BE=-2.09 eV	BE=-1.57 eV	BE=-2.16 eV		BE=-2.24 eV
	C-terminated	BE=-0.76 eV	BE=-0.81 eV	BE=-1.70 eV		BE=-1.85 eV
$Mo_2C(101)$[52]		BE=-1.83 eV	BE=-1.62 eV	BE=-2.05 eV		BE=-2.30 eV
$Mo_2C(110)$[52]		BE=-1.72 eV	BE=-1.44 eV	BE=-2.29 eV		BE=-2.25 eV
MoC(100)[52]		BE=-0.62 eV	BE=-0.56 eV	BE=-1.59 eV		BE=-1.82 eV
MoC(110)[52]		BE=-1.51 eV	BE=-0.88 eV	BE=-2.28 eV		BE=-3.04 eV
MoC(111)[52]	C-terminated	BE=-1.86 eV	BE=-1.43 eV	BE=-2.78 eV		BE=-2.72 eV
	Mo-terminated	BE=-1.44 eV	BE=-1.43 eV	BE=-1.97 eV		BE=-2.11 eV

(b) Species	Free energy difference (ΔG, eV) for each elementary step along the electrochemical CO_2RR via different pathway to produce different products (**Figure 8**)
M_3C_2[45]	$Mo_3C_2(OH)_2$: $* \xrightarrow{+CO_2(g),\ BE = 0.35\ eV} CO_2^* \xrightarrow{+H,\ \Delta G = -0.92\ eV} COOH^* \xrightarrow{+H,\ \Delta G = -0.37\ eV} HCOOH^* \xrightarrow{+H,\ \Delta G = -0.12\ eV} CH_2COOH^* \xrightarrow{+H - H_2O,\ \Delta G = -0.08\ eV} CH_2O^* \xrightarrow{+H,\ \Delta G = -1.57\ eV} CH_3O^* \xrightarrow{+H - CH_4,\ \Delta G = -0.03\ eV} O^* \xrightarrow{+H,\ \Delta G = -0.83\ eV} OH^* \xrightarrow{+H,\ \mathbf{\Delta G = 1.}}$
	$Mo_3C_2O_2$: $* \xrightarrow{+CO_2(g),\ BE = 0.23\ eV} CO_2^* \xrightarrow{+H,\ \Delta G = 0.49\ eV} COOH^* \xrightarrow{+H,\ \Delta G = -0.09\ eV} HCOOH^* \xrightarrow{+H - H_2O,\ \Delta G = -0.20\ eV} CHO^* \xrightarrow{+H,\ \mathbf{\Delta G = 0.54\ eV}} CH_2O^* \xrightarrow{+H,\ \Delta G = -0.90\ eV} CH_2OH^* \xrightarrow{+H,\ \Delta G = 0.35\ eV} CH_3OH^* \xrightarrow{+H - H_2O,\ \Delta G = -0.96\ eV} CH_3^* \xrightarrow{+H,\ \Delta G =} CH_4^*$
Mo_2C[50]	Bare: $* \xrightarrow{+CO_2(g),\ \Delta G = -0.82\ eV} CO_2^* \xrightarrow{\Delta G = 0.68\ eV} COOH^* \xrightarrow{\Delta G = -0.33\ eV} CO^* \xrightarrow{\Delta G = 1.09\ eV} CO$
	O-terminated with O vacancy: $* \xrightarrow{+CO_2(g),\ \Delta G = 0.05\ eV} CO_2^* \xrightarrow{\Delta G = 0.78\ eV} COOH^* \xrightarrow{\Delta G = -0.09\ eV} CO^* \xrightarrow{\Delta G = 0.23\ eV} CO$
	DFT+U: $* \xrightarrow{+CO_2(g),\ \Delta G = -0.04\ eV} CO_2^* \xrightarrow{\Delta G = 0.90\ eV} COOH^* \xrightarrow{\Delta G = -0.45\ eV} CO^* \xrightarrow{\Delta G = 0.20eV} CO$
Ti_3C_2[50]	Bare: $* \xrightarrow{+CO_2(g),\ \Delta G = -2.85\ eV} CO_2^* \xrightarrow{\Delta G = 2.39\ eV} COOH^* \xrightarrow{\Delta G = -0.06\ eV} CO^* \xrightarrow{\Delta G = 0.90\ eV} CO$
	O-terminated with O vacancy: $* \xrightarrow{+CO_2(g),\ \Delta G = -0.23\ eV} CO_2^* \xrightarrow{\Delta G = 1.04\ eV} COOH^* \xrightarrow{\Delta G = -0.09\ eV} CO^* \xrightarrow{\Delta G = -0.10\ eV} CO$
	DFT+U: $* \xrightarrow{+CO_2(g),\ \Delta G = -0.22\ eV} CO_2^* \xrightarrow{\Delta G = 1.09\ eV} COOH^* \xrightarrow{\Delta G = -0.01\ eV} CO^* \xrightarrow{\Delta G = -0.24\ eV} CO$

surfaces as examples to further study CO_2RR to CH_4, finding that the energy of occupied $d_{xz/yz}$ and d_z^2 states downshifted in comparison to pristine WC (**Figure 9(i)**), which resulted in lower CO and O binding energies relative to bare WC (**Table 6(a)**). The calculated free-energy diagram for CO_2RR to CH_4 on Fe-modified W surfaces via the carbophilic and oxophilic reaction pathway is shown in **Figure 9(j).** It was revealed that the oxygen pathway became increasingly uphill as Fe coverage increased, whereas the limiting potential of the carbophilic pathway reduced to U_L = -0.22 V, which was smaller than that of bare WC (U_L = -0.35 V). Thus, it was purposed that tuning the oxophilicity and carbophilicity of the surface can tailor catalysts for desirable product selectivity and optimized activation potential for the electrochemical CO_2RR to CH_4.

Li et al.[52] employed DFT calculations to study the relationship between the active-site and product selectivity of electrochemical CO_2RR on Mo_2C and MoC surfaces. They calculated BE of the main reaction intermediates (CO^*, CHO^*, O^*, and OH^*) on a set of eight low index facets and surface terminations of orthorhombic Mo_2C and cubic MoC with different Mo/C ratios during the CO_2RR process (**Table 6(a)**). It was found that the CO^* intermediate kept its up-right adsorption configuration on TM surfaces, whereas, the intermediate CHO^* preferred a side-on configuration. Furthermore, the author also calculated the U_L as a function of $\Delta G_{ad}(OH^*)$ to evaluate the effect of different active sites on product selectivity (**Figure 10(a)**). It was revealed that the product selectivity of electrochemical CO_2RR was governed by the metal/carbon ratio of the active site. For instance, the CHE-based thermodynamic analysis suggested that CH_4 was favored on the Mo-rich active-sites while CH_3OH was produced on the C-rich active-sites. In addition, the equilibrium nanoparticle shape at any given potential (**Figure 10(b)**) was constructed via the Wulff construction[171,172]. **Figure 10(b)** revealing that the equilibrium particle shapes of MoC and MoC_2 at open circuit (0 V vs RHE) and working potential (-0.5 V) predominantly consisted of the non-polarized (100) facet.

Furthermore, the electrocatalytic CO_2RR activity and mechanism on MXene materials have also been investigated using DFT calculations.[45,47-50] For instance, among all group IV, V, and VI TM MXenes,[45] the DFT results showed that the Cr_3C_2 and Mo_3C_2 MXenes should be the most promising candidates for converting CO_2 into CH_4. Cr_3C_2 and Mo_3C_2 have a strong binding affinity for O, making OH^* reduction to H_2O^* the rate-determining step of CO_2RR, with the ΔG values calculated being 1.05 and 1.31 eV, respectively (**Figures 9(d) and (e)**). The binding preference of the Cr_3C_2 and Mo_3C_2 surfaces for O and OH suggests that these surfaces may be covered by O/OH during CO_2RR. Additional DFT calculations were performed to study CO_2RR on $Mo_3C_2O_2$ and $Mo_3C_2(OH)_2$ surfaces as models to represent the O- and OH- covered Mo_3C_2 MXenes, respectively. The results (**Table 6(b)**) showed that the limiting step was the release of OH^* species in the form of a relatively strongly chemisorbed H_2O^* molecule with a ΔG value of 1.17 eV on $Mo_3C_2(OH)_2$. In contrast, the limiting step on $Mo_3C_2O_2$ was determined to be the formation of CH_2O^* species, with a ΔG value of 0.54 eV. The study suggested that the termination of MXene surfaces with either O or OH can stabilize the MXene and promote CO_2RR.

Two-dimensional Ti- and Mo-based MXenes have been investigated as catalysts for CO_2RR using experimental techniques and DFT calculations.[47] In experiments, Ti_2CT_x and Mo_2CT_x MXenes (T_x = F and O) showed promising performance for electrocatalytic CO_2RR to formic acid (main product), with Faradaic efficiency of over 56% on Ti_2CT_x at -1.8 V versus standard hydrogen electrode (SHE) and partial current density of up to -2.5 mA cm^{-2} on Mo_2CT_x. DFT calculations were carried out to identify the role of the surface termination group on Ti- and Mo-based MXenes for electrocatalytic CO_2RR to formic acid. The DFT-calculated results demonstrated that the presence of an -F termination group tuned the binding strength of intermediates and the corresponding CO_2RR limiting potential favorably, compared with the O-terminated MXenes (**Figures 10(c) and (d)**). For example, on a fully O-terminated Ti_2CT_x surface, the PDS of electrocatalytic CO_2RR is $CO_2^* + H^+ + e^- \rightarrow COOH^*$ step with the corresponding U_L of -0.85 V. However, with increasing substitution of F for O-T_x group in Ti_2CT_x, the U_L become more negative at -0.89 V to -1.26 V for 33.3% and 66.7% -F substitution, respectively (**Figures 10(c)**). On a fully O-terminated Mo_2CT_x, the PDS step was $COOH^* + H^+ + e^- \rightarrow HCOOH^*$ with a U_L of -0.47 V. Interestingly, it was found that the presence of F-T_x group can change the PDS step from $COOH^* + H^+ + e^- \rightarrow HCOOH^*$ to $CO_2^* + H^+ + e^- \rightarrow COOH^*$, compared with fully O-terminated Mo_2CT_x (**Figures 10(d)**). In addition, the author also investigated the selectivity of catalysts toward to CO_2RR (**Figure 10(e)**), it was found that O-terminated Mo_2CT_x possessed the least negative $U_L(CO_2)$-$U_L(H_2)$ values of -0.1 V, implying that low amounts of F-T_x presence should be beneficial to CO_2RR to formic acid.

In addition, the performance of electrocatalytic CO_2RR on Mo_2C and Ti_3C_2 MXenes were also studied using a combination of experimental measurements and DFT+U calculations (**Table 6(b)**).[50] The experimental results shown that the electrocatalytic CO_2RR on Mo_2C and Ti_3C_2 possessed high faradaic efficiencies of 90% (250 mV overpotential) and 65% (650 mV overpotential). DFT-based free energy computations were used to understand the origin of the enhanced CO_2RR activity on Mo_2C and Ti_3C_2 MXenes. The DFT calculated results illustrated that the intermediates of CO_2RR strongly chemisorped on bare Mo_2C and Ti_3C_2 (**Table 6(b)**), and thus reduction of strongly adsorbed intermediates were predicted to be difficult. The X-ray photoelectron spectroscopy (XPS) measurements showed that the two MXenes were largely oxygen terminated. Therefore, additional DFT calculations were performed to examine the CO_2RR thermodynamics. Oxygen terminated MXene surfaces, the binding of key reaction intermediates such as CO_2 and CO was very weak indicating a less facile CO_2RR (the BE of CO and CO_2 on Mo_2C surface is about 0.02 eV, on oxygenated Ti_3C_2 surface, the BE of CO and CO_2 is about -0.05 eV). However, on oxygen terminated MXene surface with surface oxygen vacancies, the DFT and DFT+U calculated results showed that the activation of CO_2^* to $COOH^*$ need a free energy input of 1.04 eV and 0.78 eV on Ti_3C_2 and Mo_2C (**Table 6(b)**), respectively. The formed $COOH^*$ will spontaneously dissociate and form H_2O and CO^* on the two MXenes. These results suggested

that the Mo_2C is a promising catalyst for electrocatalytic CO_2RR to CO.

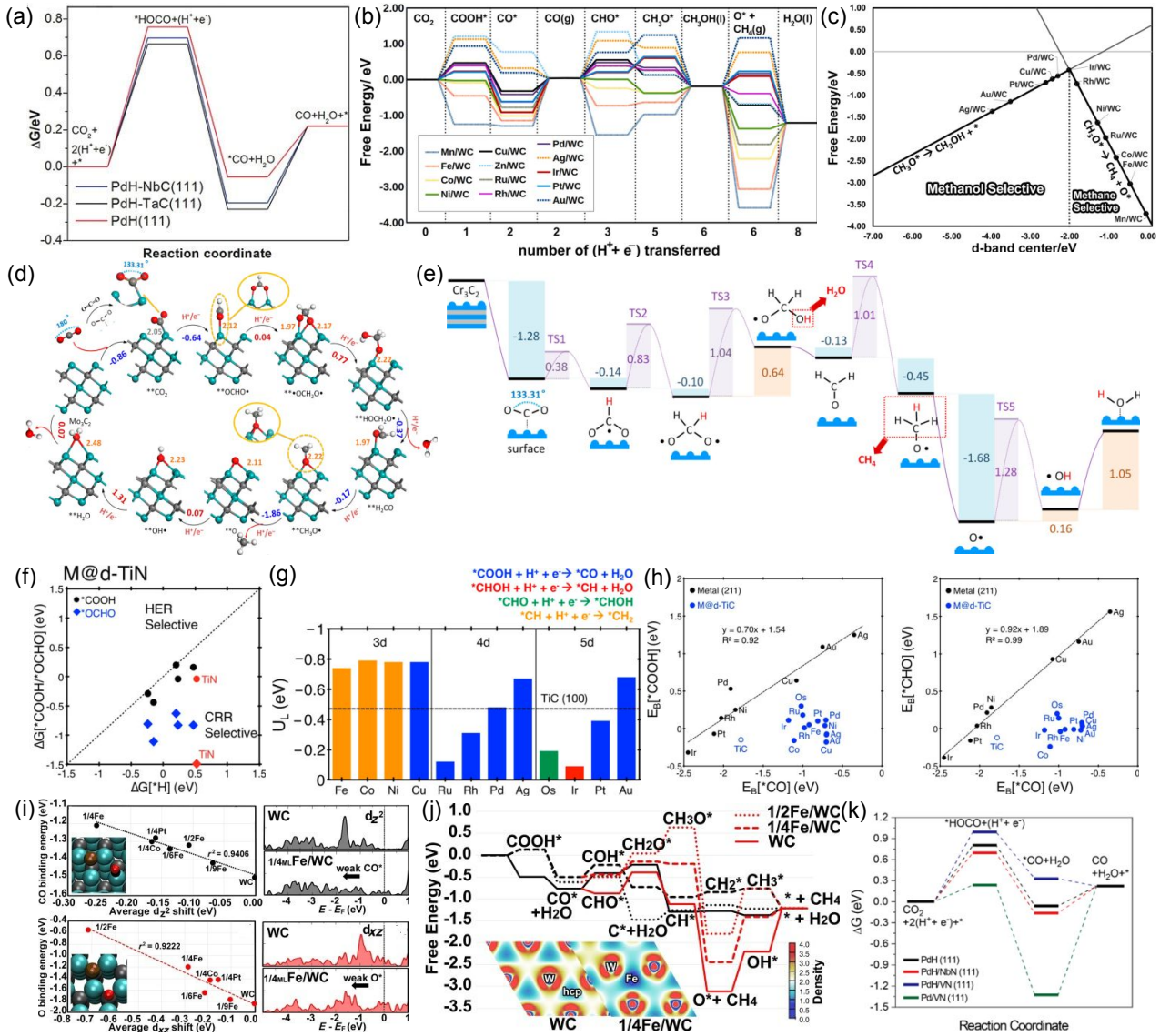

Figure 9. (a) Free energy diagrams for electrochemical CO_2RR calculated at U = 0 V on Pd/TMC materials. Reproduced with permission from ref. 42 from Wiley-VcH, Copyright 2018; (b) Free energy diagrams for electrochemical CO_2RR to different products on different metal MLs on the WC surface (U = 0 V) and (c) Volcano plot predicting the free energy change for the selectivity determining steps based on the total d-band center on different metal MLs on the WC surface. Reproduced with permission from ref. 43 from American Chemical Society, Copyright 2017; The minimum energy path of electrochemical CO_2RR to CH_4 and H_2O on (d) Mo_3C_2 and (e) Cr_3C_2 catalyst. ** refers to chemisorbed species. Reproduced with permission from ref. 45 from American Chemical Society, Copyright 2017; (f) The calculated free energy changes (ΔG) of the first protonation step of CO_2 reduction reaction ($CO_2 + H^+ + e^- \rightarrow COOH^*/OCHO^*$) and HER ($H^+ + e^- \rightarrow H^*$) at 0 V vs RHE on TiN and M@d-TiN catalysts, (g) The calculated limiting potential (U_L) of electrochemical CO_2RR on M@d-TiC(100), the different potential-determining steps (PDS) are marked with different colors and (h) The calculated binding energy of $COOH^*$ and CHO^* plotted as a function of CO^* binding energy on pure M (black) and M@d-TiC (blue) surfaces. Reproduced with permission from ref. 46 from American Chemical Society, Copyright 2017; (i) The correlation between the CO binding energy and the d_{z^2} PDOS of surface W atoms, the OBE and the $d_{xz/yz}$ PDOS, the W d_{z^2} and $d_{xz/yz}$ PDOS for pristine WC and Fe-coated WC and (j) The calculated free-energy diagram (U = 0 V) for the competitive carbophilic (black) and oxophilic (red) reaction pathways on WC, 1/4 ML Fe/WC and 1/2 ML Fe/WC surfaces. Inset: Charge densities in the plane of the W surface atoms. Reproduced with permission from ref. 44 from Wiley-VcH, Copyright 2015; (k) Free energy

diagrams for electrochemical CO_2RR calculated at U = 0 V on Pd/TMN materials. Reproduced with permission from ref. 16 from Wiley-VcH, Copyright 2020.

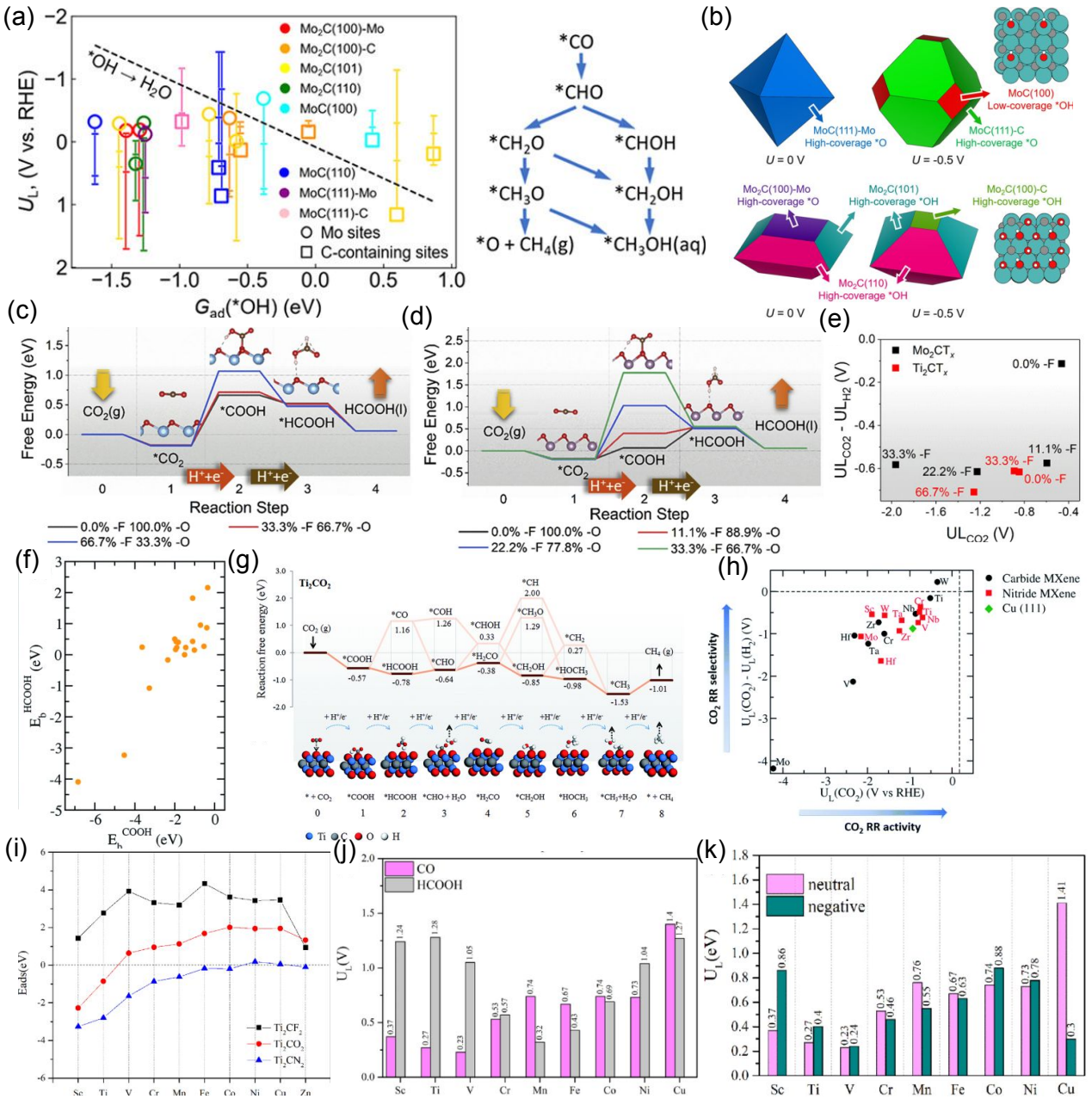

Figure 10. (a) The calculated U_L (for the desorption step of $OH^* \rightarrow H_2O(l)$) below which individual CO^*protonation steps become exergonic on different Mo_xC (x = 1, 2) active sites. For each active site, the vertical line spans the U_L for the four PCET steps along the optimum reaction path to produce CH_4 or CH_3OH in the minima reaction network displayed on the right, and (b) Ab initio thermodynamics Wulff construction showing the equilibrium particles shapes of MoC (top) and Mo_2C (bottom) at open-circuit potential (0 V vs RHE) and the CO_2RR working potential was taken the representative value of -0.5 V. Reproduced with permission from ref. 52 from American Chemical Society, Copyright 2020; The DFT calculated free energy of electrochemical CO_2RR to formic acid on (c) Ti_2CT_x and (d) Mo_2CT_x MXenes, and (e) the DFT Calculated $U_L(CO_2)$-$U_L(H_2)$ plot with respect to $U_L(CO_2)$ on all variants of Ti_2CT_x and Mo_2CT_x theoretical models with different F-T_x termination fractions. Reproduced with permission from ref. 47 from Elsevier, Copyright 2020; (f) The calculated BE of $HCOOH^*$ plotted as a function of $COOH^*$, (g) the calculated free energy diagram for the reduction of CO_2 to CH_4 on O-terminated Ti_2CO_2 MXene via different reaction path, and (h) The calculated $U_L(CO_2)$-$U_L(H_2)$ as a function of $U_L(CO_2)$

illustrating the selectivity of CO_2RR relative to HER for MXenes. Reproduced with permission from ref. 48 from the Royal Society of Chemistry, Copyright 2018; (i) The calculated BE of TM atoms anchored on the surface of Ti_2CT_2(T = F, O, N), (j) the calculated overpotentials for the productions of CO and HCOOH on TM-Ti_2CN_2, and (k) The calculated overpotential for the production of CO on neutral and negatively charged TM-Ti_2CN_2 surface. Reproduced with permission from ref. 51 from Elsevier, Copyright 2021.

Several O-terminated MXene catalysts in the form of M_2XO_2(M = Sc, Ti, Zr, Hf, V, Nb, Ta, Cr, Mo, W; and X = C, N) were investigated for CO_2RR to CH_4.[48] On most of O-terminated M_2XO_2 (except on V_2CO_2, Ta_2CO_2, and Cr_2CO_2), DFT results showed that the electrocatalytic CO_2RR to CH_4 occurred via a more favorable HCOOH* pathway, i.e., CO_2 (g) → COOH* → HCOOH* → CHO* → H_2CO^* → CH_2OH^* → $HOCH_3^*$ → CH3* → CH_4 (g). This pathway of CO_2RR to CH_4 was different from transition metals, where linear scaling relations prevented similarly-bound reaction intermediates (CO*, CHO*) from being stabilized independently on the surface. This study suggested that the limiting potential of MXene catalysts was determined by the binding energies of COOH* and/or HCOOH*, which could be tuned independently on Mxenes (**Figure 10(f)**). W_2CO_2 and Ti_2CO_2 were identified as two promising MXenes for CO_2RR (**Figures 10(f) and (g)**) with relatively low U_L of -0.35 V and -0.52 V vs. RHE, respectively. Meanwhile, the calculated theoretical overpotentials for CO_2RR to CH_4 on W_2CO_2 and Ti_2CO_2 were 0.52 and 0.69 V, respectively, significantly lower than those of Cu catalysts (0.91 to 1.10 V). Furthermore, the two MXenes have $U_L(CO_2)$-$U_L(H_2)$ values of 0.22 and -0.16 V (**Figure 10(h)**), respectively, implying that W_2CO_2 and Ti_2CO_2 should possess a high selectivity for CO_2RR as compared to HER.

TMN/TMC, TMN/TMC-supported metal, and single atom catalysts (SACs) have gained increased interest as CO_2RR catalysts.[46] Recent DFT calculations by Back et al. showed that CO_2 could be effectively reduced to CH_4 on the TiC(100) surface, where the PDS was predicted to be the protonation of CO* to CHO* (U_L = -0.47 V). However, the strong binding of the OCHO* and OH* intermediates on the TiN(100) surface resulted in surface poisoning. Free energy changes were calculated on single atom catalysts, where single transition metal atoms were embedded into the surface defect sites of TiC/TiN, denoted as M@d-TiC/TiN (M = Ag, Au, Co, Cu, Fe, Ir, Ni, Os, Pd, Pt, Rh, and Ru). The DFT calculations showed that the adsorption of reaction intermediates occured at the metal sites embedded on the TiC/TiN support. All M@d-TiN showed a similar behavior as the stoichiometric pristine TiN for OCHO* adsorption (**Figure 9(f)**), with ΔG(OCHO* → HCOOH*) values higher than 1 eV, suggesting an unfavorable CO_2RR on M@d-TiN catalysts. Different from M@d-TiN, Ir-doped TiC (Ir@d-TiC) was predicted to show a remarkably low overpotential of -0.09 V (the potential-determining step of $CHOH^* + H^+ + e^- \rightarrow CH^* + H_2O$) for the production of CH_4 (**Figure 9(g)**). The substantial activity improvement was attributed to the breaking of binding energy scaling relations on M@d-TiC (**Figure 9(h)**).

The possibility of supporting SACs on MXene for CO_2RR has been explored by Li et al. using DFT calculations. A range of TM single atoms (TM = Sc, Ti, V, Cr, Mn, Fe, Co, Ni, Cu, Zn) were anchored on two-dimensional Ti_2CN_2 MXenes for which the calculated phonon dispersion showed no imaginary bands, implying that Ti_2CN_2 should be stable and may be experimentally synthesized.[51] The stability of single TM atoms anchored on Ti_2CT_2 was studied by calculating the TM adsorption energies (**Figure 10(i)**). As shown in **Figure 10(i)**, it was found that all of the studied single TM atoms thermodynamically favored to anchor on Ti_2CN_2. The DFT results **(Figure 10(j))** on Ti_2CN_2 supported TM SACs showed that the main product of electrochemical CO_2RR was CO on Sc, Ti and V anchored on Ti_2CN_2 MXenes with the corresponding U_L values of 0.37 V, 0.27 V, and 0.23 V, respectively. Meanwhile, it was also found that Mn and Fe anchored on Ti_2CN_2 MXenes should possess a high catalytic activity to convert CO_2 into HCOOH under electrochemical conditions, with U_L of 0.32 V, and 0.43 V, respectively. Furthermore, it was revealed that the negative charging can regulate the product and efficiency of CO_2RR on TM-Ti_2CN_2 (**Figure 10(k)**).

The electrochemical CO_2RR to produce synthesis gas (syngas) with tunable CO/H_2 ratios has been studied by supporting Pd catalysts on transition metal nitride (TMN) substrates.[16] Because the supported Pd is transformed to PdH during the electrochemical reaction, Liu et al. calculated the binding energies (BE, **Table 6(a)**) and ΔG of HOCO* and CO* (**Figure 9(k)**) over PdH(111), PdH/NbN(111), and PdH/VN(111), representing the experimental Pd/C, Pd/NbN, and Pd/VN catalysts, respectively. The Pd/VN model was also included in the DFT calculation to reflect the coexistence of the Pd and PdH phases in Pd/VN during the CO_2RR. The DFT calculations predicted that Pd/VN(111) binds HOCO* and CO* more strongly compared to other surfaces. On Pd/VN(111), CO* desorption was predicted to be the rate-determining step because of the stronger binding affinity of Pd/VN(111) for CO. Consistent with the experimental observation, the DFT calculated free energy change predicted that the CO_2RR activity should follow the order of PdH/NbN(111) > PdH(111) > PdH/VN(111). Overall, the DFT results demonstrated that TMNs can effectively modify the CO_2RR activity of the PdH overlayers by adjusting the BE of intermediates. In particular, NbN was predicted to play a positive role in enhancing the CO_2RR performance of the PdH layers. This work suggested that NbN is a promising substrate to modify and reduce Pd loading and promote the selective conversion of CO_2 to syngas.

3.6 Other Reactions

TMN- and TMC-based materials have also been explored for other energy related electrochemical reactions, such as methanol[53-55] and ethanol[56,57] oxidation. These reactions are relevant to direct alcohol fuel cells (DAFCs), where the alcohol oxidation of occurs at the anode of DAFCs.

In direct methanol fuel cells (DMFCs), the ideal anodic reaction is the complete oxidation of methanol to CO_2, with the release of 6 electrons per methanol molecule ($CH_3OH + H_2O \rightarrow CO_2 + 6H^+ + 6e^-$).[54,55] Previous studies have suggested that [54,55] CH_3OH oxidation mainly occurs via two pathways: the indirect pathway and direct pathway (**Figure 11(a)**). The oxidation of CH_3OH to CO_2 proceeds via the CO* intermediate in the indirect

pathway. In contrast, CH_3OH oxidation to CO_2 occurs without the formation of the CO^* intermediate along the direct pathway (**Figure 11(a)**).[56,57] Each of these pathways can be further divided into CH and OH pathways (**Figure 11(a)**), where the C-H or O-H bond of methanol is broken first, respectively.

Currently, PGM-based catalysts are the best performing catalysts for methanol (MOR) and ethanol (EOR) oxidation reactions.[54-57] However, the high cost of PGM catalysts limits

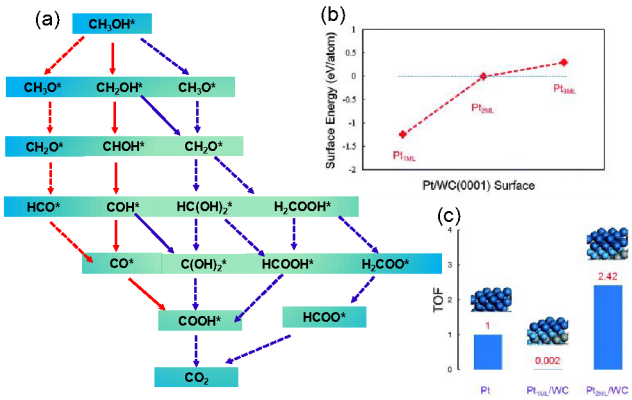

Figure 11. (a) Proposed pathway for the electrochemical methanol oxidation reaction (MOR) on TMC materials;[54,55] The solid and dashed red arrows represent that in the first step, the C-H and O-H bonds of methanol are broken along the indirect pathway, respectively. Similarly, the solid and dashed blue arrows represent that in the first step the C-H and O-H bonds of methanol are broken along the direct pathway, respectively; (b) The calculated surface energies of the mono-, bi- (fcc or hcp) layer and the tri-layer Pt atoms supported on WC(0001), where if $E_{Pt,sur} < 0$, Pt atoms will disperse on WC(0001) surface, and if $E_{Pt,sur} > 0$, Pt atoms will accumulate to form clusters of particles on WC(0001) surface and (c) The calculated normalized turnover frequency (TOF) for the electrooxidation of methanol on of a series of Pt-modified WC(0001) surfaces. Reproduced with permission from ref. 55 from the Royal Society of Chemistry, Copyright 2015.

the large-scale application of DAFCs.[53-57] Furthermore, the stronger binding of carbonyl-containing intermediates and/or CO on Pt/Pd surfaces at low potentials results in the surface poisoning of PGM catalysts, significantly reducing the cell lifetime.[56] Although operating DAFCs at higher potentials can prevent catalyst poisoning, the associated decrease in device efficiency can be prohibitive. TMCs and PGMs supported on TMCs are low-cost, poison-tolerant alternative catalysts for MOR[53-55] and EOR.[56,57] A brief summary of recent DFT studies of the methanol and ethanol electrooxidation reactions on TMC-based electrocatalysts follows.

DFT calculations have been extensively used to investigate the MOR mechanism over TMC surfaces.[53-55,173-175] In one study, the MOR pathways on basal (0001) and prismatic $(10\bar{1}0)$ surfaces of α-tungsten carbide (WC), and platinum (111) were investigated by calculating the free energy (**Table 7(a)**) of reaction intermediates and products (**Figure 11(a)**).[54] On Pt(111), the electrochemical MOR to CO_2 via the indirect pathway resulted in an accumulation of CO on the surface. This was found to be the case because, with an onset potential of 1.21 V, CO oxidation was the determining step and the free energy of CO formation was downhill (**Table 7(a)**). For the electrochemical MOR to CO_2 along the direct pathway (**Figure 11(a)**) on the Pt(111) surface, it was found that both the CH and OH pathways have the same potential-limiting step (the dehydrogenation of hydroxy-methylene to formaldehyde), i.e., $H_2COH \rightarrow H_2CO$ with an onset potential of 0.48 V. It was also found that the electrochemical MOR on the basal WC(0001) surface was more facile than on the prismatic $(10\bar{1}0)$ surface. On the basal WC (0001) surface, the most favorable pathway was found to be the OH direct pathway (**Figure 11(a)**): $CH_3OH^* \rightarrow CH_3O^* \rightarrow CH_2O^* \rightarrow H_2COOH^* \rightarrow H_2COO^* \rightarrow HCOO^* \rightarrow CO_2^* \rightarrow CO_2(g)$, and the corresponding potential-limiting step was $H_2CO + H_2O \rightarrow H_2COOH$ with a calculated onset potential of 0.64 V. In addition, the effect of an excess electron charge at the WC surface on the electrocatalytic activity toward the electrochemical MOR was analyzed. It was predicted that when WC surfaces are electron-rich, the most favored electrochemical MOR pathway becomes the OH indirect pathway. This was the case for the basal WC(0001) surface, where the calculated onset potential was 0.49 V, very close to the value on the Pt(111) surface (0.48 V). On these electron-rich surfaces, all the intermediate species (except CO and CO_2) along the reaction pathway were destabilized, resulting in more efficient CO production and its subsequent oxidation to CO_2. This study suggested that electron-rich WC could be an alternative to Pt for the catalysis of MOR.

DFT calculations have also been used to study the electrochemical MOR on a series of Pt-modified tungsten and surfaces (WC(0001)).[55] Surface energy calculations (**Figure 11 (b)**) of the mono- , bi- (fcc or hcp), tri-layer Pt carbide supported on WC(0001) revealed that the Pt mono- or bi- (fcc or hcp) layer on WC(0001) was considerably more stable than the Pt tri-layer on WC(0001) due to favorable Pt-cluster formation. Subsequently, the reaction barriers (E_a) and reaction energies (ΔE) of the elementary steps in methanol dehydrogenation to surface CO^*, and its further oxidation to CO_2^*, were calculated on Pt_{1ML}/WC(0001), $Pt_{2ML,fcc}$/WC(0001), $Pt_{2ML,hcp}$/WC(0001), and Pt(111) via the indirect pathway (**Table 7(b)**). It was found that the optimal methanol dehydrogenation pathway was different on different surfaces. Specifically, on Pt_{1ML}/WC(0001), the most favorable pathway was $CH_3OH^* \rightarrow CH_3O^* \rightarrow CH_2O^* \rightarrow CHO^* \rightarrow CO^*$, and on Pt_{2ML}/WC(0001) and Pt(111) surfaces, the most favorable pathway was $CH_3OH^* \rightarrow CH_2OH^* \rightarrow CHOH^* \rightarrow CHO^* \rightarrow CO^*$. CO^* oxidation was also studied in the presence of surface oxidants produced from water dissociation. Due to facile CO^* oxidation, the RDS of the MOR was predicted to be the C-H bond activation. In addition, the effect of water on the initial dehydrogenation of methanol was investigated. It was found that water played an important role in determining the absolute adsorption and kinetic values for the MOR, but did not have a significant influence on the inherent activity of the catalysts studied. The onset potentials for surface OH^* formation through water dissociation were calculated for the Pt-modified WC surfaces, and it was found that bi- (fcc or hcp) layer Pt-modified WC catalysts (0.67 V vs SHE and 0.66 V vs SHE) have similar

onset potentials compared to pure Pt(111) (0.64 V), but exhibit up to 2.4 times greater activity compared to that of pure Pt (**Figure 11(c)**).

Similarly, the electrochemical MOR on tungsten carbide (WC) and Pd-modified WC was investigated using a combination of DFT calculations and ultrahigh vacuum (UHV) studies.[53] The calculated results (**Table 7(a)**) showed that there is a strong affinity between the methoxy intermediate and the unmodified

Table 7. DFT calculated energetics of alcohol oxidation reactions. (a) Relative free energies (ΔG, eV) for methanol electrooxidation intermediates on Pt (111), WC(0001), and WC($10\bar{1}0$) surfaces under standard conditions (298 K, 1 atm). Binding energies (BE, eV) of methanol and methoxy on WC(0001), Pd/WC, and Pd(111) are also included; (b) Reaction barriers (E_a, eV) and reaction energies (ΔE, eV) of the elementary steps in methanol dehydrogenation to surface CO^* and further CO^* oxidation to CO_2(g) on Pt_{1ML}/WC(0001), $Pt_{2ML,fcc}$/WC(0001), $Pt_{2ML,hcp}$/WC(0001) and Pt(111) surfaces; (c) Binding energies (BE, eV) of potential ethanol oxidation reaction intermediates on Pt(111), Pt/TaC(111), Pd(111), and Pd/WC(0001) surfaces. Some of activation energies (E_a, eV) and reaction energies (ΔE) for the elementary steps of ethanol are also included.

(a)	Species	Pt(111)[54], Pd(111)[53]	WC(0001)[54]	WC($10\bar{1}0$)[54]	Pd/WC(0001)[53]
Methanol	CH_3OH(g)	ΔG=0.00	ΔG=0.00	ΔG=0.00	-
	CH_3OH^*	ΔG=0.18, BE=-0.24[53]	ΔG=-0.21, BE=0.69[53]	ΔG=-0.51	BE=-0.37
	CH_2OH^*	ΔG=0.19	ΔG=-0.47	ΔG=-0.64	-
	CH_3O^*	ΔG=0.18, BE=-1.65[53]	ΔG=-1.48, BE=3.95[53]	ΔG=-1.47	BE=-2.40
	$CHOH^*$	ΔG=0.16	ΔG=-0.62	ΔG=-2.83	-
	CH_2O^*	ΔG=0.67	ΔG=-1.05	ΔG=-1.69	-
	COH^*	ΔG=-0.17	ΔG=-0.73	-	-
	HCO^*	ΔG=0.11	ΔG=1.09	ΔG=-1.76	-
	$HC(OH)_2^*$	ΔG=1.03	-	-	-
	H_2COOH^*	ΔG=1.82	ΔG=-0.41	ΔG=-0.96	-
	CO^*	ΔG=-0.66	ΔG=-0.80	ΔG=-1.12	-
	$C(OH)_2^*$	ΔG=0.38	ΔG=2.42	ΔG=2.51	-
	$HCOOH^*$	ΔG=0.73	ΔG=0.26	ΔG=-0.99	-
	H_2COO^*	-	ΔG=-0.72	ΔG=-2.17	-
	CO^*+OH^*	-	ΔG=-1.33	ΔG=-2.24	-
	$COOH^*$	ΔG=0.55	ΔG=-0.28	ΔG=1.28	-
	$HCOO^*$	-	ΔG=-0.76	ΔG=-2.34	-
	CO_2^*	-	ΔG=-0.55	ΔG=-1.06	-
	CO_2(g)	ΔG=0.12	ΔG=0.12	ΔG=0.12	-
(b)		Pt(111)[55]	Pt_{1Ml}/WC[55]	$Pt_{2Ml,fcc}$/WC[55]	$Pt_{2Ml,hcp}$/WC[55]
Methanol	$CH_3OH^*\rightarrow CH_2OH^*+H^*$	E_a=0.72, ΔE=-0.21	E_a=1.01, ΔE=0.29	E_a=0.68, ΔE=-0.44	E_a=0.77, ΔE=-0.18
	$CH_3OH^*\rightarrow CH_3O^*+H^*$	E_a=0.90, ΔE=0.63	E_a=0.92, ΔE=0.22	E_a=1.01, ΔE=0.08	E_a=1.03, ΔE=0.42
	$CH_2OH^*\rightarrow CHOH^*+H^*$	E_a=0.65, ΔE=-0.17	E_a=0.57, ΔE=0.43	E_a=0.67, ΔE=-0.57	E_a=0.74, ΔE=-0.20
	$CH_2OH^*\rightarrow CH_2O^*+H^*$	E_a=0.91, ΔE=0.51	E_a=0.82, ΔE=0.07	E_a=0.98, ΔE=0.29	E_a=1.17, ΔE=0.53
	$CH_3O^*\rightarrow CH_2O^*+H^*$	E_a=0.43, ΔE=-0.33	E_a=0.36, ΔE=0.13	E_a=0.85, ΔE=-0.23	E_a=0.94, ΔE=-0.07
	$CHOH^*\rightarrow COH^*+H^*$	E_a=0.64, ΔE=-0.51	E_a=0.58, ΔE=0.14	E_a=0.55, ΔE=-0.95	E_a=0.58, ΔE=-0.72
	$CHOH^*\rightarrow CHO^*+H^*$	E_a=0.56, ΔE=-0.11	E_a=0.20, ΔE=-0.61	E_a=0.46, ΔE=-0.23	E_a=0.47, ΔE=-0.09
	$CH_2O^*\rightarrow CHO^*+H^*$	E_a=0.47, ΔE=-0.79	E_a=0.45, ΔE=-0.26	E_a=0.41, ΔE=-1.10	E_a=0.45, ΔE=-0.82
	$CHO^*\rightarrow CO^*+H^*$	E_a=0.31, ΔE=-0.73	E_a=0.61, ΔE=-0.68	E_a=0.29, ΔE=-1.40	E_a=0.32, ΔE=-1.04
	$COH^*\rightarrow CO^*+H^*$	E_a=0.93, ΔE=-1.26	E_a=0.59, ΔE=-1.43	E_a=0.89, ΔE=-0.68	E_a=0.84, ΔE=-0.42
	$CO^*+OH^*\rightarrow COOH^*$	E_a=0.43, ΔE=-0.34	E_a=0.49, ΔE=0.04	E_a=0.58, ΔE=-0.24	E_a=0.59, ΔE=-0.24
(c)	Species	Pt(111)[56]	Pt/TaC(111)[56]	Pd(111)[57]	Pd/WC(0001)[57]
Ethanol	$CH_3CH_2OH^*$	BE=-0.31	BE=-0.42	BE=-0.30	BE=-0.58
	$CH_3CH_2O^*$	BE=-1.82	BE=-1.92	BE=-1.55	BE=-2.31
	CH_3CHOH^*	BE=-2.28	BE=-1.42	BE=-2.12	BE=-2.05
	$CH_2CH_2OH^*$	BE=-2.45	BE=-1.92	BE=-2.28	BE=-1.98
	CH_3^*	BE=-2.38	BE=-1.66	BE=-2.38	BE=-2.24
	CH_2OH^*	BE=-2.37	BE=-1.50	BE=-2.25	BE=-2.17
	CH_3CHO^*	BE=-0.71	BE=-0.48	BE=-0.29	BE=-0.16
	CH_3CO^*	BE=-2.37	BE=-1.90	BE=-2.14	BE=-1.86
	CH_2CO^*	BE=-1.48	BE=-0.51	BE=-1.14	BE=-0.97
	CO^*	BE=-2.02	BE=-1.35	BE=-1.98	BE=-1.36
	H^*	BE=-0.46	BE=-0.28	-	-

	$CH_3CH_2OH^*+^*\rightarrow CH_3CHOH^*+H^*$	E_a=0.78, ΔE=0.19	E_a=0.62, ΔE=0.13	-	-
	$CH_3CH_2OH^*+^*\rightarrow CH_3^*+CH_2OH^*$	E_a=2.64, ΔE=0.31	E_a=2.31, ΔE=1.31	-	-

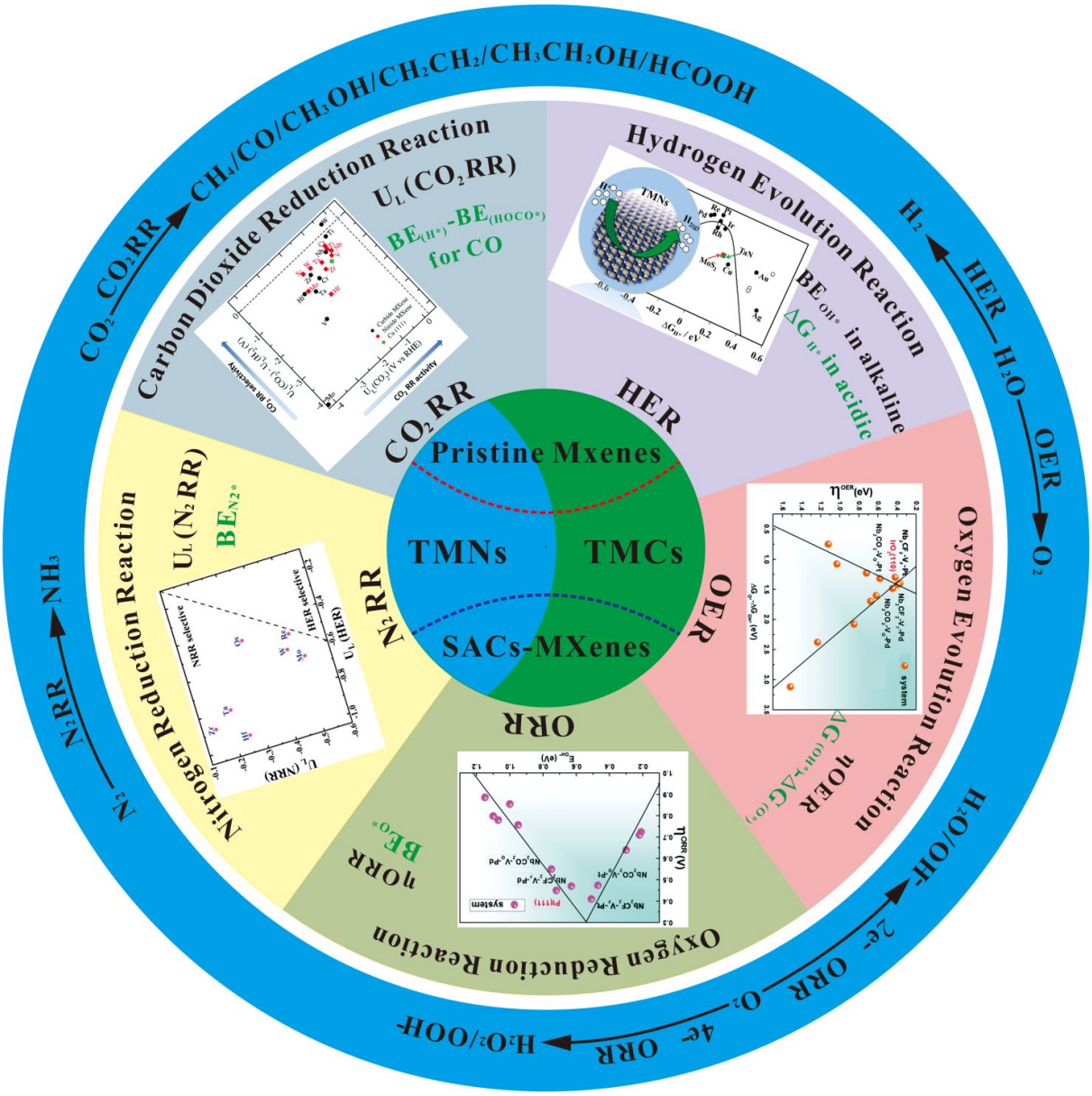

Figure 12. The summarized activity descriptors for all the electrolytic reactions determined through DFT calculations. The insert picture in HER, OER, ORR, N_2RR, and CO_2RR come from ref. 15, ref. 31, ref. 31, ref. 40, and ref. 48, respectively. The corresponding copyrights are reproduced with permissions from ref. 15 from American Chemical Society, Copyright 2017, ref. 31 from the Royal Society of Chemistry, Copyright 2020, ref. 31 from the Royal Society of Chemistry, Copyright 2020, ref. 40 from Wiley-Vch, Copyright 2019, and ref. 48 from the Royal Society of Chemistry, Copyright 2018, respectively.

WC surface through the oxygen atom. This strong interaction resulted in a significantly lengthened C-O bond compared to gas-phase values. For methoxy, the gas phase C-O bond length is 1.36 Å, compared to the calculated C-O bond length of 1.44 Å on Pd(111) and Pd/WC, and 1.48 Å on WC. The weakening of the C-O bond of the adsorbed methoxy facilitates the formation of a CH_3 fragment on the pure WC(0001) surface, which recombines with an atomic hydrogen to form CH_4, as verified in the temperature programmed desorption (TPD) measurements. When compared to the unmodified WC(0001) surface, the binding energy of methoxy on Pd_{ML}/WC(0001) was substantially reduced, which inhibited the formation of CH_4. On the other

hand, the stronger binding energy of methoxy (**Table 7(a)**) on Pd_{ML}/WC(0001) compared to Pd(111) was expected to result in higher MOR activity, as confirmed by the TPD results. Based on these results, Pd-modified WC may be a promising catalyst for the electrochemical MOR.

Several DFT studies have also been performed to investigate the EOR mechanism over TMC surfaces.[56,57,176,177] In one study, DFT calculations were used investigate the binding energies of ethanol and EOR intermediates on Pt_{ML}/TaC(111), including CH_3CH_2O (ethoxy), CH_3CHOH, CH_2CH_2OH, CH_3, CH_2OH, CH_3CHO, CH_3CO, CH_2CO, and CO (**Table 7(c)**).[56] The DFT calculated binding energies of ethanol on Pt_{ML}/TaC(111) and Pt(111) were 0.42 eV and -0.31 eV, respectively, which showed that there was a slightly stronger interaction with the Pt-modified carbide surface. Similarly, the binding energy of ethoxy was slightly higher on Pt_{ML}/TaC (-1.92 eV) than that on Pt(111) (-1.82 eV). Interestingly, it was found that binding energies of other intermediates (CH_3CHOH, CH_2CH_2OH, CH_3, CH_2OH, CH_3CHO, CH_3CO, CH_2CO, and CO) on the Pt(111) surface were larger than those on the Pt_{ML}/TaC(111) surface, implying that Pt_{ML}/TaC(111) should facilitate the formation and conversion of these OER reaction intermediates. In agreement with the in-situ IRRAS-LSV experimental results, the DFT calculations predicted that the effect of CO poisoning should be alleviated on the Pt_{ML}/TaC(111) compared to Pt(111), resulting in more facile CO oxidation on Pt_{ML}/TaC(111). Additional DFT calculations were performed to calculate the activation energies of the C-H and C-C bond scission steps to further understand the reaction pathways for ethanol decomposition on Pt(111) and Pt_{ML}/TaC(111) surfaces (**Table 7(c)**). It was found that the activation energies for C-H bond cleavage were lower than those for C-C bond cleavage on both surfaces, suggesting that the primary reaction pathways for both surfaces should follow the C-H bond scission pathway. Pt_{ML}/TaC(111) had lower activation energies for both C-H and C-C bond scissions compared to Pt(111), suggesting facile EOR on Pt_{ML}/TaC(111) compared to Pt(111). The combined experimental and theoretical results from this study indicate that Pt-modified TaC may be a stable and promising electrocatalyst for ultra-low Pt loading for the EOR in both acid and alkaline electrolytes.

Similarly, the electrochemical EOR on Pd-modified tungsten carbide (Pd_{ML}/WC(0001)) was also investigated using DFT and electrochemical methods in DEFCs.[57] The DFT calculated results showed that the adsorbed ethanol and ethoxy species preferred to bind to the atop site of the Pd(111) and Pd_{ML}/WC(0001) surfaces via the oxygen atom. In contrast, all the other intermediates (CH_3CHOH, CH_2CH_2OH, CH_3, CH_2OH, CH_3CHO, CH_3CO, CH_2CO, and CO) absorbed to the Pd(111) and Pd_{ML}/WC(0001) surfaces via the carbon atom. The CH_3CHO intermediate was found to bind through both carbon and oxygen atoms. The DFT calculated binding energies (**Table 7(c)**) showed that Pd_{ML}/WC(0001) binds EOR reaction intermediates more weakly compared to Pd(111). The weakened binding of these reaction intermediates on Pd_{ML}/WC(0001) indicates a facile EOR alleviated of CO poisoning. Furthermore, it was found that the ethanol activity toward the C-H and C-C bond cleavage on the Pd_{ML}/WC(0001) surface was enhanced, compared to Pd(111), while the undesired C-O bond scission mainly occurred on the unmodified WC surface. Thus, Pd_{ML}/WC(0001) could be a potential low-cost catalyst for the EOR at ambient conditions.

4. Conclusions, Challenges and Opportunities

As described above, DFT calculations have provided significant insight into the reaction mechanisms of a wide range of electrochemical reactions on TMC- and TMN-based catalysts. **Figure 12** summarizes the DFT-identified descriptors of electrochemical reactions on TMC and TMN based catalysts. ΔG_H^* is the descriptor of HER in an acidic medium.[11,16] In alkaline environments, in addition to ΔG_H^*, the kinetic barrier to water dissociation and OH binding energy are important descriptors to determine the overall kinetics of the HER.[14] For OER, $\Delta G_{(OH^*)}$-$\Delta G_{(O^*)}$ has been identified as a descriptor.[23] The binding energy of oxygen (BEO) has been shown to correlate well with the ORR activity and serves as an activity descriptor of ORR on TMC and TMN based materials.[3,27,76] For N_2RR, the limiting potential, i.e., the potential (U_L) required to make all electrochemical steps exothermic,[48] has been found to correlate with the nitrogen binding energy (NBE), suggesting that the NBE is a descriptor of N_2RR activity on TMN based materials.[48,74] The CO_2RR is a complex reaction with multiple C_1 and C_2 compounds as products. Thus a single descriptor of CO_2RR that can effectively describe the products is not practical. However, the binding energy of HOCO* and the difference of binding energies of H^* and $HOCO^*$ have been found to correlate well with the CO faradic efficiencies for the conversion of CO_2 to CO.[178] Below are several challenges and opportunities to further utilize DFT calculations for designing and improving TMC and TMN electrocatalysts:

1. For most electrocatalytic reactions, the descriptors for activity and selectivity are well established over metal electrocatalysts. With the exception of the HER over TMC-based electrocatalysts, there is a lack of understanding of whether these descriptors can be extended or modified to TMC- and TMN-based catalysts. Furthermore, compared to the TMC counterparts, DFT calculations of TMN materials either as catalysts and catalyst supports are much less explored at present.
2. TMC and TMN surfaces are often modified by the presence of vacancies and by the formation metal-oxygen bonds under electrocatalytic conditions. It is important to develop DFT structural models to describe active sites involving vacancies and oxygen modification. The development of such models should be closely coupled with experimental characterization under in-situ conditions.
3. TMC and TMN substrates are often used to support metal modifiers to enhance electrocatalytic properties. It is critical to develop DFT models to accurately describe the interfacial active sites at the metal/TMC and metal/TMN interfaces. Such interfacial models should also consider potential complications from vacancies and oxygen modifications described above.
4. At present most of the DFT calculations do not adequately consider the role of applied potentials and solvation effect from the electrolyte. Including these effects is particularly important for TMC- and TMN-based electrocatalysts because their surface compositions and the interfacial sites are often less stable than

the PGM counterparts at oxidizing potentials or in alkaline electrolyte.

5.Previous DFT efforts to study electrochemical reactions on TMC and TMN based catalysts primarily focused on the thermodynamic aspects and did not sufficiently describe the electrochemical reaction at relevant experimental reaction conditions. Therefore, future theoretical studies should aim to explore catalysis-kinetics of reactions on TMC and TMN based materials using kinetic models such as kinetic Monte Carlo or microkinetic simulations developed using the DFT calculated energetics.

6.Theoretical results have helped explain trends in experimentally observed electrocatalytic activity and selectivity for the electrocatalytic reactions summarized in this article. Future efforts in DFT calculations should continue to be coupled with experimental measurements, especially over well-characterized catalysts under in-situ reaction conditions, to further advance the understanding and development of TMC- and TMN-based materials as electrocatalysts.

Conflicts of interest

The authors declare no conflicts of interest.

Acknowledgements

This work was supported by the US Department of Energy, Office of Basic Energy Sciences, Catalysis Science Program (Grant No. DE-FG02-13ER16381). Dong Tian acknowledges the financial support from the China Scholarship Council (No.201808740001). S. K. acknowledges the faculty start-up fund from Florida A&M University.

Notes and references

1. J. G. Chen, *Chemical Reviews*, 1996, **96**, 1477-1498.
2. W. Wan, B. M. Tackett and J. G. Chen, *Chem Soc Rev*, 2017, **46**, 1807-1823.
3. Y. C. Kimmel, X. Xu, W. Yu, X. Yang and J. G. Chen, *ACS Catalysis*, 2014, **4**, 1558-1562.
4. J. Mao, S. Li, Y. Zhang, X. Chu and Z. Yang, *J Chem Phys*, 2016, **144**, 204703.
5. Y. Yu, J. Zhou and Z. Sun, *Advanced Functional Materials*, *2020, **30** (47), 2000570.*
6. I. Matanovic and F. H. Garzon, *Phys Chem Chem Phys*, 2018, **20**, 14679-14687.
7. R. B. Levy and M. Boudart, Science, 1973, 181 (4099), 547-549.
8. S. T. Gyama, CatalysisToday, 1992, **15**, 179-200.
9. C. Yang, R. Zhao, H. Xiang, J. Wu, W. Zhong, W. Li, Q. Zhang, N. Yang and X. Li, *Advanced Energy Materials*, 2020, **10**, 2002260.
10. R. M. Bullock, J. G. Chen, L. Gagliardi, P. J. Chirik, O. K. Farha, C. H. Hendon, C. W. Jones, J. A. Keith, J. Klosin, S. D. Minteer, R. H. Morris, A. T. Radosevich, T. B. Rauchfuss, N. A. Strotman, A. Vojvodic, T. R. Ward, J. Y. Yang and Y. Surendranath, *Science*, 2020, **369**, 786.
11. Q. Zhang, Z. Jiang, B. M. Tackett, S. R. Denny, B. Tian, X. Chen, B. Wang and J. G. Chen, *ACS Catalysis*, 2019, **9**, 2415-2422.
12. D. D. Vasić, I. A. Pašti and S. V. Mentus, *International Journal of Hydrogen Energy*, 2013, **38**, 5009-5018.
13. J. R. Kitchin, J. K. Nørskov, M. A. Barteau and J. G. Chen, *Catalysis Today*, 2005, **105**, 66-73.
14. R. Michalsky, Y.-J. Zhang and A. A. Peterson, *ACS Catalysis*, 2014, **4**, 1274-1278.
15. Y. Abghoui and E. Skúlason, *The Journal of Physical Chemistry C*, 2017, **121**, 24036-24045.
16. Y. Liu, D. Tian, A. N. Biswas, Z. Xie, S. Hwang, J. H. Lee, H. Meng and J. G. Chen, *Angew Chem Int Ed Engl*, 2020, **132**, 1141-1144.
17. Z. Chen, Y. Song, J. Cai, X. Zheng, D. Han, Y. Wu, Y. Zang, S. Niu, Y. Liu, J. Zhu, X. Liu and G. Wang, *Angew Chem Int Ed Engl*, 2018, **57**, 5076-5080.
18. W. Jiang, X. Zou, H. Du, L. Gan, C. Xu, F. Kang, W. Duan and J. Li, *Chemistry of Materials*, 2018, **30**, 2687-2693.
19. B. Ding, W.-J. Ong, J. Jiang, X. Chen and N. Li, *Applied Surface Science*, 2020, **500,** 143987.
20. D. Chen, Z. Chen, X. Zhang, Z. Lu, S. Xiao, B. Xiao and C. V. Singh, *Journal of Energy Chemistry*, 2021, **52**, 155-162.
21. J. Wan, C. Wang, Q. Tang, X. Gu and M. He, *RSC Advances*, 2019, **9**, 37467-37473.
22. S. Xu, M. Wang, G. Saranya, N. Chen, L. Zhang, Y. He, L. Wu, Y. Gong, Z. Yao, G. Wang, Z. Wang, S. Zhao, H. Tang, M. Chen and H. Gou, *Applied Catalysis B: Environmental*, 2020, **268**, 118385.
23. B. M. Tackett, W. Sheng, S. Kattel, S. Yao, B. Yan, K. A. Kuttiyiel, Q. Wu and J. G. Chen, *ACS Catalysis*, 2018, **8**, 2615-2621.
24. X. Bai, Q. Wang, G. Xu, Y. Ning, K. Huang, F. He, Z. J. Wu and J. Zhang, *Chemistry*, 2017, **23**, 16862-16870.
25. J. Chen, Q. Long, K. Xiao, T. Ouyang, N. Li, S. Ye and Z.-Q. Liu, *Science Bulletin*, 2021, DOI: 10.1016/j.scib.2021.02.033.
26. S. Wang, X. Chu, X. Zhang, Y. Zhang, J. Mao and Z. Yang, *The Journal of Physical Chemistry C*, 2017, **121**, 21333-21342.
27. M. Reda, H. A. Hansen and T. Vegge, *ACS Catalysis*, 2018, **8**, 10521-10529.
28. X. Zhang, Z. Lu and Z. Yang, *Journal of Power Sources*, 2016, **321**, 163-173.
29. A. Seifitokaldani, O. Savadogo and M. Perrier, *Electrochimica Acta*, 2014, **141**, 25-32.
30. H. Abroshan, P. Bothra, S. Back, A. Kulkarni, J. K. Nørskov and S. Siahrostami, *The Journal of Physical Chemistry C*, 2018, **122**, 4783-4791.
31. D. Kan, D. Wang, X. Zhang, R. Lian, J. Xu, G. Chen and Y. Wei, *Journal of Materials Chemistry A*, 2020, **8**, 3097-3108.
32. H. Cheng, L. X. Ding, G. F. Chen, L. Zhang, J. Xue and H. Wang, *Adv Mater*, 2018, **30**, e1803694.
33. I. Matanovic, F. H. Garzon and N. J. Henson, *Phys Chem Chem Phys*, 2014, **16**, 3014-3026.
34. Y. Abghoui, A. L. Garden, J. G. Howalt, T. Vegge and E. Skúlason, *ACS Catalysis*, 2015, **6**, 635-646.
35. Y. Abghoui and E. Skúlason, *The Journal of Physical Chemistry C*, 2017, **121**, 6141-6151.
36. X. Yang, S. Kattel, J. Nash, X. Chang, J. H. Lee, Y. Yan, J. G. Chen and B. Xu, *Angew Chem Int Ed Engl*, 2019, **58**, 13768-13772.
37. X. Yang, J. Nash, J. Anibal, M. Dunwell, S. Kattel, E. Stavitski, K. Attenkofer, J. G. Chen, Y. Yan and B. Xu, *J Am Chem Soc*, 2018, **140**, 13387-13391.
38. L. R. Johnson, S. Sridhar, L. Zhang, K. D. Fredrickson, A. S. Raman, J. Jang, C. Leach, A. Padmanabhan, C. C. Price, N. C. Frey, A. Raizada, V. Rajaraman, S. A. Saiprasad, X. Tang and A. Vojvodic, *ACS Catalysis*, 2019, **10**, 253-264.
39. S. Wang, B. Li, L. Li, Z. Tian, Q. Zhang, L. Chen and X. C. Zeng, *Nanoscale*, 2020, **12**, 538-547.

40. L. Li, X. Wang, H. Guo, G. Yao, H. Yu, Z. Tian, B. Li and L. Chen, *Small Methods*, 2019, **3**, 1900337.
41. B. Huang, N. Li, W.-J. Ong and N. Zhou, *Journal of Materials Chemistry A*, 2019, **7**, 27620-27631.
42. J. Wang, S. Kattel, C. J. Hawxhurst, J. H. Lee, B. M. Tackett, K. Chang, N. Rui, C. J. Liu and J. G. Chen, *Angew Chem Int Ed Engl*, 2019, **58**, 6271-6275.
43. S. Wannakao, N. Artrith, J. Limtrakul and A. M. Kolpak, *The Journal of Physical Chemistry C*, 2017, **121**, 20306-20314.
44. S. Wannakao, N. Artrith, J. Limtrakul and A. M. Kolpak, *ChemSusChem*, 2015, **8**, 2745-2751.
45. N. Li, X. Chen, W. J. Ong, D. R. MacFarlane, X. Zhao, A. K. Cheetham and C. Sun, *ACS Nano*, 2017, **11**, 10825-10833.
46. S. Back and Y. Jung, *ACS Energy Letters*, 2017, **2**, 969-975.
47. A. D. Handoko, H. Chen, Y. Lum, Q. Zhang, B. Anasori and Z. W. Seh, *iScience*, 2020, **23**, 101181.
48. A. D. Handoko, K. H. Khoo, T. L. Tan, H. Jin and Z. W. Seh, *Journal of Materials Chemistry A*, 2018, **6**, 21885-21890.
49. Y. Xiao and W. Zhang, *Nanoscale*, 2020, **12**, 7660-7673.
50. N. H. Attanayake, H. R. Banjade, A. C. Thenuwara, B. Anasori, Q. Yan and D. R. Strongin, *Chem Commun (Camb)*, 2021, **57**, 1675-1678.
51. F. Li, H. Ai, C. Shi, K. H. Lo and H. Pan, *International Journal of Hydrogen Energy*, 2021, **46**, 12886-12896.
52. H. Li and K. Reuter, *ACS Catalysis*, 2020, **10**, 11814-11821.
53. Z. J. Mellinger, T. G. Kelly and J. G. Chen, *ACS Catalysis*, 2012, **2**, 751-758.
54. C. Di Valentin, D. Fittipaldi and G. Pacchioni, *ChemCatChem*, 2015, **7**, 3533-3543.
55. T. Sheng, X. Lin, Z. Y. Chen, P. Hu, S. G. Sun, Y. Q. Chu, C. A. Ma and W. F. Lin, *Phys Chem Chem Phys*, 2015, **17**, 25235-25243.
56. Z. Jiang, Q. Zhang, Z. Liang and J. G. Chen, *Applied Catalysis B: Environmental*, 2018, **234**, 329-336.
57. Q. Zhang, Z. J. Mellinger, Z. Jiang, X. Chen, B. Wang, B. Tian, Z. Liang and J. G. Chen, *Journal of The Electrochemical Society*, 2018, **165**, J3031-J3038.
58. D. Tian, K. Li, Y. Wei, X. Zhu, C. Zeng, X. Cheng, Y. Zheng and H. Wang, *Phys Chem Chem Phys*, 2018, **20**, 11912-11929.
59. D. Tian, C. Zeng, H. Wang, X. Cheng, Y. Zheng, C. Xiang, Y. Wei, K. Li and X. Zhu, *Applied Surface Science*, 2017, **416**, 547-564.
60. Q. Zhang, B. M. Tackett, Q. Wu and J. G. Chen, *ChemElectroChem*, 2016, **3**, 1686-1693.
61. S. R. Denny, B. M. Tackett, D. Tian, K. Sasaki and J. G. Chen, *International Journal of Hydrogen Energy*, 2020, **45**, 22883-22892.
62. Z. Chen, J. Zhao, C. R. Cabrera and Z. Chen, *Small Methods*, 2018, **3**, 1800368.
63. Q. He, D. Tian, H. Jiang, D. Cao, S. Wei, D. Liu, P. Song, Y. Lin and L. Song, *Adv Mater*, 2020, **32**, e1906972.
64. Z. Xie, D. Tian, M. Xie, S.-Z. Yang, Y. Xu, N. Rui, J. H. Lee, S. D. Senanayake, K. Li, H. Wang, S. Kattel and J. G. Chen, *Chem*, 2020, **6**, 2703-2716.
65. Y. Ma, Z. He, Z. Wu, B. Zhang, Y. Zhang, S. Ding and C. Xiao, *Journal of Materials Chemistry A*, 2017, **5**, 24850-24858.
66. A. A. Gokhale, S. Kandoi, J. P. Greeley, M. Mavrikakis and J. A. Dumesic, *Chemical Engineering Science*, 2004, **59**, 4679-4691.
67. R. Koitz, J. K. Norskov and F. Studt, *Phys Chem Chem Phys*, 2015, **17**, 12722-12727.
68. E. Skulason, T. Bligaard, S. Gudmundsdottir, F. Studt, J. Rossmeisl, F. Abild-Pedersen, T. Vegge, H. Jonsson and J. K. Norskov, *Phys Chem Chem Phys*, 2012, **14**, 1235-1245.
69. J. K. Nørskov, T. Bligaard, A. Logadottir, J. R. Kitchin, J. G. Chen, S. Pandelov, and U. Stimming, Journal of The Electrochemical Society, 2005, 152(3), J23-J26.
70. J. K. Nørskov, J. Rossmeisl, A. Logadottir, and L. Lindqvist, J. Phys. Chem. B, 2004, 108, 17886-17892.
71. J. S. Li, Y. Wang, C. H. Liu, S. L. Li, Y. G. Wang, L. Z. Dong, Z. H. Dai, Y. F. Li and Y. Q. Lan, *Nat Commun*, 2016, **7**, 11204.
72. C. Lu, D. Tranca, J. Zhang, F. N. Rodri Guez Hernandez, Y. Su, X. Zhuang, F. Zhang, G. Seifert and X. Feng, *ACS Nano*, 2017, **11**, 3933-3942.
73. S. Kattel, P. Atanassov and B. Kiefer, *Phys Chem Chem Phys*, 2013, **15**, 148-153.
74. D. Ologunagba and S. Kattel, *Materials Advances*, 2021, **2**, 1263-1270.
75. T. Li, H. Deng, J. Liu, C. Jin, Y. Song and F. Wang, *Carbon*, 2019, **143**, 859-868.
76. H. Xu, D. Cheng, D. Cao and X. C. Zeng, *Nature Catalysis*, 2018, **1**, 339-348.
77. J. A. Gauthier, C. F. Dickens, L. D. Chen, A. D. Doyle and J. K. Nørskov, *The Journal of Physical Chemistry C*, 2017, **121**, 11455-11463.
78. M. Van den Bossche, E. Skúlason, C. Rose-Petruck and H. Jónsson, *The Journal of Physical Chemistry C*, 2019, **123**, 4116-4124.
79. K. Chang, H. Zhang, J. G. Chen, Q. Lu and M.-J. Cheng, *ACS Catalysis*, 2019, **9**, 8197-8207.
80. K. Chang, J. G. Chen, Q. Lu and M.-J. Cheng, *The Journal of Physical Chemistry C*, 2017, **121**, 24618-24625.
81. O. Andreussi, I. Dabo and N. Marzari, *J Chem Phys*, 2012, **136**, 064102.
82. R. Jinnouchi and A. B. Anderson, *Journal of Physical Chemistry C*, 2008, **112**, 8747-8750.
83. R. Jinnouchi and A. B. Anderson, *Physical Review B*, 2008, **77**, 245417.
84. S. Kattel and G. Wang, *J Phys Chem Lett*, 2014, **5**, 452-456.
85. R. Gao, D.-B. Cao, Y. Yang, Y.-W. Li, J. Wang and H. Jiao, *Applied Catalysis A: General*, 2014, **475**, 186-194.
86. C. P. Plaisance, S. D. Beinlich and K. Reuter, *The Journal of Physical Chemistry C*, 2018, **123**, 8287-8303.
87. J. K. Norskov, F. Abild-Pedersen, F. Studt and T. Bligaard, *Proc Natl Acad Sci U S A*, 2011, **108**, 937-943.
88. J. K. Nørskov, T. Bligaard, A. Logadottir, S. Bahn, L. B. Hansen, M. Bollinger, H. Bengaard, B. Hammer, Z. Sljivancanin, M. Mavrikakis, Y. Xu, S. Dahl and C. J. H. Jacobsen, *Journal of Catalysis*, 2002, **209**, 275-278.
89. G. Rostamikia and M. J. Janik, *Electrochimica Acta*, 2010, **55**, 1175-1183.
90. Z. W. Seh, J. Kibsgaard, C. F. Dickens, I. Chorkendorff, J. K. Norskov and T. F. Jaramillo, *Science*, 2017, **355**, 6321.
91. J. Greeley, I. E. Stephens, A. S. Bondarenko, T. P. Johansson, H. A. Hansen, T. F. Jaramillo, J. Rossmeisl, I. Chorkendorff and J. K. Norskov, *Nat Chem*, 2009, **1**, 552-556.
92. J. Greeley, T. F. Jaramillo, J. Bonde, I. B. Chorkendorff and J. K. Norskov, *Nat Mater*, 2006, **5**, 909-913.
93. D. Tian, C. Zeng, H. Wang, H. Luo, X. Cheng, C. Xiang, Y. Wei, K. Li and X. Zhu, *Journal of Alloys and Compounds*, 2016, **671**, 208-219.
94. D. Tian, C. Zeng, Y. Fu, H. Wang, H. Luo, C. Xiang, Y. Wei, K. Li and X. Zhu, *Solid State Communications*, 2016, **231-232**, 68-79.
95. Y. Xue, L. Gao, H. Liu, W. Ren, X. Shai, T. Wei, Y. Tian and C. Zeng, *Applied Surface Science*, 2021, **555**, 149654.
96. *Marcal Capdevila-Cortada, Zbigniew Łodziana, and Nuria Lo´pez´, ACS Catal, 2016, **6**, 8370-8379*.

97. L. Wang, T. Maxisch and G. Ceder, *Physical Review B*, 2006, **73**, 195107.
98. M. Cococcioni and S. de Gironcoli, *Physical Review B*, 2005, **71**, 035105.
99. A. E. Mattsson, R. Armiento, P. A. Schultz and T. R. Mattsson, *Physical Review B*, 2006, **73**, 195123.
100. B. M. Tackett, W. Sheng and J. G. Chen, *Joule*, 2017, **1**, 253-263.
101. Q. Gao, W. Zhang, Z. Shi, L. Yang and Y. Tang, *Adv Mater*, 2019, **31**, e1802880.
102. P. g. R. Jiao Deng, Dehui Deng, Liang Yu, Fan Yang and Xinhe Bao, *Energy Environ. Sci*, 2014, **7**, 1919.
103. S.-K. J. Sanjib Baran Roy, Kamran Akbar, Jae Ho Jeon, Linh Truong, Seung-Hyun Chun, Min Jong Noh, Juho Lee and Yong-Hoon Kim, *J. Mater. Chem. A*, **7**, 17046.
104. S. R. Chemler and M. T. Bovino, *ACS Catal*, 2013, **3**, 1076-1091.
105. D. V. Esposito and J. G. Chen, *Energy & Environmental Science*, 2011, **4**, 3900-3912.
106. D. V. Esposito, S. T. Hunt, A. L. Stottlemyer, K. D. Dobson, B. E. McCandless, R. W. Birkmire and J. G. Chen, *Angew Chem Int Ed Engl*, 2010, **49**, 9859-9862.
107. G. Gao, Y. Jiao, F. Ma, Y. Jiao, E. Waclawik and A. Du, *Journal of Catalysis*, 2015, **332**, 149-155.
108. N. Gaston and S. Hendy, *Catalysis Today*, 2009, **146**, 223-229.
109. N. Han, K. R. Yang, Z. Lu, Y. Li, W. Xu, T. Gao, Z. Cai, Y. Zhang, V. S. Batista, W. Liu and X. Sun, *Nat Commun*, 2018, **9**, 924.
110. M. P. Humbert, C. A. Menning and J. G. Chen, *Journal of Catalysis*, 2010, **271**, 132-139.
111. J. Jia, W. Zhou, Z. Wei, T. Xiong, G. Li, L. Zhao, X. Zhang, H. Liu, J. Zhou and S. Chen, *Nano Energy*, 2017, **41**, 749-757.
112. Y. C. Kimmel, L. Yang, T. G. Kelly, S. A. Rykov and J. G. Chen, *Journal of Catalysis*, 2014, **312**, 216-220.
113. F. Marinelli, A. Jelea and A. Allouche, *Surface Science*, 2007, **601**, 578-587.
114. Y. Peng, B. Lu, L. Chen, N. Wang, J. E. Lu, Y. Ping and S. Chen, *Journal of Materials Chemistry A*, 2017, **5**, 18261-18269.
115. B. M. Tackett, Y. C. Kimmel and J. G. Chen, *International Journal of Hydrogen Energy*, 2016, **41**, 5948-5954.
116. D. D. Vasić Anićijević, V. M. Nikolić, M. P. Marčeta-Kaninski and I. A. Pašti, *International Journal of Hydrogen Energy*, 2013, **38**, 16071-16079.
117. F. Wang, Y. Sun, Y. He, L. Liu, J. Xu, X. Zhao, G. Yin, L. Zhang, S. Li, Q. Mao, Y. Huang, T. Zhang and B. Liu, *Nano Energy*, 2017, **37**, 1-6.
118. J. Xie, S. Li, X. Zhang, J. Zhang, R. Wang, H. Zhang, B. Pan and Y. Xie, *Chem. Sci.*, 2014, **5**, 4615-4620.
119. D. V. Esposito, S. T. Hunt, Y. C. Kimmel and J. G. Chen, *J Am Chem Soc*, 2012, **134**, 3025-3033.
120. H. Shu, D. Zhou, F. Li, D. Cao and X. Chen, *ACS Appl Mater Interfaces*, 2017, **9**, 42688-42698.
121. Y. Zhang, X. Chen, Y. Huang, C. Zhang, F. Li and H. Shu, *The Journal of Physical Chemistry C*, 2017, **121**, 1530-1536.
122. S. Liu, Z. Li, C. Wang, W. Tao, M. Huang, M. Zuo, Y. Yang, K. Yang, L. Zhang, S. Chen, P. Xu and Q. Chen, *Nat Commun*, 2020, **11**, 938.
123. Y. Jiao, Y. Zheng, K. Davey and S.-Z. Qiao, *Nature Energy*, 2016, **1**, 16130.
124. Y. Wang, Y. Nian, A. N. Biswas, W. Li, Y. Han and J. G. Chen, *Advanced Energy Materials*, 2021, **11**, 2002967.
125. X. Li, P. Cui, W. Zhong, J. Li, X. Wang, Z. Wang and J. Jiang, *Chem Commun (Camb)*, 2016, **52**, 13233-13236.
126. Y. Wen, Z. Wei, J. Liu, R. Li, P. Wang, B. Zhou, X. Zhang, J. Li and Z. Li, *Journal of Energy Chemistry*, 2021, **52**, 412-420.
127. P. Chen, K. Xu, Z. Fang, Y. Tong, J. Wu, X. Lu, X. Peng, H. Ding, C. Wu and Y. Xie, *Angew Chem Int Ed Engl*, 2015, **54**, 14710-14714.
128. Y. Fan, S. Ida, A. Staykov, T. Akbay, H. Hagiwara, J. Matsuda, K. Kaneko and T. Ishihara, *Small*, 2017, **13**.
129. C. Hao, Y. Wu, Y. An, B. Cui, J. Lin, X. Li, D. Wang, M. Jiang, Z. Cheng and S. Hu, *Materials Today Energy*, 2019, **12**, 453-462.
130. M. Kim, S. Kim, D. Song, S. Oh, K. J. Chang and E. Cho, *Applied Catalysis B: Environmental*, 2018, **227**, 340-348.
131. D. Song, J. Shin, Y. Lee, Y. Kwon, J. Lim, E.-J. Kim, S. Oh, M. Kim and E. Cho, *ACS Applied Energy Materials*, 2019, **2**, 3452-3460.
132. K. Xu, P. Chen, X. Li, Y. Tong, H. Ding, X. Wu, W. Chu, Z. Peng, C. Wu and Y. Xie, *J Am Chem Soc*, 2015, **137**, 4119-4125.
133. Y. Zheng, Y. Jiao, Y. Zhu, Q. Cai, A. Vasileff, L. H. Li, Y. Han, Y. Chen and S. Z. Qiao, *J Am Chem Soc*, 2017, **139**, 3336-3339.
134. Z. Kou, L. Zhang, Y. Ma, X. Liu, W. Zang, J. Zhang, S. Huang, Y. Du, A. K. Cheetham and J. Wang, *Applied Catalysis B: Environmental*, 2019, **243**, 678-685.
135. S. Zhang, G. Gao, J. Hao, M. Wang, H. Zhu, S. Lu, F. Duan, W. Dong, M. Du and Y. Zhao, *ACS Appl Mater Interfaces*, 2019, **11**, 43261-43269.
136. Y. Yang, Y. Wang, M. Yao, X. Wang and H. Huang, *Phys Chem Chem Phys*, 2018, **20**, 30231-30238.
137. Q. Xu, H. Jiang, X. Duan, Z. Jiang, Y. Hu, S. W. Boettcher, W. Zhang, S. Guo and C. Li, *Nano Lett*, 2021, **21**, 492-499.
138. S. Lee, L. Bai and X. Hu, *Angew Chem Int Ed Engl*, 2020, **59**, 8072-8077.
139. J. Jiang, F. Sun, S. Zhou, W. Hu, H. Zhang, J. Dong, Z. Jiang, J. Zhao, J. Li, W. Yan and M. Wang, *Nat Commun*, 2018, **9**, 2885.
140. Y. Wang, Y. Zhou, M. Han, Y. Xi, H. You, X. Hao, Z. Li, J. Zhou, D. Song, D. Wang and F. Gao, *Small*, 2019, **15**, e1805435.
141. Z. Lu, G. Xu, C. He, T. Wang, L. Yang, Z. Yang and D. Ma, *Carbon*, 2015, **84**, 500-508.
142. K. Liu, S. Kattel, V. Mao and G. Wang, *The Journal of Physical Chemistry C*, 2016, **120**, 1586-1596.
143. L.-y. Feng, Y.-j. Liu and J.-x. Zhao, *Journal of Power Sources*, 2015, **287**, 431-438.
144. K. Uosaki, G. Elumalai, H. Noguchi, T. Masuda, A. Lyalin, A. Nakayama and T. Taketsugu, *J Am Chem Soc*, 2014, **136**, 6542-6545.
145. M. D. Bhatt, G. Lee and J. S. Lee, *Electrochimica Acta*, 2017, **228**, 619-627.
146. D. Zhao, Z. Zhuang, X. Cao, C. Zhang, Q. Peng, C. Chen and Y. Li, *Chem Soc Rev*, 2020, **49**, 2215-2264.
147. C. K. Poh, S. H. Lim, J. Lin and Y. P. Feng, *The Journal of Physical Chemistry C*, 2014, **118**, 13525-13538.
148. X. R. Wang, J. Y. Liu, Z. W. Liu, W. C. Wang, J. Luo, X. P. Han, X. W. Du, S. Z. Qiao and J. Yang, *Adv Mater*, 2018, **30**, e1800005.
149. Q. Gao, *Ionics*, 2019, DOI: 10.1007/s11581-019-03376-9.
150. I. J. Hsu, D. A. Hansgen, B. E. McCandless, B. G. Willis and J. G. Chen, *The Journal of Physical Chemistry C*, 2011, **115**, 3709-3715.
151. N. Y. Kim, J. H. Lee, J. A. Kwon, S. J. Yoo, J. H. Jang, H.-J. Kim, D.-H. Lim and J. Y. Kim, *Journal of Industrial and Engineering Chemistry*, 2017, **46**, 298-303.
152. M. Ma, S. You, W. Wang, G. Liu, D. Qi, X. Chen, J. Qu and N. Ren, *ACS Appl Mater Interfaces*, 2016, **8**, 32307-32316.
153. Y. Meng, X. Zhang, J. Mao, X. Xu and Z. Yang, *Applied Surface Science*, 2018, **439**, 845-851.
154. A. L. Stottlemyer, T. G. Kelly, Q. Meng and J. G. Chen, *Surface Science Reports*, 2012, **67**, 201-232.
155. T. Sun, Y. Jiang, Q. Wu, L. Du, Z. Zhang, L. Yang, X. Wang and Z. Hu, *Catalysis Science & Technology*, 2017, **7**, 51-55.
156. X. Xu, W. Ren, H. Xu, X. Zhang, X. Zheng, D. L. Phillips and C. Zhao, *Sensors and Actuators B: Chemical*, 2015, **213**, 139-149.

157. J. L. Yates, G. H. Spikes and G. Jones, *Phys Chem Chem Phys*, 2015, **17**, 4250-4258.
158. W. Guo, K. Zhang, Z. Liang, R. Zou and Q. Xu, *Chem Soc Rev*, 2019, **48**, 5658-5716.
159. J. Zhao and Z. Chen, *J Am Chem Soc*, 2017, **139**, 12480-12487.
160. X. F. Li, Q. K. Li, J. Cheng, L. Liu, Q. Yan, Y. Wu, X. H. Zhang, Z. Y. Wang, Q. Qiu and Y. Luo, *J Am Chem Soc*, 2016, **138**, 8706-8709.
161. Y. Abghoui and E. Skúlason, *Catalysis Today*, 2017, **286**, 78-84.
162. C. Ling, X. Niu, Q. Li, A. Du and J. Wang, *J Am Chem Soc*, 2018, **140**, 14161-14168.
163. Y. Abghoui and E. Skúlasson, *Procedia Computer Science*, 2015, **51**, 1897-1906.
164. X. Chen, X. Zhao, Z. Kong, W.-J. Ong and N. Li, *Journal of Materials Chemistry A*, 2018, **6**, 21941-21948.
165. C. Lv, Y. Qian, C. Yan, Y. Ding, Y. Liu, G. Chen and G. Yu, *Angew Chem Int Ed Engl*, 2018, **57**, 10246-10250.
166. G. L. Chai and Z. X. Guo, *Chem Sci*, 2016, **7**, 1268-1275.
167. S. Tang, X. Zhou, S. Zhang, X. Li, T. Yang, W. Hu, J. Jiang and Y. Luo, *ACS Appl Mater Interfaces*, 2019, **11**, 906-915.
168. C. Guo, T. Zhang, X. Deng, X. Liang, W. Guo, X. Lu and C. L. Wu, *ChemSusChem*, 2019, **12**, 5126-5132.
169. X. Li, W. Bi, M. Chen, Y. Sun, H. Ju, W. Yan, J. Zhu, X. Wu, W. Chu, C. Wu and Y. Xie, *J Am Chem Soc*, 2017, **139**, 14889-14892.
170. C. Zhang, S. Yang, J. Wu, M. Liu, S. Yazdi, M. Ren, J. Sha, J. Zhong, K. Nie, A. S. Jalilov, Z. Li, H. Li, B. I. Yakobson, Q. Wu, E. Ringe, H. Xu, P. M. Ajayan and J. M. Tour, *Advanced Energy Materials*, 2018, **8**, 1703487.
171. D. Opalka, C. Scheurer and K. Reuter, *ACS Catalysis*, 2019, **9**, 4944-4950.
172. T. Wang, J. Jelic, D. Rosenthal and K. Reuter, *ChemCatChem*, 2013, **5**, 3398-3403.
173. X. Yue, C. He, C. Zhong, Y. Chen, S. P. Jiang and P. K. Shen, *Adv Mater*, 2016, **28**, 2163-2169.
174. W. Zhang, Y. Fu, J. Wang and X. Wang, *Advanced Materials Interfaces*, 2017, **4**, 1601219.
175. G. Cui, P. K. Shen, H. Meng, J. Zhao and G. Wu, *Journal of Power Sources*, 2011, **196**, 6125-6130.
176. T. G. Kelly, A. L. Stottlemyer, X. Yang and J. G. Chen, *Journal of The Electrochemical Society*, 2014, **161**, E3165-E3170.
177. L. Luo, C. Fu, F. Yang, X. Li, F. Jiang, Y. Guo, F. Zhu, L. Yang, S. Shen and J. Zhang, *ACS Catalysis*, 2019, **10**, 1171-1184.
178. J. H. Lee, S. Kattel, Z. Jiang, Z. Xie, S. Yao, B. M. Tackett, W. Xu, N. S. Marinkovic and J. G. Chen, *Nat Commun*, 2019, **10**, 3724.